

---

This manuscript has been submitted for publication in the special issue ***Responding to Change: Propagation of Environmental Signals During Landscape Transience*** in ***Frontiers of Earth Science: Sedimentology, Stratigraphy and Diagenesis***. This pre-print has **not undergone peer-review** and subsequent versions of the manuscript may differ from this version. If accepted, the final version will be available via a DOI link on this page.

Please contact the corresponding author by email with any queries - [tim.cullen@uib.no](mailto:tim.cullen@uib.no)

Prepared for EarthArxiv on 27<sup>th</sup> May 2021

---

# Deep-water syn-rift stratigraphy as archives of Early-Mid Pleistocene palaeoenvironmental signals and controls on sediment delivery

Timothy M. Cullen<sup>\*1,2</sup>, Richard E. L. Collier<sup>1</sup>, David M. Hodgson<sup>1</sup>, Robert L. Gawthorpe<sup>2</sup>, Katerina Kouli<sup>3</sup>, Marco Maffione<sup>4</sup>, Haralambos Kranis<sup>3</sup>, Gauti T. Eliassen<sup>2</sup>.

1. School of Earth and Environment, University of Leeds, Leeds, United Kingdom
2. Department of Earth Sciences, University of Bergen, Bergen, Norway
3. Department of Geology and Geoenvironment, National and Kapodistrian University of Athens, Athens, Greece
4. Department of Earth and Environmental Sciences, University of Birmingham, Birmingham, United Kingdom

\* tim.cullen@uib.no

## Abstract

The timing and character of coarse siliciclastic sediment delivered to deep-water environments in active rift basins is governed by the complicated interactions of tectonics, climate, eustasy, hinterland geology, and shelf process regime. The stratigraphic archives of deep-water syn-rift basin-fills provide records of palaeoenvironmental changes (e.g. climate and vegetation) in onshore catchments, particularly where they are connected by narrow shelves. However, a chronostratigraphically constrained record of climatic fluctuations and process responses in the hinterland source area recorded in deep-water deposits is rare. Here, we integrate a fully cored research borehole with outcrop exposures of deep-water syn-rift stratigraphy to reconstruct palaeoenvironmental change within the stratigraphy of the West Xylokastro Fault Block in the Corinth Rift, Greece. We used palaeomagnetic and palynological analyses from borehole core samples to develop a chronostratigraphic and palaeoenvironmental model, which we compare to global records of Early-Mid Pleistocene climate and eustatic change. This framework allows establishment of a chronostratigraphic and palaeoenvironmental context to stratigraphic variability encountered in outcrop and in the borehole. Our results show that the ~240 m thick studied succession was deposited from ~1.1 to 0.6 Ma across the Early- to Mid-Pleistocene transition. During the Early Pleistocene, obliquity-paced climatic variability is largely coherent with vegetation changes of forest coverage within catchments on the southern margin of the Corinth Rift. Large magnitude, eccentricity-paced cyclicity can alter sediment supply from onshore catchments during the warming stages of severe interglacials where expansion of forest cover traps sediment within catchments. Conglomeratic grade sediment delivery to the deep-water is enhanced during glacial periods, interpreted to reflect sparse forest cover and large winter storms, and during semi-arid, grassland-dominated interglacial highstands during severe interglacials. More minor interglacials are easily outpaced by high sediment supply and are seldom represented stratigraphically. The study demonstrates the value of integrated palynological and sedimentological studies, whilst applying a conservative approach to interpretation when dealing with sparse palynological records from proximal deep-water stratigraphy. The observations open conceptual models where vegetation changes are

highlighted as an important control on sediment flux from onshore drainage basins to deep-water syn-rift successions.

## 1 **1 Introduction**

2 Deep-water, syn-rift depositional systems are highly dynamic. Short-scale temporal and spatial changes  
3 in accommodation produce complicated depocenters that can receive substantial but variable coarse-  
4 grained sediment supply on account of steep gradients, short transport distances and multiple input  
5 systems (Gawthorpe et al., 1994; Hadler-Jacobsen et al., 2005; Pechlivanidou et al., 2019). Despite  
6 this well-known complexity, smaller scale variability of deep-water syn-rift systems attributable to  
7 palaeoenvironmental change are seldom considered in depositional models, especially in comparison  
8 to responses to tectonic forcing, or eustatic variability in shallow water systems (e.g. Collier, 1990;  
9 Muravchik et al., 2017; Gawthorpe et al., 2017). Deep-water syn-rift systems are often directly linked to  
10 terrestrial drainage catchments as rift-basin physiography does not favour the development of wide  
11 shelves, and instead produces steep, short source-to-sink configurations (Gawthorpe et al., 1994;  
12 Sømme et al., 2009; Hadler-Jacobsen et al., 2005; Nelson et al., 2009; Covault & Graham, 2010;  
13 Armitage et al., 2013; Nyberg et al., 2018). As a result, sediment supply variability to the deep-water  
14 does not necessarily follow 'classical' lowstand or falling base-level models (Posamentier & Vail, 1988;  
15 Hadler-Jacobsen et al., 2005; Sømme et al., 2009; Nelson et al., 2009; Strachan et al., 2013; Watkins  
16 et al., 2018; Zhang et al., 2019a, b) and shelf process regime is less influential or can be considered  
17 fluvially-driven (Dixon et al., 2012; Cosgrove et al., 2018). Consequently, changes in sediment flux  
18 within onshore drainage catchments should have direct implications for deep-water sediment delivery  
19 (Collier et al., 2000; Blum & Hattier-Womack, 2009; Armitage et al., 2011; Romans et al., 2016; Watkins  
20 et al., 2018; Sømme et al., 2019; Tofelde et al., 2021). Although changes in sedimentation rate in deep-  
21 water syn-rift depositional systems are recognised or interpreted (Guitierrez-Pastor et al., 2009; Nelson  
22 et al., 2009; Pechlivanidou et al., 2018; McNeil et al., 2019a), the interplay of external factors that control  
23 changes in sediment flux are seldom well constrained. Changes in climate are a fundamental control  
24 on sediment flux from drainage catchments, either through changes in precipitation patterns or  
25 magnitude, or through resultant changes in catchment character such as vegetation (Leeder et al.,  
26 1998; Collier et al., 2000; Bogaart et al., 2002). However, the way these factors interact to govern  
27 sediment flux to the deep-water, and how confidently they can be inverted from stratigraphy remains  
28 unclear.

29 Environmental signals are defined by Tofelde et al., (2021) as '*a measurable change in any sedimentary*  
30 *parameter of interest through time that can be linked to an environmental change*'. However,  
31 environmental signals resulting from changes in catchment sediment flux to be recorded in deep-water  
32 stratigraphy can be modified by sediment transport processes or buffered by transient, up-dip storage  
33 (Jerolmack & Paola, 2010; Simpson & Castellort, 2012; Armitage et al., 2013; Watkins et al., 2018;  
34 Staub et al., 2020). The growth and death of extensional faults can additionally impact sediment routing  
35 patterns, and either inhibit or promote siliciclastic delivery to the deep-water (Gupta et al., 1999; Nelson  
36 et al., 2009; Gawthorpe et al., 2018; Geurts et al., 2018; Pechlivanidou et al., 2019). Typically, tectonic  
37 changes operate on  $10^5$ - $10^6$  yr timescales (e.g. Allen et al., 2008; Romans et al., 2016, Ford et al.,

38 2016; Gawthorpe et al., 2018), whereas climatic variability can be identified on higher order,  $10^4$ - $10^5$  yr  
39 timescales (e.g. Collier et al., 2000; Nelson et al., 2009; Allen et al., 2008; Blum & Hattier-Womack,  
40 2009; Watkins et al., 2018; Sømme et al., 2019). The overlap in the timescales for these controls, makes  
41 determining relative influences of climate and tectonics on stratigraphy challenging, especially in under-  
42 filled deep-water basins (Allen et al., 2008; Whittaker et al., 2010, 2011; Armitage et al., 2011; Romans  
43 et al., 2016; Sømme et al., 2019). The difficulty of confident palaeoenvironmental reconstruction,  
44 against comparatively more accessible and certain structural mapping, may mean that many  
45 depositional models tend to favour tectonics as a principal driving force, even at  $10^4$ - $10^5$  yr timescales.  
46 However, numerical modelling and quantitative sediment volume reconstructions have demonstrated  
47 that non-tectonic sediment supply variability has the potential to dramatically alter the stratigraphy within  
48 rift basin-fills, and this complexity should be included in conceptual models for deep-water syn-rift  
49 systems (Leeder et al., 1998; Collier et al., 2000; Barrett et al., 2017; Armitage et al., 2018; Watkins et  
50 al., 2018; Tofelde et al., 2021).

51 Climate and related changes in vegetation impart a major control on sedimentary parameters (e.g. grain  
52 size and shape), and the extent and duration of sediment erosion and transport (Leeder et al., 1998;  
53 Collier et al., 2000; Blum & Hattier-Womack, 2009; Kneller et al., 2009; Nelson et al., 2009; Bourget et  
54 al., 2010a,b; Armitage et al., 2011; Watkins et al., 2018, McNeil et al., 2019a). However, the dynamic  
55 response of catchments to climatic change is poorly understood and difficult to reconstruct (Cordier et  
56 al., 2017). Climatic modelling (Leeder et al., 1998; Armitage et al., 2011, 2013), eroded and offshore  
57 sediment volumes (Collier et al. 2000; Watkins et al., 2018), and drainage modelling (Pechlivanidou et  
58 al., 2019) highlight that diverse climatic regimes and drainage configurations in rift catchments make  
59 the potential mechanisms for variable sediment production and carrying capacity extremely broad. The  
60 role of vegetation as a control on sediment flux to the deep-water is largely unexplored beyond  
61 numerical models (Leeder et al., 1998; Schmid et al., 2018) with relatively few paired examples where  
62 the source-to-sink configuration can be confidently constrained (Collier et al., 2000; Cheng et al., 2017).

63 Here, we use exposures and a fully cored research borehole to identify the palaeoenvironmental  
64 controls on sediment flux to an exhumed, Early-Mid Pleistocene, deep-water system, in the West  
65 Xylokastro Fault Block (WXFB) of the Corinth Rift, Greece. Climatic fluctuations in the Corinth Rift  
66 through the Pleistocene and Holocene are well documented (Collier et al., 2000; Watkins et al., 2018;  
67 Barrett et al., 2019; McNeil et al., 2019a), although contrasting interpretations of glacial- (Collier et al.,  
68 2000) or interglacial-dominated (Watkins et al., 2018) sediment supply to the deep-water have been  
69 suggested. Stratigraphic correlations permit the architectures observed in the up-dip, fan delta feeder  
70 system to be tied to palynological palaeoenvironmental proxies in the deep-water stratigraphy using an  
71 age model generated through palaeomagnetic and tectonostratigraphic methods. This is compared with  
72 other Corinthian and Mediterranean climatic records and deposits in order to 1) test the reliability of  
73 complex, non-ideal, deep-water stratigraphic successions as records for Quaternary environmental  
74 change, 2) investigate the response of the deep-water syn-rift systems to Quaternary climatic and  
75 vegetation variability on  $10^4$ - $10^5$  yr timescales, and 3) propose new conceptual models for  
76 palaeoenvironmental controls on sediment supply to ancient deep-water syn-rift systems.



## 78 2 Geological Setting

79 The Corinth Rift is an active E-W-striking basin initiated ~5 Ma in response to NNE-SSW extension  
80 associated with the subduction and roll-back of the African plate beneath the European and Anatolian  
81 plates (Doutsos & Poulimenos, 1992; Collier & Dart, 1991; Armijo, 1996; Leeder et al., 2003; McNeil et  
82 al., 2005; Bell et al., 2009; Skourtsos & Kranis, 2009; Taylor et al., 2011; Beckers et al., 2015; Nixon et  
83 al., 2016). In the study area (Figure 1), the uppermost pre-rift stratigraphy is represented by a ~1.3 km  
84 thick succession of Mesozoic carbonates and Cenozoic siliciclastics arranged in ~N-S-striking, west-  
85 verging thrust sheets related to the Hellenide thrust belt (Piper, 2006; Skourtsos & Kranis, 2009; Ford  
86 et al., 2013; Skourtsos et al., 2016; Gawthorpe et al., 2018). Gawthorpe et al. (2018) subdivided the  
87 syn-rift stratigraphy of the southern margin into two main phases: i) Rift 1, 5.0-3.6 to 2.2-1.8 Ma, within  
88 dispersed, localised depocentres filled by early syn-rift alluvial and fluvial deposits, with a younger  
89 Gilbert-type fan delta and deep-water component, and ii) Rift 2, 2.2-1.8 Ma to the present day, which  
90 comprises localised, but partially connected, depocentres with Gilbert-type fan deltas and associated  
91 deep-water deposits (Collier & Dart, 1991; Rohais et al., 2008; Backert et al., 2010; Gobo et al., 2014;  
92 Barrett et al., 2019; Gawthorpe et al., 2018; Muravchik et al., 2020; Cullen et al., 2020). The Rethi-  
93 Dendro Formation (RDF – Leeder et al., 2012) of the Rift 2 phase is exposed in the West Xylokastro  
94 Fault Block (WXFB) on the southern margin of the Gulf of Corinth (Figure 1). The WXFB is a ~12 km  
95 long, 6-8 km wide fault terrace bound by the E-W-trending West Xylokastro Fault to the south, and the  
96 E-W Derveni and NW-SE-trending Lykoporiá Faults to the north (Figure 1). The RDF in the study area  
97 comprises an axial, delta-derived system, and a transverse fault-scarp apron system (Gawthorpe et al.,  
98 2018; Cullen et al., 2020). Palaeocurrents and the inclusion of metamorphic clasts indicate the main  
99 source of sediment input is from the Ilias fan delta fed by the well-established Olvios drainage catchment  
100 (Rohais et al., 2007a; Gobo et al., 2014, 2015; Rohais & Moretti, 2017; Rubi et al., 2018; Gawthorpe et  
101 al., 2018; Zhong et al., 2018; Cullen et al., 2020). An age of ~1.5 Ma – 0.7 Ma is established for this  
102 stratigraphy but is limited by low biostratigraphic resolution internally (Ford et al., 2016; Gawthorpe et  
103 al., 2018). Early-Mid Pleistocene palaeogeographies of the Olvios catchment indicate approximately  
104 1600 m of elevation difference from the uppermost hinterland of Mavron Oros to the topsets and  
105 shoreline of the Ilias fan delta over a distance of ~15-18 km (Gawthorpe et al., 2018, de Gelder et al.,  
106 2019).

107 Ilias fan delta foreset heights indicate that water-depth at the western end of the WXFB was >300-400  
108 m, increasing to ~500-600 m in the centre of the fault segment demonstrated through the elevation  
109 difference in time equivalent stratigraphy, extrapolated sedimentation rates and times of abandonment  
110 (Rohais et al., 2007; Gobo et al., 2014, 2015; Ford et al., 2016; Gawthorpe et al., 2018; Rubi et al.,  
111 2018; Zhong et al., 2018; Cullen et al., 2020). Topset radii of the Ilias fan delta are difficult to constrain  
112 due to faulted stratigraphy and later erosion, but exposures suggest they were likely <3.5 km (Rohais  
113 et al., 2007a,b, 2008; Rubi et al., 2018; Zhong et al., 2018; Cullen et al., 2020), similar to modern fan  
114 deltas along the southern shoreline. Key surfaces define a stratigraphic framework subdivided into the  
115 Lower WX and the Upper WX (Figure 1). This study focuses on the Lower WX, itself subdivided into

116 WX1-WX7 (Figures 1 to 4, Cullen et al., 2020). The G4 borehole (Figure 1, 2), drilled in January 2018  
117 as part of the Syn-Rift Systems project, is situated within the basin-floor domain, 3 km from the West  
118 Xylokastro Fault and ~6 km downdip of the Ilias fan delta (Cullen et al., 2020; Figure 1). The borehole  
119 intersects 172 m of RDF stratigraphy, mostly of the axial depositional system in the hangingwall of the  
120 West Xylokastro Fault.

121 **FIGURE 1: Location map**

122 **FIGURE 2: Correlation**

### 123 **3 Methodology**

#### 124 **3.1 Outcrop and core sedimentology**

125 The G4 research borehole located near Skoupéika/Kalitheia (Figure 1) retrieved a 172 m cored section,  
126 which is integrated with outcrop logging and digital outcrop models. 87% of the core showed good or  
127 excellent recovery. The stratigraphy for the West Xylokastro Fault Block RDF was developed through  
128 conventional stratigraphic and structural mapping supported by digital outcrop models outlined in Cullen  
129 et al. (2020). The G4 borehole core was logged at 1:50 scale in Greece prior to splitting and the  
130 collection of palynological and palaeomagnetic samples from the core. The core was then logged in  
131 greater detail (1:10) to provide a detailed sedimentological record to aid with the positioning of  
132 stratigraphic horizons and complement palaeoenvironmental and chronostratigraphic analysis.

#### 133 **3.2 Digital outcrops**

134 The digital outcrop model for the Skoupéika exposures was generated using photographs from DJI  
135 Mavic Pro and DJI Phantom 3 Uncrewed Aerial Vehicles, with photogrammetric models built using  
136 Agisoft Photoscan Pro (now Agisoft Metashape) with interpretation in LIME (Buckley et al., 2019).  
137 Multiple orthogonal and oblique photographs were used to maximise coverage and resolution of the  
138 model. The inaccessibility of much of the outcrop meant that ground-control points were not available  
139 but consistency within the model was checked through control points compared against topographic  
140 maps of the outcrop area. Field-based stratigraphic correlations (Cullen et al., 2020) were mapped onto  
141 the model as horizons. The 3D nature of the exposure permits confident dip projections of surfaces to  
142 the wellbore, initially as an unconstrained dip projection, then constrained with greater confidence by  
143 “well-top” interpretations from core logging (Figure 3, 4, Supplementary Information 3).

144 **FIGURE 3: Summary of outcrops and well data**

#### 145 **3.3 Palaeomagnetic analysis**

146 Seventeen samples were collected for palaeomagnetic analysis, preferentially from mudstones  
147 approximately every 20 m +/- 1 m in the core and, where available, from outcrops (Supplementary Data  
148 1, 2). Samples were cut into 8 cm<sup>3</sup> cubes marked with a way up indicator from the vertical well, or  
149 vertically aligned way-up arrows from outcrop samples, where bedding never exceeded a dip of 20°.  
150 The samples were then subject to alternating field (AF) demagnetisation with an AGICO LDA5 AF  
151 demagnetiser using 12-14 AF increments from 5 to 120 mT. Natural remanent magnetization and

152 remanence after each demagnetization step were measured with an AGICO JR5 spinner  
153 magnetometer at the PUMA Rock Magnetic laboratory, University of Birmingham. Demagnetization  
154 data were plotted on orthogonal (Zijderveld) diagrams, and the remanence components were calculated  
155 through principal component analysis (Kirschvink, 1980) using online software paleomagnetism.org  
156 (Koymans et al., 2016) (Supplementary Data 1, 2). Sample depths and locations are summarised in  
157 Figure 2 and 3 and the supplementary information. The directions (inclination) of the isolated  
158 characteristic remanent magnetization (ChRM) directions were used to produce a magnetostratigraphy,  
159 which was then compared to the Geomagnetic Polarity Time Scale (Cande & Kent, 1995; Cohen &  
160 Gibbard, 2016) to produce an age model for the studied stratigraphic intervals.

### 161 3.4 Palynology

162 Palynology samples were collected from core every ~10 m with slight deviations to achieve good quality  
163 sample material (Supplementary Material 1,4). Intact, mudstones were preferentially sampled in order  
164 to achieve the greatest likelihood of the preservation of undamaged organic material (Paropkari et al.,  
165 1992; McNeil et al., 2019c). Samples were prepared using the method of Vidal (1988). Samples were  
166 dried at 50° C, weighed then crushed and spiked with a *Lycopodium* tablet and minor amount of distilled  
167 water to cover the sample. 20% hydrochloric acid (HCl) was then added until the reaction had ceased  
168 and was topped up with water and left to settle for at least 12 hours. The supernatant liquid was then  
169 sieved through a 10 µm cloth sieve and returned to the beaker. 50 ml of 40% hydrofluoric acid (HF) was  
170 then added and stirred and left for 48 hours. This was neutralised by topping up and sieving with water  
171 prior to simmering in 20% hydrochloric acid to remove precipitates. This solution was then re-sieved  
172 with distilled water to bring to neutral. Where precipitates remained, HCl or HF stages were repeated  
173 until all precipitates were removed before mounting on slides in glycerine jelly.

174 In total, 20 samples were counted for pollen, dinoflagellates and other sedimentary organic matter using  
175 a Leica DM500 light microscope at 400-630x magnification. Pollen grain and dinoflagellate cyst  
176 identification was based on Chester & Raine (2001), Beug (2015) and Mudie et al. (2017). Sedimentary  
177 Organic Matter (SOM) is grouped into three, broad categories; Amorphous Organic Matter (AOM); Non-  
178 Terrestrial Palynomorphs (NTP) comprising marine algae, acritarchs and zoomorphs (foraminiferal test  
179 linings); and Terrestrial Palynomorphs (TP) comprising freshwater algae (*Botryococcus*), cuticle and  
180 unstructured phytoclasts, resin, degraded wood, dark structureless organic matter (DSOM) and bladed  
181 and equant organic debris (Tyson, 1996, McArthur et al., 2016a, b). All types of non-palynomorph  
182 organic matter were counted to a minimum of 300 in the classification of McArthur et al. (2016a, b).  
183 Dinoflagellate cyst counts vary considerably and a minimum count criterion for some samples could be  
184 met with mean count of 34 (varying from 1 to 212). Most pollen samples were counted until at least 250  
185 grains to exceed the ranges typical for validity in Quaternary lacustrine studies (Djamali & Cilleros,  
186 2020). However, four samples were deemed barren for pollen, dinoflagellates and spores, with an  
187 additional sample showing a very low count and poor preservation of material (Supplementary Data 4).  
188 Pollen percentages for vegetation groups were calculated based on a pollen sum excluding i) Pinaceae,  
189 which are variably over-represented through the stratigraphy due to their long-distance transport (*sensu*  
190 Szczepanek et al., 2017), and ii) aquatics, due to their potential for different transport mechanisms. For

191 both pollen and dinoflagellates, concentrations were calculated using the *Lycopodium* exotic marker  
192 method (Supplementary Data 4) established by Benninghoff (1962) and Stockmarr (1971) and  
193 summarised in Mertens et al. (2012b) and Nguyen et al. (2013). The average pollen concentration was  
194 577.9 grains/gram of sediment (Supplementary Data 4) ranging from 2294 grains/gram to 65.9  
195 grains/gram for countable samples; barren samples showed between 0 - 20.7 grains/gram.

196 To allow for cross-comparison between age-equivalent pollen records published in the area, pollen data  
197 were also grouped (Figure 10) following the grouping of Joannin et al. (2007a, b, 2008). As in Joannin  
198 et al. (2007b, 2008) *Quercus ilex* type, *Phillyrea* and undifferentiated *Oleaceae/Olea* are treated as a  
199 Mediterranean Elements sum, and separately from deciduous trees/mesothermic elements due to their  
200 local importance. Given their potential importance in highlighting semiaquatic grass populations,  
201 *Phragmites* sp. are distinguished from the rest of Poaceae based on their typically smaller size (<27  
202 µm) than other grains of the family (Chester & Raine, 2001). It is acknowledged that local or seasonal  
203 variability may produce unavoidable false-positive identification of *Phragmites* sp. In this case, the low  
204 concentrations *Phragmites* sp. and high concentrations of Poaceae means the impact of this on the  
205 total “Grasses” population is negligible.

206 In addition, ‘biomization’ (Prentice et al., 1996) allows a semi-quantitative comparison of the pollen data  
207 from this study to newer Mediterranean vegetation biome schemes. Here, we use the plant functional  
208 types and biomes of Marinova et al. (2018) derived for the Eastern Mediterranean and Southern  
209 Balkans supplemented with the plant functional types of Panagiotopoulos et al. (2020) for *Tsuga* to  
210 produce biome affinities for the following biomes (Supplementary Information 5):

- 211 • Tundra (TUND)
- 212 • Desert (DESE)
- 213 • Graminoids with Forbs (GRAM)
- 214 • Xeric Shrubland (XSHB)
- 215 • Warm-temperate evergreen sclerophyll broadleaf shrubland (WTSHB)
- 216 • Cool/Cold evergreen needleleaf forest (COOL/CENF)
- 217 • Warm-temperate/Temperate deciduous malcophyll broadleaf forest (WTDF/TEDE)
- 218 • Cool-mixed evergreen needleleaf and deciduous broadleaf forest (CMIX)
- 219 • Warm-temperate evergreen needle and sclerophyll broadleaf forest (WTEF)
- 220 • Evergreen needleleaf woodland (ENWD)
- 221 • Deciduous broadleaf woodland (DBWD)

222 To determine the affinity of a given assemblage, pollen taxa are organised into ‘plant functional types’  
223 (PFTs) and arranged into a taxon x PFT matrix. Marinova et al. (2018) provide data to support the  
224 transformation of a taxon x PFT matrix to a taxon x biome matrix to establish an association between a  
225 given taxa, and a vegetation biome. Using these matrices and the approach of Prentice et al. (1996),  
226 an affinity score for a pollen sample is generated for each biome (Supplementary Information 5). The  
227 pollen sum used for the biomization does not exclude Pinaceae to not artificially reduce or enhance the  
228 affinity towards certain biomes. The square-root operation stabilizes variance and increases the

229 methods sensitivity to less abundant taxa such that the variable over-representation of Pinaceae is  
230 accounted for (Prentice et al., 1996).

#### 231 **4 Stratigraphy**

232 The West Xylokaastro RDF comprises seven units (WX1-7), bound by key stratal surfaces that are traced  
233 from the Ilias fan delta foresets, over 8 km downdip into the deep-water basin floor stratigraphy at the  
234 G4 borehole (Cullen et al., 2020). **Figures 3 and 4** highlight the stratigraphy in the region surrounding  
235 the G4 borehole and the lateral variability, showing 10-20% variations in the percentage of sandstone  
236 and conglomeratic lithofacies over distances of 100-400 m. WX1 comprises calcareous mudstones in  
237 both the basin floor and up-dip Ilias delta. This is overlain by a coarser grained package, WX2, which  
238 thins and pinches out to the south in the G4 locality (**Figure 2,3**). WX2 comprises sandstone-rich and  
239 conglomeratic sheets and lenticular heterolithic packages in the basin floor, with highly variable  
240 conglomeratic and sandstone-rich scour-fills in the Ilias fan delta region. The overlying WX3 stratigraphy  
241 comprises sandstone- and conglomerate-rich broad, shallow, channel-fills interspersed with more  
242 lenticular but laterally extensive sandstone-rich heterolithics. WX3 is bound by its lower surface, Surface  
243 3, which deeply incises within a 7 km<sup>2</sup> area of the Ilias fan delta foresets and bottomsets marks a major  
244 change in sedimentary facies from interbedded sandstone and mudstone foresets to conglomerate-rich  
245 foresets (Cullen et al., 2020). Near G4, Surface 3 comprises a surface separating underlying calcareous  
246 mudstones (WX1) and sandstone- and conglomerate-rich channelised lobe deposits (WX3 – **Figure 3,**  
247 **4**, Cullen et al., 2020). Surface 4, the basal surface of WX4, marks a retrogradation of the Ilias fan delta,  
248 which is recognised by overlying back-stepping finer-grained (sandstone- and mudstone-rich) foresets,  
249 and corresponds to a downdip hiatus in coarse-grained siliciclastic supply to the deep-water (**Figure 3,**  
250 **4**, Cullen et al., 2020). WX4 forms a regionally extensive mud-rich marlstone dominated unit with rare  
251 shelly fauna in the otherwise non-fossiliferous G4 core. WX4 is capped by Surface 5, marked by  
252 downlap of WX5 foresets onto WX4 foresets and bottomsets, reflecting renewed progradation of the  
253 Ilias fan delta (Cullen et al., 2020). At the G4 borehole, Surface 5 is overlain by conglomeratic debrites  
254 and sandstone sheets interbedded with mudstone horizons typical of WX5. The vertical change from  
255 WX4 to WX5 is laterally variable, appearing in G4 as ~90 cm thick debrite, but 500 m to the north as a  
256 gradual increase in the number and thickness of sandstone beds (**Figure 3, 4**). Surface 6 (base WX6)  
257 is marked by an erosion surface in the bottomset of the Ilias fan delta, and an increase in the proportion  
258 of conglomerates that thin and lap onto the foreset (Cullen et al., 2020). Near G4, Surface 6 is identified  
259 by an overlying and extensive coarse-grained, conglomeratic package that marks the onset of  
260 alternations of decametric-scale, laterally extensive packages of sandstone- and gravel-rich  
261 stratigraphy interbedded with mudstones of WX6 (**Figure 3**). In the Ilias fan delta region, WX5 and WX6  
262 are exposed in the bottomsets, comprising laterally variable conglomeratic lenses, and elsewhere as  
263 sandstone-rich channel- and scour-fills. The base of WX7 is marked by a laterally extensive mass  
264 transport deposit of variable character that is overlain by sandstone sheets and mudstone intervals  
265 similar to WX5 and WX6 (Cullen et al., 2020).

266 In the region of the G4 borehole, three cliff faces (two orientated N-S and one north facing, NE-SW  
267 oriented cliff) produce a promontory near the village of Skoupéika (**Figure 1-4**, Cullen et al., 2020).

268 Present day structural dip is 10 - 15° eastward for much of the deep-water stratigraphy in the northern  
269 part of these cliffs, rotating to 15 - 20° southeastward around the G4 borehole. This forms a broad SSE-  
270 NNW striking anticline, approximately 500 m wide, dissected by smaller-scale faults in the region around  
271 logs 1 and 2 (Figure 3, 4), which we interpret formed above a blind intra-basinal fault, Minor Fault 1  
272 (Supplementary Information 3, Cullen et al., 2020). Stratigraphic thinning of WX2 and WX3 toward this  
273 blind fault tip (Figure 4) supports the presence of a minor bathymetric high generated by the blind fault  
274 during WX2 and WX3 deposition (Cullen et al., 2020). The southward thinning means WX2 is likely  
275 absent or highly condensed in the G4 core. Subtle northward thinning of WX5 (and WX3) between logs  
276 3 and 5 may be a result of incipient growth of the Lykoporiá Fault and the inception of a bathymetric  
277 high to the north of the section (Cullen et al., 2020). Observations of intra-basinal structures <1 km to  
278 the footwall of, and co-planar with, the Lykoporiá Fault that affect younger stratigraphy (in WX7, WX8)  
279 support this interpretation (Figure 1, 2, Cullen et al., 2020).

280 **FIGURE 4: Correlation panel of Skoupéika West Outcrop Panel to G4.**

## 281 **5 Magnetic Chronostratigraphy**

282 Biostratigraphy (low resolution palynology and macrofauna ranges) and tectonostratigraphy based on  
283 the topset elevations of laterally equivalent fan deltas and uplift rates for the southern margin of the Gulf  
284 of Corinth, place the Ilias fan delta system and downdip RDF stratigraphy to be ~1.5-0.7 Ma  
285 (Symeonidis et al., 1987; Muntzos, 1992; Armijo, 1996, Westaway, 2002; Malartre et al., 2004; Rohais  
286 et al., 2007a; Ford et al., 2007, 2013, 2016; Nixon et al., 2016, Gawthorpe et al., 2018). Syn-  
287 deformational calcite cements dated from the West Xylokastro Fault indicate activity on the West  
288 Xylokastro Fault at ~1 Ma (+/- 0.1 Ma) (Flotte et al., 2001; Causse et al., 2004), however such cements  
289 can be precipitated during various periods of the lifetime of a fault and do not constitute an upper  
290 boundary age condition. The youngest part of the West Xylokastro RDF is likely to coincide with the  
291 migration of activity from the West Xylokastro Fault to the Derveni and Lykoporiá Faults, which is  
292 estimated to have become the main active border fault at ~0.75 Ma (Bell et al., 2009; Nixon et al., 2016;  
293 Gawthorpe et al., 2018). Northward migration of fault activity may have been protracted, as timing of  
294 drainage reversals on the southern rift margin associated with this are known to range from 0.7-0.5 Ma  
295 (Ford et al., 2007; Gawthorpe et al., 2018; Fernández-Blanco et al., 2019, 2020; de Gelder et al., 2019).

296 Palaeomagnetic analyses from the G4 borehole and outcrop samples revealed six magnetozones  
297 within the West Xylokastro stratigraphy (Figure 3, 5). Two sections of normal (MAG1, MAG2) and  
298 reverse polarity (MAG0, MAG4) can be identified at the lower and upper parts of the stratigraphy,  
299 respectively (Figure 5). Within the ~1.5 – 0.5 Ma age range constrained by previous tectonostratigraphy  
300 and biostratigraphy, there are three > 20kyr periods of normal polarity; the Brunhes chron (0-773 kyr),  
301 the Jaramillo sub-chron (990-1001 to 1069-1071 kyr) and the Cobb Mountain sub-chron (1189-1221  
302 kyr) (Figure 5). Shorter intervals of normal polarity (i.e. magnetic excursions) also exist and correspond  
303 to the Kamikatsura (900 kyr) and Santa Rosa (932 kyr) excursions.

304 An actively growing hanging wall depocenter north of the Lykoporiá Fault has been demonstrated from  
305 ~0.75 Ma (Nixon et al., 2016; de Gelder et al., 2019). This activity continued to the present day with



306 uplift in the footwall of the Lykoporiá Fault acting to exhume the West Xylokastro RDF to its present-  
307 day position. The northward stratigraphic thinning within WX4 and WX5 across the northern part of the  
308 Skoupéika West outcrop panel (Figure 3, 4) is interpreted to reflect the onset of the earliest part of  
309 Lykoporiá Fault activity, where it formed a bounding topographic high to the West Xylokastro  
310 depositional system (Nixon et al., 2016; Gawthorpe et al., 2018; Cullen et al., 2020). As WX1 and WX2  
311 was determined to be unaffected by the Lykoporiá Fault (Section 4), the MAG 1 normal polarity  
312 magnetozone should be older than ~0.75 Ma. The occurrence of a relatively thick reverse polarity  
313 magnetozone above MAG1 (i.e., MAG4) excludes the latter from being correlated with the, and Bruhnes  
314 normal polarity chron.

### 315 **Figure 5: Palaeomag ties to magnetostrat boundaries**

316 In the absence of absolute stratigraphic ages (e.g. dated tephra), magnetostratigraphic logs can provide  
317 multiple, alternative age interpretations, as palaeomagnetic highlighted in Figure 6. The choice of the  
318 presented palaeomagnetic interpretation (MAG 1 = Jaramillo sub-chron) is in agreement with i) regional  
319 palaeogeography, ii) required exhumation/uplift rate, iii) rationality of sedimentation rates and/or  
320 variability, and iv) palaeomagnetic certainty (or variability thereof). In this instance, palaeomagnetic  
321 certainty relates to how likely the spot-sampling method would identify a given reversal, and/or how  
322 densely sampled a given magnetic chron is. With the exception of the Olduvai alternative, MAG1  
323 Jaramillo, Cobb Mountain and Bruhnes interpretations fit within the broad, possible age range (~1.8 Ma  
324 – ~0.6Ma) for the RDF in the West Xylokastro Region (Ford et al., 2016; Gawthorpe et al., 2018; Figure  
325 6). A “Bruhnes Alternative” (Option 4 on Figure 6) can easily be ruled out as it would require the ~80m-  
326 thick MAG4 interval to have deposited within the ~10ky-long “Stage 17” excursion (Singer, 2014), hence  
327 providing an unrealistic sedimentation rate as high as 8m/kyr or even more. Where MAG1 is tied to  
328 longer intra-Matuyama sub-chrons (i.e., Olduvai and Cobb Mountain) f sedimentation rate variability  
329 would need to be extreme in order to fit palaeomagnetic data, and in cases outside typical values for  
330 similar settings of the Corinth Rift (0.2 m/kyr – 2.5 m/kyr as extremes; Ford et al., 2016; Sergiou et al.,  
331 2016; McNeil et al., 2019a). The estimated exhumation rate of the Likoporia Fault footwall to put the  
332 RDF at its present day position required for the oldest (Olduvai) alternative (~0.4 mm/yr) is substantially  
333 slower than that established for this region of the southern coastline (1.3-1.5 mm/yr - Armijo et al., 1996;  
334 Taylor et al., 2011; Ford et al., 2014, 2016; Rohais & Moretti, 2016; de Gelder et al., 2019). Although it  
335 is probable that past uplift rates were slower, during the early life of the Lykoporiá Fault, so this criterion  
336 alone is uncertain. However, if this were the case, such an uplift rate would place beach terrace deposits  
337 that lie unconformably on the RDF as significantly older (~750 ka) than elevation equivalent beach  
338 terraces to the east with confirmed U/Th dating (maximum 600 ka, Armijo et al., 1996). As a result, the  
339 chosen interpretation relies on MAG1 tying to the Jaramillo sub-chron, which yields sediment  
340 accumulation and uplift rates, and palaeogeographies, which agree with those established in the Corinth  
341 Rift, and has a reasonable palaeomagnetic certainty. This interpretation is further supported by the  
342 likely correlation of the short MAG3 normal polarity interval with the Santa Rosa excursion (Figure 5).

### 343 **Figure 6: Palaeomag equivocal alternatives**

344 Two hundred metres of younger RDF stratigraphy is preserved as the Upper WX (Cullen et al., 2020).  
345 Extrapolating the preferred uppermost sediment accumulation rate estimated from the palaeomagnetic  
346 ties for MAG 4 gives an age of ~0.6 Ma for the top of the preserved West Xylokastro RDF stratigraphy  
347 in the study area. Internal to these upper and lower boundaries, the positioning of stratigraphic units  
348 needs to account for condensed sections. Unit WX2 is absent, or condensed, at the base of WX3 as a  
349 composite of WX2 and Surface 3 within the G4 borehole stratigraphy (Figure 3). Using the nearby G4  
350 borehole sediment accumulation rate from analogous MAG1 (0.65 m/kyr) or MAG2 (0.42 m/kyr), and  
351 thickness of WX2 at its thickest point nearby (~15 m in Log 6 in Figure 3), WX2 is interpreted to  
352 correspond to a ~23 kyr–36 kyr duration. The preferred duration is the shorter model, given the greater  
353 similarity of stratigraphy within MAG1 to that of MAG2, which contains a basin wide mudstone interval  
354 separating coarse-grained scour-fill prone stratigraphy, rather than the alternations between mudstones  
355 and laterally extensive conglomeratic debrites and mudstones within MAG1.

356 The chronostratigraphic placement of the West Xylokastro Fault Block stratigraphy places it equivalent  
357 to the lower offshore unit penetrated at IODP 381 Site M0078 (Unit 1 - Nixon et al., 2016; Unit 2 - McNeil  
358 et al., 2019a-f) and provides one of the first demonstrable chronostratigraphic ties between the onshore  
359 and offshore stratigraphy in the Gulf of Corinth. Chronostratigraphy established through the  
360 palaeomagnetic record also allows context for the likely frequency recorded by palynological sampling,  
361 which averages 1 sample per 20kyr, although this rate does show minor deviations to maintain good  
362 sample quality. This means the palaeoenvironmental record will not accurately characterise higher-  
363 frequency variability (~10<sup>3</sup> kyr).

## 364 6 Palynology

### 365 6.1.1 Palynofacies analysis

366

367 All palynological samples plot within the proximal, terrestrially-influenced part of a palynofacies ternary  
368 plot (Figure 7a, b, *sensu* Tyson, 1996, Zobia et al., 2015). An enlargement of the upper 20% of the  
369 ternary plot (Figure 7b) highlights that very minor marine/brackish influences are typically within  
370 mudstone-rich units (WX4 and WX1) or more heterolithic units (WX5/6). These are expressed as minor  
371 (<5%) occurrences of AOM and marine algae (Supplementary Information 4), dinoflagellates, and a  
372 coincident reduction of freshwater algae and/or terrestrial matter. Figure 8 provides further detail on the  
373 types of organic matter preserved and highlights consistently high cuticle/unstructured phytoclasts and  
374 woody/equant/bladed debris comprising 40-70% of the organic matter. There is no observable cyclicity  
375 in this organic matter type or distribution, and variability is generally pulsed (rather than cyclical waxing  
376 or waning variability). Pulses of freshwater algae (*Botryococcus*) are noted at the onset of WX6 and are  
377 at their lowest during mudstone dominated WX1 and WX4, and sandstone-rich WX5. Within WX7, very  
378 high proportions of equant debris and degraded wood are recorded with far less cuticle than in lower  
379 parts of the succession.

380 The dominance of terrestrial palynomorphs, and the lack of strong marine influence indicators, agrees  
381 with previous studies that interpret the first phase of the Late Pleistocene Gulf of Corinth as a largely  
382 isolated freshwater to brackish body: “Lake Corinth” (Rohais et al., 2008, Gawthorpe et al., 2018, McNeil



383 et al., 2019a, f). In WX4 and WX5, possible marine indicators such as AOM and NTP remain below the  
384 2% of the SOM at their highest level in the stratigraphy. NTP (e.g. Marine Algae, Acritarchs and  
385 Zoomorphs), when present, are found in very low numbers, and detailed identification was not possible.  
386 As a result, minor presences of NTP cannot be considered as indicative of marine conditions given the  
387 overwhelmingly freshwater signature even where they are present. However, we cannot exclude that  
388 this may be indicative of some presence of partly mixed or weakly brackish conditions due to the level  
389 of poor preservation of acritarchs present. Given the co-occurrence with more strongly represented  
390 *Spiniferites cruciformis* (Figure 8), pulses of NTP may be related to minor salinity variations due to  
391 increased freshwater/terrigenous influx (Kouli et al., 2001; Mudie et al., 2017) comprising rarer  
392 freshwater acritarchs, however this cannot be confirmed. The intra-WX7 switch to equant  
393 debris/degraded wood dominated organic assemblages is interpreted as results of depositional  
394 palynofacies variation (McArthur et al., 2016a, b) corresponding with change from lobate/weakly  
395 confined deposits to more channelised stratigraphy within WX7 (Cullen et al., 2020).

### 396 **Figure 7: Ternary plots and Figure 8: SOM Plots**

#### 397 **6.1.2 Dinoflagellates and non-pollen palynomorphs (NPP)**

398

399 The maximum number of co-existent dinoflagellate taxa is 11, with most samples typically showing 3 –  
400 5 taxa (Figure 9). *Spiniferites* spp. and *Spiniferites cruciformis* exhibit the highest abundances as peaks  
401 within WX1, near the top of WX4, within WX5, and near the base of WX6. Other dinoflagellate cyst taxa  
402 occurrences also increase in samples with high *Spiniferites* spp. counts but are typically lower in  
403 abundance. During WX5 and WX6, high abundance of *Spiniferites* spp. is coincident with increases in  
404 freshwater algae (Figure 7, Supplementary Information 4). In contrast, during WX3 when *Spiniferites*  
405 spp. counts are substantially lower, there is an increased presence of *Impagdinium*, *Gymnodinium* and  
406 *Ataxiodinium choane* cysts. Acritarchs are rare in most samples, and where present are poorly  
407 preserved, meaning their genera cannot be identified.

408 The variable presence and limited dinoflagellate diversity reflected by the relatively low number of taxa  
409 suggests that dinoflagellate populations may have been strained (Mudie et al., 2001). High  
410 concentrations of *S. cruciformis* and lower dinoflagellate diversity suggest the area was isolated from  
411 the Mediterranean Sea during this interval. Such almost monospecific dinoflagellate cyst assemblages  
412 are found in the lowest salinity, isolated intervals in the late Pleistocene Gulf of Corinth (McNeil et al.,  
413 2019a-f, Fatourou et al., 2021) in contrast to more diverse assemblages during marine connections  
414 (Collier et al., 2000; McNeil et al., 2019a-f). The co-presence of *S. cruciformis* and *Spiniferites* spp.  
415 accompanied with relative increases in freshwater algae (e.g. in WX5 in Figure 8), is in agreement with  
416 the recognised ability of *Sp. cruciformis* to withstand a variety of salinity conditions (Kouli et al., 2001;  
417 Mertens et al., 2012a; Mudie et al., 2001; McNeill et al., 2019e) and its characterisation as a ‘pioneer’  
418 taxa in strained or variable salinity environments such as the Black Sea corridor (Mudie et al., 2001;  
419 2010; 2017). Mudie et al. (2010) highlight that nutrient supply to the water-column rather than absolute  
420 lake-level and marine-connectivity controls *Spiniferites* spp. populations in lacustrine or ephemerally  
421 connected water bodies. As a result, variability in diversity and/or presence of dinoflagellate populations

422 may be linked to minor variations in salinity resultant from increased fresh-water influx to a given basin.  
423 Ultimately, the dinoflagellate and other non-pollen palynomorph signature is consistent with the entire  
424 G4 stratigraphy being deposited under lacustrine conditions, in agreement with the lower unit of IODP  
425 boreholes M0078 and M0079 in McNeil et al. (2019a-f).

## 426 **Figure 9: Dino Plots**

### 427 **6.1.3 Pollen assemblages**

428

429 **Figure 10** presents the pollen concentration data from the G4 borehole (**Supplementary information 4**).  
430 *Pinus* and Pinaceae are the most common taxa, except for minor periods when grasses (Poaceae,  
431 Cyperaceae) dominate the assemblages. The next most common taxa are Poaceae, Cyperaceae and  
432 subordinate Asteraceae, Cupressaceae/Taxodiaceae and *Plantago* sp. (**Figure 10c**). As with most  
433 Pleistocene pollen records, substantial variability exists in the abundance of arboreal pollen (Tzedakis  
434 et al., 2006; Joannin et al., 2007a,b; Okuda et al., 2008; Sadori et al., 2016). The assemblage is similar  
435 to most Pleistocene Mediterranean assemblages, although *Artemisia* is notably absent. Unlike other  
436 Mediterranean Pleistocene pollen records, *Quercus* makes up a comparatively minor component of  
437 arboreal pollen in the G4 stratigraphy (Tzedakis et al., 2006; Joannin et al., 2007a, b; Okuda et al.,  
438 2008; Sadori et al., 2016). Mediterranean elements are also very rare in the G4 record, similar to their  
439 scarcity in IODP 381 Corinth Rift palynological observations (McNeil et al., 2019a,b,e,f). Steppic  
440 elements, such as Chenopodiaceae or *Ephedra*, are present but rare, with aquatic elements  
441 (Potamogetonaceae, Sparganiaceae and *Nymphaea alba*) even rarer. Other herbaceous elements  
442 comprise flowering plants typical of, although not specific to, Mediterranean flora assemblages. Most  
443 commonly in this study these comprise Asteraceae, Caryophyllaceae, Saxifragaceae, Rosaceae,  
444 Dipsacaceae, Malvaceae and the relict taxon *T. sibiricum*.

445 Biome affinities (**Figure 10b**) are typical of Mediterranean flora in the large altitudinal range (0 – 1500  
446 m) which surrounds the modern Gulf of Corinth. Strongest biome affinities are towards with Graminoids  
447 with Forbs (GRAM), followed by cold and cool evergreen needleleaf forest (CENF and COOL),  
448 temperate deciduous malachophyll (TEDE), cool mixed evergreen needleleaf and deciduous  
449 broadleaf forest (CMIX), and warm-temperate evergreen needleleaf and sclerophyll broadleaf forest  
450 (WTEF). Non-forested biomes are strongly represented by graminoid grasslands (GRAM) and a more  
451 minor and variable xeric shrubland component (XSHB).

## 452 **Figure 10: Pollen Plots**

453 WX1 is largely characterised by high proportions of non-arboreal pollen, grasses and a diverse array of  
454 other herbaceous taxa. Arboreal pollen abundance varies between ~<250k grains/gram to more than  
455 1600 grains/gram with two distinct peaks. Arboreal pollen is dominated by *Pinus*, and more commonly  
456 Pinaceae Undiff. and *Abies* towards the uppermost part with deciduous trees being generally rare. Non-  
457 arboreal pollen mostly comprises Poaceae and other herbs (most commonly Asteraceae and  
458 *T.sibiricum* although the non-arboreal taxa present are diverse and variable). Steppic elements and  
459 Mediterranean elements are generally absent, with the exception of some rare representation in the

460 middle and upper part of the unit. The middle portion of the unit shows less coniferous arboreal pollen  
461 (most dramatically in *Pinus*) but the strongest presence of mesothermic trees (*Betula* and *Quercus*) and  
462 sclerophyllous (scrub) forms of herbaceous plants (e.g. Scrophulariaceae, and steppic elements). As  
463 a result, there is a weakened affinity towards temperate forested biomes in the middle part of WX1, with  
464 biome affinities stronger towards graminoid grassland and xeric shrubland (Figure 10b). In the upper  
465 part of WX1, grassland is dominant with a minor component of coniferous trees (especially *Abies*, *Picea*,  
466 *Juniperus* and other Cupressaceae). The uppermost part of WX1 has approximately equal affinities  
467 towards graminoid grassland (GRAM), cool evergreen needle leaf forest (CENF) and cool mixed  
468 evergreen needleleaf and deciduous broadleaf forest (CMIX) and evergreen needleleaf woodland  
469 (ENWD) suggesting a temperate-cool climate. Whilst the strong affinity towards forest throughout the  
470 unit indicates sufficient precipitation, increases in affinities within the middle of the unit to xeric biomes  
471 and sclerophyllous vegetation suggest potential periods of lower precipitation.

472 Overall, WX3 shows comparably lower arboreal pollen percentages and a dominance of non-arboreal  
473 pollen, rich in grasses (*Cyperaceae* and *Phragmites* sp.) and other herbs (*Asteraceae*, *Caryophyllaceae*).  
474 The arboreal pollen assemblage is dominated by conifers with mountainous/cold-tolerant taxa, such as  
475 *Abies* and more minor *Tsuga* (Figure 10). The conglomerate- and sandstone-rich lower-to-middle part  
476 of WX3 also shows peaks in steppic (*Chenopodiaceae*) and aquatic elements. Following this, there is  
477 an expansion of forest cover through the upper part of WX3, especially in deciduous trees (mainly  
478 *Quercus* and *Ulmus*) through the unit from <2% at its base to ~8% in the upper part of WX3. As a result,  
479 samples immediately prior to WX4 show strong affinities only towards forested biomes, some of which  
480 require warm or temperate climates (Figure 10b - e.g. WTEF). The lower part of WX3 is therefore  
481 interpreted to represent a mix of steppe/grassland vegetation initially with more minor forest cover  
482 typical of a colder, likely wetter climate associated with Pleistocene glacials in the Mediterranean (Collier  
483 et al., 2000; Tzedakis et al., 2006; Joannin et al., 2007a, b). This is followed by a warming in the  
484 transition from WX3 to WX4 is accompanied by a decrease of steppic and Mediterranean elements,  
485 suggesting an increase in precipitation supported by weakening affinities to grassland (GRAM),  
486 xerophytic shrubland (XSHB) and any desertification (DESE) indications.

487 Mudstone-dominated WX4 comprises a ~8 m section showing substantial differences between a mixed-  
488 arboreal-dominated lower part and a non-arboreal-dominated upper part with the arboreal percentage  
489 is dominated by deciduous trees (*Quercus* sp., *Ulmus* and *Fraxinus* sp.). The lower part of WX4 is  
490 dominated by arboreal pollen, which is largely conifer-dominated. Comparatively, the upper part of WX4  
491 records a substantial decrease in conifer pollen, as part of an overall 60% reduction in arboreal pollen  
492 from the onset of WX4 to the base of WX5. However, the mesothermic/deciduous proportion comprising  
493 *Quercus* and *Alnus* is remain low in the upper and lower part of WX4 (~3-5%). This marks a shift in the  
494 forest biome affinities from cool or cold-forest (e.g. CENF, COOL), with graminoid grassland (GRAM)  
495 in the lower part of WX4 towards more temperate mixed forest biomes (TEDE, CMIX, ENWD, DBWD)  
496 through to WX5 with maintained strong affinities towards graminoid grassland (GRAM). More subtle  
497 changes also exist, such as increased diversity of other herbaceous elements, with 10 co-existent taxa,  
498 but still dominated by *Asteraceae*. Whilst desert/xeric biomes (mainly represented by steppic elements)

499 remain relatively low these biomes, but approximately double their affinity from the onset of WX4 to the  
500 onset of WX5. The low values of DESE and XSHB likely reflect the lower pollen dispersal potential  
501 compared to Pinaceae and other arboreal taxa, but nevertheless show an increase during this time.  
502 The combination of the i) overall reduction in arboreal pollen, but maintenance of deciduous trees, ii)  
503 increase in xeric and desertification indicators, and iii) an absence of cold or humidity-demanding taxa  
504 such as *Abies*, is interpreted to reflected continued warming and drying, to a climate too warm, or too  
505 dry, to sustain widespread temperate or cool coniferous forest. This is similar to very warm/semi-arid  
506 episodes observed in severe interglacials in Early-Mid Pleistocene stratigraphy of Rhodes, Greece  
507 (Joannin et al., 2007b). This assemblage is maintained through much of the heterolithic but sandstone-  
508 rich WX5, with an absence of *Pinus* and very low counts of other Pinaceae. The uppermost 4-5 m in  
509 WX5 records a change, with increased coniferous arboreal pollen, and decreased mesothermic  
510 arboreal elements (*Quercus* sp.) indicative of return to a cooler, temperate or wetter climate, with a  
511 notable switch to strong affinities to CENF and COOL forest in addition to TEDE, CMIX and WTEF.

512 WX6 comprises approximately equal proportions of arboreal and non-arboreal pollen in the lowest  
513 sample and is more dominated by non-arboreal pollen at its top. The basal part of WX6 contains a  
514 diverse array of non-aboreal pollen and some of the largest abundances of aquatic and steppic  
515 elements through the G4 record. Initially this is accompanied by a minor, mixed arboreal proportion  
516 comprising *Quercus* sp., Tamaricaceae mesothermic/deciduous trees, and humidity demanding  
517 Pinaceae taxa, such as *Abies*. The upper part of the unit shows less conifers and grasses but similar,  
518 overall deciduous tree percentage (~5%), and is dominated by grasses and steppic and aquatic  
519 elements. Biome affinities to frost-intolerant or temperate biomes (e.g. WTEF) are low while affinities to  
520 grassland and xeric shrubland biomes appear increased. This is ultimately interpreted as continuation  
521 of the cooling at the end of WX5, to a colder and less-forested landscape. The MTD overlying WX6 is  
522 followed by more sparsely sampled and occasionally barren stratigraphy (Figure 10, Supplementary  
523 Information 4). Given the poor sample preservation within and above the MTD, we do not propose a  
524 confident climatic interpretation for WX7 stratigraphy on the basis of the G4 pollen record.

525 **Figure 11: Chronostrat summary**

## 526 **7 Discussion**

### 527 **7.1 Palaeoenvironmental evolution and sediment supply synthesis**

528 The boundaries of the six magnetozones are treated as fixed tie-points to allow the placement of the  
529 stratigraphic and palaeoenvironmental record in chronostratigraphic context (Figure 11a). In the  
530 absence of higher resolution or absolute chronostratigraphic constraints within these magnetozones,  
531 the stratigraphy within them is linearly interpolated according to the average sedimentation rates to  
532 meet the time-depth relationship of the G4 borehole and surrounding stratigraphy (Figure 11b). The  
533 uncertainty within the individual magnetozones is mitigated by the spacing of palaeomagnetic samples  
534 and their corresponding reversals, which means the chronostratigraphic resolution is greatly increased  
535 from previous studies in the Early-Mid Pleistocene stratigraphy onshore the Gulf of Corinth. As a result,  
536 we tentatively propose a new age model (Figure 11b). The duration of the magnetozones means linear

537 interpolation covers a variety of timespans, from roughly ~ 2 kyr for the Santa Rosa Chron (Yang et al.,  
538 2004) through to ~160 kyr for MAG 4 from the Santa Rosa Chron to the Bruhnes-Matuyhama Reversal,  
539 and a mean magnetozone duration of 75 kyr. This spacing of tie points governing linear interpolation is  
540 similar to that of many geological, coarser resolution climatic stratigraphic studies (e.g. examining  
541 variability on  $10^4$ - $10^6$ - $10^6$  yrs timescales) in complex stratigraphy (e.g. 20-60 kyr  $^{10}\text{Be}$  cosmogenic  
542 nuclide dating in D'Arcy et al., 2017; ~70 - 500 kyr  $\delta^{13}\text{C}$  and biostratigraphy in Castellort et al., 2017;  
543 50-100 kyr biostratigraphy in Sømme et al., 2019). A linear interpolation between the magnetic tiepoints  
544 in the absence of other chronostratigraphic data is favoured over a 'peak matching' of different  
545 resolution palynological records or sequence stratigraphic interpretations as stratigraphic surfaces  
546 within rift basins are commonly complex and diachronous due to interactions of local accommodation  
547 and supply variations (Gawthorpe et al., 1994; Rohais et al., 2008; Muravchik et al., 2018; Barrett et al.,  
548 2018, 2019). As a result, stratigraphic surfaces are placed honouring their interpolated  
549 magnetostratigraphic position rather than through a correlative interpretation with global sea-level or  
550 vegetation records. The chronostratigraphic resolution provided by the magnetostratigraphy and the  
551 correlation to deltaic stratigraphic architecture (Cullen et al., 2020) provides a marked improvement on  
552 the existing age-range of the West Xylokastro RDF and means previous stratigraphic interpretations  
553 can be complemented with potential palaeoenvironmental triggers. Given the range of the magnetozone  
554 from the Santa Rosa chron (0.932 Ma) to the Bruhnes-Matuyhama reversal (0.773 Ma) and the quasi-  
555 instantaneous emplacement of the MTD, the positioning of WX7 and the MTD remains highly uncertain.  
556 Table 1 summarises the previously proposed interpretation of surfaces, and the chronostratigraphic  
557 placement as a result of this study.

Surface	Proposed Interpretation (Cullen et al., 2020)	Chronostratigraphic position (Figure 11)
Surface 2 (Base WX2)	Forced regressive surface documented by widespread erosion in Ilias delta and increase in conglomeratic lithofacies	~1.01 Ma within MIS28 global sea-level fall or ~1.03 Ma at onset of MIS 29 global sea-level rise
Surface 3 (Base WX3)	Forced regressive surface documented by widespread erosion and chutes in Ilias delta and continued coarse-grained lithofacies	~0.99 Ma (MIS 28) during MIS28 at onset of global sea-level fall from MIS28 interstadial
Surface 4 (Base WX4)	Transgression documented by a back-stepping of delta foresets in the Ilias Delta and basin-wide dominance of mudstone-dominated stratigraphy	~0.96 Ma (MIS 26) during maximum rate of global sea-level rise to MIS 25
Surface 5 (Base WX5)	Maximum flooding surface marked by basinward downlap capping retrogradation of mudstone-rich WX4 stratigraphy	~0.95 Ma (MIS 25) during onset of global sea-level fall from MIS 25
Surface 6 (Base WX6)	Regressive surface documented by erosion in the Ilias delta and increase in conglomeratic lithofacies	~0.93 Ma (MIS 24) during highest rate of global sea-level fall to MIS 24

Surface 7 (Base WX7)	Possible transgressive surface, but weakly expressed as backstepping bottomsets onlapping onto foresets in Ilias delta	~0.91 – 0.87 Ma Highly uncertain due to MTD at G4 borehole
-------------------------	--	--

558 **Table 1: Chronostratigraphic placement of key stratigraphic surfaces proposed in Cullen et al.**  
559 **(2020)**

560 Coarse-grained delivery to the West Xylokaastro Fault Block occurs during WX2, WX3, WX5, WX6 and  
561 WX7 (Figure 11, Figure 12). The character of these coarse-grained units varies; WX2 is dominated by  
562 conglomeratic sheets and sand-rich weakly channelised lobe deposits; WX3, is less conglomeratic with  
563 more heterolithic stratigraphy but is dominated by sand-rich channelised lobe and sheet-like deposits.  
564 WX5, WX6 and WX7 show sandstone-rich, but heterolithic sheet-like and weakly channelised deposits  
565 and more substantial conglomeratic channels interbedded with laterally discontinuous (<300 m)  
566 mudstones (Cullen et al., 2020). WX7 is eroded into by conglomerate-filled channels in locations close  
567 to the basin-bounding fault (Cullen et al., 2020). The widespread absence of coarse clastic delivery  
568 during WX1 and WX4 compared to WX2 and WX3 (and the variability within WX6 and WX7) highlights  
569 variability in sedimentary parameters.

570 The absence of WX2 conglomerates in the G4 borehole reflects a structurally-controlled depositional  
571 variability. Elsewhere (Figure 2,3) this is a period of conglomerate delivery to the deep-water. Tzedakis  
572 et al. (2006) and Wagner et al. (2019) document arboreal pollen at Tenaghi Philippon measured at  
573 periods of time equivalent to pre-, syn- and post-WX2, which is in good agreement with the G4 record  
574 (~60% at the onset of MIS 28 compared to 60 - 65 % in Tenaghi Philippon, Figure 11). In the absence  
575 of intra-WX2 palaeoenvironmental information, correlation with the Tenaghi Philippon record indicates  
576 that this period of coarse-clastic delivery is coincident with reductions of 80 - 40 % in arboreal pollen at  
577 Tenaghi Philippon associated with the lowstand of the early MIS 28 stadial (Tzedakis et al., 2006, Figure  
578 11). Given the limited volume of sediment exposed as a result of base-level fall in narrow shelved active  
579 margins (Collier et al., 2000), an increase in sediment supply as a result of deforestation in the  
580 catchment is considered a possible trigger for the change from mudstone dominated WX1 to  
581 conglomeratic WX2 in MIS 28. A decrease in forest cover acts to increase erosion and sediment  
582 discharge due to more limited physical creep processes such as rainsplash and dry ravel to export  
583 material previously stored within the catchment (e.g., from freeze-thaw weathering and other  
584 glaciogenic processes) (Bosch & Hewlett, 1982; Leeder et al., 1998; Istanbuluoglu & Bras, 2005).

585 Much of WX3 was deposited during times when catchments contained limited forest cover and  
586 steppic/shrubland vegetation similar to many Mediterranean glacials (e.g. MIS 24, 26, 28 - Tzedakis et  
587 al., 2006; Joannin et al., 2007a, b, 2008; Wagner et al., 2019). However, the interpolation between  
588 magnetostratigraphic tie points suggests the onset of WX3 was during an interstadial, with moderately  
589 developed forest and an affinity towards temperate forested biomes (Figure 11, 13b). Given the highly  
590 erosive nature of Surface 3 in the Ilias fan delta, and the significant thickness (~25-30 m) of the overlying  
591 WX3 stratigraphy downdip in the WXFB, we interpret that Surface 3 likely represents the onset of a  
592 minor interstadial to stadial base-level fall, the deep-water expression of which separates



593 compensationally stacked WX2 and WX3. The presence of steppic elements in the middle part of WX3  
594 is synchronous with a reduction in affinity to forested biomes. A less forested landscape could have  
595 acted to increase lowland-derived 'soft' sediment yield to maintain sediment delivery during the likely  
596 limited lowstand/base-level fall and aid progradation of the reworked shoreline (*sensu* Leeder et al.,  
597 1998, Figure 13c). In addition, we interpret high levels of precipitation evidenced by well-maintained  
598 aquatic element taxa and reed grasses (*Phragmites* sp.) (Figure 10,11,13b).

599 WX4 is preceded by a substantial expansion in forest cover to the highest level seen in the G4  
600 stratigraphy (Figure 11, 13) and within the Tenaghi Philippon record (Tzedakis et al., 2006). The  
601 chronostratigraphic model suggests that this is synchronous with the global marine sea-level rise and  
602 warming related to the MIS 25 interglacial (Figure 11). During the warming phase of MIS 25, ~60%  
603 arboreal pollen values in the pollen sample at the base of WX4, and ~75% immediately prior to WX4  
604 document this expansion, which is demonstrated through the strongest affinities to broad-ranging and  
605 temperate/warm, malacophyll prone forest biomes (e.g. CENF, COOL, TEDE, CMIX, ENWD in Figure  
606 10). The strongest of these affinities tends towards CMIX, which may indicate a milder climate than the  
607 previous dominant GRAM and weak affinity to CMIX within the middle part of WX3. WX4 in the Ilias fan  
608 delta is recognised by a back-stepping relationship and fining upward indicative of delta retrogradation  
609 (Cullen et al., 2020). With WX4 chronostratigraphically constrained, we interpret the substantial  
610 magnitude and rate of this global marine transgression may have been mimicked by a more minor lake-  
611 level rise in Lake Corinth. Any lake level rise would likely have been amplified by ongoing subsidence,  
612 and we interpret this outpaced a synchronous reduction in sediment supply triggered by the expansion  
613 of catchment forest cover.

614 In the Ilias fan delta, WX4 is overlapped by prograding foresets of WX5 (Cullen et al., 2020). The  
615 chronostratigraphy and palynology of this study highlights this is coincident with a reduction in arboreal  
616 pollen during the latter part/peak of the MIS 25 interglacial highstand within WX5. Arboreal pollen  
617 percentages are reduced to 20% at the onset of WX5 and ~30% (20% of which is mesothermal) at the  
618 end of WX5. Biome affinities reflect this through showing stronger affinities to warm forest biomes  
619 (TEDE, CMIX, ENWD), an increase in arid shrubland affinities, and strong affinities to grasslands. This  
620 contrasts with the maintained, and substantial, forest cover (75-90% arboreal pollen) in the Tenaghi  
621 Philippon Record (Tzedakis et al., 2006), although a similar reduction appears within the transition from  
622 MIS 25 to MIS24 that is younger than the linear interpolation at G4 suggests. Pollen samples within  
623 WX5 show the development of steppic and halophilic elements but an absence of cold, or humidity  
624 demanding, taxa such as *Abies*. The dominance of *Spiniferities* spp. through WX5 and WX6 appears  
625 concomitant with proposed base-level changes (Section 5) but cannot be used alone as an indicator of  
626 marine connection or lake-level control (cf. Morzadec-Kerfoun, 2005). However, such dinoflagellate  
627 variability is consistent with the influx of nutrients from increased terrigenous supply (Mudie et al., 2010).  
628 The reduction in arboreal pollen percentage in the West Xylokaastro record is substantially larger (a  
629 reduction of 50-65%) than the higher frequency variability (75% +/- 10-15%) in the Tzedakis et al. (2006)  
630 record at this time and supports a genuine deforestation in the catchment rather than aliasing of higher-  
631 frequency variability. Therefore, we interpret that the reduction in forest cover (during a drier or semi-

632 arid period of an interglacial) permits sediment supply increase to drive progradation of the Ilias fan  
633 delta and supply of sediment to the deep-water (Figure 11).

634 WX6 in the Ilias fan delta is marked as a subtle increase in the conglomerate fraction, whilst in other  
635 portions of the delta bottomset WX6 is marked by channelised features (Section 2, 4.1, Rubi et al.,  
636 2018, Cullen et al., 2020). Distally, Surface 6 (base WX6) does not record an increased sediment supply  
637 or facies change from WX5 as it does more proximally. Surface 6, underlying WX6, occurs during the  
638 global cooling from MIS 25 to MIS24. In the G4 stratigraphy, arboreal pollen percentages increase at  
639 the proposed onset of WX6, which may have acted to coincidentally inhibit sediment supply from the  
640 catchment (Figure 11). This may explain why any coincident lake-level fall is not strongly represented  
641 in the stratigraphy. The sample at the top of WX6 shows a decrease in arboreal pollen percentages to  
642 assemblages more typical of Mediterranean glacials, dominated by grassland and steppe with limited  
643 development of forests that may have increased or maintained sediment supply to produce sandstone-  
644 dominated stratigraphy distally (Figure 10, 11). The G4 pollen record becomes sparse in WX7, which  
645 is more heterolithic and variable than underlying units (Cullen et al., 2020). However, the poor recovery  
646 of pollen in samples within WX7, and sparse spacing of samples due to the MTD at the basal part of  
647 WX7, means it is not possible to pose suitable interpretations on this part of the record.

648 Stratigraphic and palynological observations highlight that climatic and vegetation variability likely  
649 impacted sediment delivery to the deep-water in the WXFB. None of the studied section is deposited  
650 under fully marine conditions, and hence lake-level is a function of local climate and hydrology. Coarse-  
651 grained input is coincident with open vegetation typical of glacial conditions, or reduced forest cover in  
652 semi-arid interglacials. Severe supply reductions produce laterally extensive mudstone intervals during  
653 widespread increases in forestation, which may be coincident with high magnitude, rapid, 100-kyr paced  
654 warming events and global sea-level rises. Minor increases (those typical of interstadials or less severe,  
655 41-kyr paced interglacials) appear to have a more limited impact on supply to the deep-water, producing  
656 subtle facies changes, which are not readily distinguished from autogenic facies variability.

## 657 **7.2 Topographic and temporal complexity in Early-Middle Pleistocene rift-margin** 658 **catchments – implications and potential for further palynological investigations**

### 659 **7.2.1 Topographic complexity of short, steep drainage catchments**

660 Early-Mid Pleistocene palaeogeographies of the Olvios catchment indicate approximately 1600 m of  
661 elevation difference from the uppermost hinterland to the topsets of the Ilias fan delta over ~15-18 km  
662 horizontal distance (Gawthorpe et al., 2018). This elevation difference covers a wide variety of  
663 Mediterranean vegetation biomes within the transportable distance offshore for airborne pollen  
664 (Capraro et al., 2005, Suc & Popescu, 2005; Beaudouin et al., 2007; up to 100 km for Pinaceae  
665 Szczepanek et al., 2017). For example, the modern Gulf of Corinth catchments, analogous to warmer  
666 interglacials of the Middle Pleistocene, typically have semi-arid lowlands with grasslands (GRAM) and  
667 sclerophyllous ('scrub') vegetation typical of xeric shrublands (XSHB) and more forested but temperate-  
668 warm biomes (e.g. TEDE, WTDF, WTEF) with warm, scrub and grassland vegetation also present  
669 above the treeline (Papadopoulou et al., 2018, Marinova et al., 2018). This means the palynological  
670 assemblage is an aggregate of this spatial variability, which can inform detailed palaeoecology of the



671 syn-rift hinterland (McArthur et al., 2016c), rather than an isolated local palynological signature (e.g.  
672 from very broad lowlands unrepresentative of larger catchments). In syn-rift catchments, this  
673 configuration can substantially impact the calibre and timing of sediment supply. For example, altitudinal  
674 increases in catchment forest cover can inhibit erosion in the upper reaches, whereas lowland  
675 deforestation in lower reaches can promote reworking 'soft' sediment yield from soils (Leeder et al.,  
676 1998). It is for this reason that the biomization and biome affinities are not treated as a singular confident  
677 biome affinity, but that similarly-high affinities or changes in affinity may be representative of the entire  
678 variability of catchment vegetation (Marinova et al., 2018). Deep-water syn-rift localities are likely to  
679 offer opportunities to test or investigate the potential for whole-catchment variability further due to the  
680 large range of elevations over relatively short catchments, which are within the range to receive pollen  
681 as a palaeoclimatic archive. This is contrary to offshore passive margin studies, which may receive  
682 pollen largely from extensive (> 100s km) lowlands that may only represent a small part of the larger  
683 fluvial catchments controlling offshore sediment supply.

### 684 **7.2.2 Climatic variability and fluctuations of Lake Corinth in the Early-Middle Pleistocene**

685 The Gulf of Corinth's location within the eastern-central Mediterranean places it within a transition from  
686 Atlantic-influenced Mediterranean climates (hot, dry summers and cool, wet and stormy winters) to an  
687 Eastern Mediterranean/Levant semi-arid/arid climate. Global climatic variability through the Pleistocene  
688 can either enhance or dampen the influence of either of these climatic regimes through latitudinal shifts  
689 of the Atlantic Westerly jet stream (COHMAP Members, 1988; Harrison et al., 1992; Leeder et al., 1998;  
690 Collier et al., 2000). Particularly severe interglacials may alter the typical latitudinal range of the Atlantic  
691 Westerly jet stream allowing a departure from the typically temperate, forest-dominated interglacials  
692 (Leeder et al., 1998; Tzedakis et al., 2006; Joannin et al., 2007a, b; Francke et al., 2016; Sadori et al.,  
693 2016; Lacey et al., 2016; Wagner et al., 2019). This may explain fluctuations between wet and dry  
694 interglacials observed in comparative studies between the Eastern and Western Mediterranean,  
695 particularly through the Early-Middle Pleistocene transition (Capraro et al., 2005; Suc & Popescu, 2005).  
696 Furthermore, the impact of this upon local hydrology and catchment vegetation for lakes makes  
697 estimating lake-level for Lake Corinth during the Early-Pleistocene challenging. Whilst many  
698 Pleistocene lake-level records are observed to vary in-phase with global marine eustatic variability such  
699 as Lakes Tana and Tanganyika, East Africa (Gasse et al., 1989; Marshall et al., 2011), local hydrological  
700 and climatic variations can alter the evaporation to precipitation ratio for a given water body to produce  
701 lake-levels that operate out-of-phase with global marine changes (Leeder et al., 1998). For instance,  
702 lake-level falls during interglacials are documented in Late Pleistocene and Holocene Eastern  
703 Mediterranean and Levant lakes on account of more evaporative, arid conditions (Torfstein et al., 2013;  
704 Kiro et al., 2017). Conversely, Gulf of Corinth lake levels in the Late Pleistocene are suggested to be in  
705 phase with global marine variability through highstand marine incursions (Collier, 1990; Armijo et al.,  
706 1996; McNeil et al., 2019a). However, there is limited independent control on lake-level during the Early-  
707 Middle Pleistocene, when the Gulf of Corinth was largely isolated (Gawthorpe et al., 2018; McNeill et  
708 al., 2019a). We observe retrogradation of the Ilias fan delta during WX4 (Cullen et al., 2020), which the  
709 magnetostratigraphy of this study suggests developed synchronously with a substantial eustatic global  
710 sea-level rise outside Lake Corinth to the MIS25 interglacial highstand (Figure 11, Section 7). These

711 observations suggest that Lake Corinth levels may have operated (at least partly) in-phase with global  
712 marine variability at this time. An in-phase lake-level variability for the Gulf of Corinth is reasonable  
713 given that many of the catchments were affected by montane glaciations during the Pleistocene,  
714 particularly in the west of the rift (Pope et al., 2017; Hughes & Woodward, 2017, Leontaritis et al., 2020).  
715 Therefore, they would have been subject to increases in discharge from glacier melting, in the transition  
716 from glacials to interglacials, or reductions in discharge during glacier growth in glacials. The extent to  
717 which this was modified by higher overall precipitation during glacials (Leeder et al., 1998; Collier et al.,  
718 2000) is unclear, and may explain the minor absolute magnitude (10-15 m) of lake-level variability  
719 derived by Barrett et al. (2019) and de Gelder et al. (2019) for the Early Pleistocene Gulf of Corinth  
720 compared to time-equivalent global sea level variability (50 – 100 m).

### 721 **7.3 Early-Middle Pleistocene sediment supply variability in the West Xylokastro Fault** 722 **Block**

723 **Figure 11: West Xylokastro Landscape summary**

724 **Figure 12: Proposed conceptual model**

725 The typical climatic model for the Mediterranean is that highest sediment supply occurs during glacials,  
726 with limited supply to the basin during interglacials due to reduced precipitation and the trapping of  
727 sediment within the catchment because of well-developed forest cover (Leeder et al., 1998; Collier et  
728 al., 2000; Tzedakis et al., 2006). In the WXFB, WX2 and WX3, which the magnetostratigraphy suggests  
729 likely occurred during the glacial MIS 28, shows substantial coarse-grained sediment delivery to the  
730 deep-water depocenter of the West Xylokastro Fault Block (Figure 11, Figure 13, Figure 14B, C).  
731 Coarse sediment supply is also maintained in WX5 and WX6, which is proposed to be during the latter  
732 part of the MIS25 interglacial. Although sandstone-dominated, WX5 and WX6 are more heterolithic than  
733 WX2 and WX3. In contrast, sediment supply and resultant grain-sizes are substantially reduced within  
734 WX4, interpreted to have occurred during the warming and transgression to the MIS 25 interglacial  
735 (Figure 11, Figure 13, Figure 14A, D). Frequent winter storms during subsequent glacials may help to  
736 flush-out sediment stored in catchments, aided by steppe-like vegetation that is less effective at trapping  
737 sediment within the catchment (Leeder et al., 1998; Marston 2010; Schmid et al., 2018). Alternatively,  
738 an interglacial-driven supply model has been proposed to explain examples of larger sediment volumes  
739 deposited in interglacials (e.g. Watkins et al., 2018). Here *larger* winter storms occur during interglacials  
740 on account of elevated ocean and atmospheric temperatures and carry out significant geomorphic  
741 'work' in steep, short catchments, such as those surrounding the Gulf of Corinth (Trenberth et al., 2003;  
742 Berg et al., 2013; Bates et al., 2014; Watkins et al., 2018; Wagner et al., 2019). The MIS 25 interglacial  
743 in the Gulf of Corinth may represent an alternative form of Mediterranean interglacial (Figure 13e),  
744 proposed to have semi-arid lowland vegetation and partly forested mountains during its peak, contrary  
745 to typical widespread forest cover of most Pleistocene interglacials (Tzedakis et al., 2006; Joannin et  
746 al., 2007a,b; Figure 13d, 14a,d,e). In the G4 borehole record, well-developed forest is only seen during  
747 the preceding warming phase. Samples within MIS25 reveal substantially reduced Pinaceae pollen  
748 counts. The reduction in forest cover during the latter stages of the interglacial, coupled with large winter

749 storms may well allow sediment flux to deep-water environments sooner than predicted by previous  
750 models (cf. Leeder et al., 1998).

751 The peak of the atypical MIS25 Mediterranean interglacial permitted enhanced sediment supply from  
752 catchments. High run-off is evidenced by the prevalence of nutrient-rich freshwater indicators like  
753 *Botryococcus* and *Spiniferites* spp. in this part of the stratigraphy (Mudie et al., 2010). Large storms, in  
754 cool, rather than very cold, wet winters may have eroded substantial volumes of sediment on dominantly  
755 grassland and xeric shrubland landscapes. Dry, hot summers are then interpreted to produce limited  
756 sediment delivery to the deep-water leading to highly seasonal sediment flux. This seasonal sediment  
757 delivery may explain the more heterolithic, but still coarse-grained, character of interglacial/highstand  
758 units like WX5. This is similar to sediment delivery in the modern Gulf of Corinth, demonstrated by the  
759 frequency of subaqueous cable breaks basinward of river mouths concentrated during winter months  
760 following large storms (Heezen et al., 1966; Papadopoulos, 2003). Interglacials within the Quaternary  
761 vary in severity and associated with entirely different weather patterns (e.g. jet-stream positions,  
762 Harrison et al., 1992) producing variable climate conditions for a given interglacial or glacial. It is  
763 therefore recommended that interglacials, whilst warmer than their preceding or following glacial, are  
764 not by default treated as drier overall and should include the possibility of enhanced or reduced  
765 seasonality compared to other glacials or interglacials (e.g. Collier et al., 2000).

766 Glacial periods of the Pleistocene in central Greece were often accompanied by montane glaciations  
767 (Smith et al., 1997; Hughes et al., 2006, 2007; Bathrellos et al., 2017; Hughes & Woodward, 2017;  
768 Leontaritis et al., 2020). Whilst most of the Olvios drainage is unlikely to have suffered severe or full  
769 glaciation given its elevation below the equilibrium line for Pleistocene glaciations, extensive permafrost  
770 was likely, especially in its upper reaches (Hughes & Woodward, 2017; Leontaritis et al., 2020). In  
771 addition to colder temperatures, permafrost can further inhibit widespread forest growth during glacials  
772 which may promote increases in sediment transport out of the catchment (Woodward et al., 1992;  
773 Hughes et al., 2007). However, any deforestation competes with the ability for longer-term ice or  
774 permafrost coverage in the upper reaches of catchments to diminish supply by reducing the effective  
775 size of the catchment or restricting erodibility compared to an unglaciated catchment (Armitage et al.,  
776 2011; Romans et al., 2016; Watkins et al., 2018). The extent to which this impacts a catchment may be  
777 minor, with seasonal freeze-thaw weathering identified as the primary mechanism through which  
778 enhanced erosion during Mediterranean glacials occurs (Italian Apennines – Tucker et al., 2011). The  
779 sediment produced through this can be flushed-out of the catchment during minor warming or wet  
780 episodes in stadials, or the end of the glacial (Figure 13a, Figure 14b,c: Hughes et al., 2007; Armitage  
781 et al., 2011; Tucker et al., 2011; Strachan et al., 2013; Cordier et al., 2017; Cao et al., 2018).

782 Ultimately, interglacially-driven supply relies on large, basin-drainage changes being recorded as a  
783 'step-change' in stratigraphy (Armitage et al., 2011, Watkins et al., 2018). In contrast, glacially-driven  
784 supply relies on the consistency and averaging effect of frequent storms, and absence of forest cover  
785 common to Mediterranean glacials (Harrison et al., 1992, Collier et al., 2000). The climatic transition  
786 *between* glacials and interglacials has been poorly documented in deep-water syn-rift systems, with a  
787 focus on prevailing interglacial or glacial conditions. However, the nature of the transitions between

788 interglacials and glacials are seen to be equally as important in interrupting sediment delivery from  
789 terrestrial catchments as lowstand/glacial or highstand/interglacial climate/vegetation conditions  
790 themselves (Armitage et al., 2013). We interpret that both deforestation-aided glacial supply and highly  
791 seasonal interglacials increases in sediment supply were active in the Early-Mid Pleistocene WXFB.

#### 792 **7.4 Palaeoenvironmental controls on deep-water syn-rift sedimentation**

793 The WXFB stratigraphy highlights that major climatic changes during global marine transgressions form  
794 the principal mechanism for inhibiting otherwise sustained sediment supply to the deep-water in rift  
795 settings. However, to expect all systems to respond similarly may be unrealistic given well-documented  
796 examples of the transition to interglacials providing increased sediment supply through deglaciation of  
797 drainage catchments (e.g. Mississippi Fan Delta during Holocene transgression (Covault & Graham,  
798 2010) and Armorican turbidite systems during the Last Glacial (20-15ka) warming (Toucanne et al.,  
799 2012)). The manner in which a landscape and basin responds to changes from glacials to interglacials  
800 will be specific to a given landscape and rely on local interaction and feedbacks between drainage  
801 physiography, the rate and nature of climatic and vegetation variability, oceanographic changes and  
802 shoreline processes (Hay et al., 2014; Dixon et al., 2012; Armitage et al., 2013; Bernhardt et al., 2016,  
803 2017; Beckers et al., 2016; Romans et al., 2016; Rovere et al., 2016; Horsch & Fourniotis, 2018;  
804 Watkins et al., 2018; Pechlivanidou et al., 2018; Cosgrove et al. 2018).

805 In the WXFB, it is only the largest climatic changes that produce widespread stratigraphic changes.  
806 Ultimately, this results in intra-formational and laterally extensive mudstone-dominated successions  
807 being rare amongst sustained coarse-grained supply, but where present are typically triggered by rapid  
808 and extensive forestation related to warming during the transition from glacials to severe interglacials  
809 (Figure 13, 14). The extreme narrowness or absence of shelves and limited sediment storage in  
810 terrestrial settings along active rift margins permits enhanced sensitivity of the deep-water realm to  
811 major cessations and triggers of sediment supply in the catchments from climatic changes (Burgess &  
812 Hovius, 1998; Carvajal & Steel, 2006; Covault & Graham, 2010; Strachan et al., 2013; Romans et al.,  
813 2016; Harris et al., 2018; Watkins et al., 2018; Zhang et al., 2019a, b). Counterintuitively, small  
814 magnitude or high frequency ( $10^3$  yrs) supply fluctuations may not be stratigraphically represented as  
815 reduced sedimentation, or changes in sedimentary parameters, because supply is readily maintained  
816 to the deep-water across narrow shelves within the response timescale of the landscape (Romans et  
817 al., 2016; Jobe et al., 2017; Hajek & Straub, 2017; Tofelde et al., 2021). More subtle changes may  
818 therefore be non-resolvable from bathymetrically controlled spatial patterns in deposition or autogenic  
819 variability. In the WXFB, where sediment supply is derived from the footwall catchment, high sediment  
820 supply across a narrow Gilbert fan delta topset (1.5 km long and ~3.5 km radius, Cullen et al., 2020) is  
821 interpreted to prevent the preservation of environmental signals of minor changes in climate or lake-  
822 level in the stratigraphy as changes of lithofacies. However, the lower subsidence rates and shallower  
823 water depths typical of a hanging wall dip-slope system, permit larger alluvial topsets or the  
824 development of low angle, subaqueous shelves (Gawthorpe et al., 1994; Collier & Gawthorpe, 1995,  
825 Henstra et al., 2016, cf. Figure 14). This increases the potential for sediment storage and signal-  
826 shredding (Jerolmack & Paola, 2010) along the transport path prior to the deep-water realm, which may

827 act to enhance the impact of high-frequency, low-magnitude, minor sediment flux reductions contrary  
828 to the maintained supply observed in the West Xylokastro.

## 829 **8 Conclusion**

830 Deep-water syn-rift sediment delivery relies on the complicated interplay of climate, vegetation,  
831 drainage arrangement, shelf physiography, and structural evolution. 'Classical' sequence stratigraphic  
832 models, which predict delivery restricted to lowstands or base-level falls, do not sufficiently represent  
833 the variability in rift basin-fills. Typically, active rifts are dominated by narrow or absent shelves, and as  
834 such their deep-water environments are sensitive to onshore changes in sediment flux, which may be  
835 linked to climatic variability. Vegetation changes coherent with global, orbital-forced climatic variability  
836 in the Early-Mid Pleistocene favour increased sediment delivery during glacial periods, and during semi-  
837 arid highstands/interglacial periods when high sediment supply is aided by large interglacial winter  
838 storms and a reduction in lowland forest cover. Coherence between vegetation and climate is persistent  
839 during the obliquity-controlled Early Pleistocene. However, vegetation fluctuations occur at higher  
840 temporal orders and magnitudes following the Early-Mid Pleistocene transition to eccentricity-paced  
841 glacioeustasy. In the West Xylokastro Fault Block, deep-water syn-rift coarse-grained sediment delivery  
842 is only hindered during large magnitude warming events related to larger, eccentricity-paced  
843 transgressions, which promotes widespread forest cover that reduces catchment sediment yield. Where  
844 possible, different severities of glacial or interglacial episodes should be included in palaeoclimate  
845 models rather than binary, dry-interglacial vs. wet-glacial models. The role of highly seasonal or wet  
846 interglacials may be important for triggering sediment release from onshore catchments into the deep-  
847 water realm. The study highlights the variability of the stratigraphic signature of such signals, which can  
848 be interpreted using palynological data to discern palaeoenvironmental change despite the distal  
849 setting, and the typical coarse grain-size of the deep-water deposits in such systems. The study  
850 highlights the value of integrating chronostratigraphic interpretation with palynological and broader  
851 stratigraphic relationships to help discern the evolution of deep-water syn-rift systems, and provides  
852 new conceptual models for climatic control on deep-water sediment delivery.

## 853 **9 Acknowledgements**

854 This publication forms part of the first author's PhD project which was funded by the Syn-Rift Systems  
855 (PETROMAKS 2) project funded by the Research Council of Norway (Project number 255229/E30) and  
856 industry partners Aker BP, ConocoPhillips, DNO, Equinor, Tullow Oil and Neptune Energy and by the  
857 University of Leeds. TC and RLG also acknowledge VISTA visitor and professorship funding and  
858 Equinor for core storage and viewing facilities in Bergen. Natasha Barlow is thanked for access to a  
859 Leica DM2500 microscope. Fanis Chatoupis of HydroGEO, and the chair of the council of Kalithea are  
860 thanked for facilitating drilling of the borehole in Greece. Al Fraser and Bill McCaffrey are thanked for  
861 discussions on an earlier version of this manuscript. Pollen plots were generated using C2  
862 (<https://www.staff.ncl.ac.uk/stephen.juggins/software/C2Home.htm>). Palynological sample preparation  
863 by Malcolm Jones of Palynological Laboratory Services Ltd, Anglesey, Wales.

## 864 **10 Figure Captions**

865 **Figure 1:** Geological location map for the study area, the West Xylokaastro fault block, modified from  
866 Cullen et al. (2020). Coordinates are UTM (in Metres) for zone 34N. MT = Marine Terrace, WXF = WXF,  
867 VRY = Vrysoulous Fault. Cross section (Figure 3) localities are provided in dark blue dots, with other  
868 figures in this paper referenced by white outlook points. Stratigraphic key for the map shows colours  
869 and relative ages of mapped units. TKF = Trikala Fault, SF=Sythas Fault, AF=Amphithea Fault, KF =  
870 Kyllini Fault, MF = Mavro Fault, WXF = WXF, LF = Lykoporiá Fault, K = Kyllini, M = Mavro, E/I=  
871 Evrostini/Ilias, PM = Pyrgos Member, LS = Lykoporiá Slide. WTS – Western Transverse system, CTS  
872 – Central Transverse system. B) Location of the study area within the Gulf of Corinth, Central Greece  
873 highlighting the distribution of Pre-Rift and Syn-Rift stratigraphy. All mapping constructed and modified  
874 from Gawthorpe et al. 2017, compiled from Ford et al., 2013, Ford et al., 2016, Nixon et al., 2016,  
875 Skourtsos unpb. and author's own mapping. Red box indicates the locale focused on in this paper.

876 **Figure 2:** Summary stratigraphic correlation modified from Cullen et al. (2020) highlighting the position  
877 of the G4 borehole and outcrop samples ~ 7km downdip of the base of the Ilias delta and the supporting  
878 outcrop palaeomagnetic samples (black squares) outboard and within the G4 stratigraphy.

879 **Figure 3:** A) The Skoupéika digital outcrop model with the projection and measurement of unit  
880 thicknesses in to the G4 borehole (Figure 5-4). Bracketed numbers indicate minimum thickness at digital  
881 log locations where a unit is constrained by the base or top of the exposure. \* and \*\* indicate thicknesses  
882 which are projected from downdip digital logs 150 m away in the Skoupéika North Face. B) Outcrop  
883 photograph of the face in A, highlighting stratigraphic architectures and exposure of G4 stratigraphy  
884 nearby. C) Summary of the stratigraphic position of samples within, and outboard of the well stratigraphy  
885 along with unit projections. The channel body and MTD are considered within WX7.

886 **Figure 4:** Correlation panel for the Skoupéika East outcrop into the G4 borehole with relative  
887 proportions of coarse-grained to fine-grained stratigraphy expressed as net:gross. Two main coarse-  
888 grained stratigraphic units (WX3 and WX5) are separated by mudstone rich WX4. MT and WX7  
889 thicknesses are extrapolated from a digital log out of section by ~120 m downdip in line with 4a. The  
890 Skoupéika structure is complicated by an intra-basinal fault tip (probably related to Minor Fault 1), which  
891 generated a small anticline in the southern part of the cliffs and restricted the lateral extent of WX2. This  
892 produces the thinning relationships seen in WX3, WX4 and WX5, which show a northward and  
893 southward thinning from the central area (Log 4) where they are thickest.

894 **Figure 5:** Palaeomagnetic ties of four reversals identified within the sampled stratigraphy to generate  
895 6 magnetozones (MAG0-MAG5). Buffers in the placement of these reversals within the stratigraphy are  
896 shown as error bars in the sample locations on the right. Influence of Likoporia Fault (LF) determined  
897 from literature chronostratigraphic models and stratigraphic evidence in this study.

898 **Figure 6:** Summary chart (A) for the four possible alternative palaeomagnetic interpretations for the  
899 West Xylokaastro RDF stratigraphy in this thesis. B) Sediment accumulation rates for magnetozones  
900 (MAG0-5) for the four possible scenarios. Red text indicates sediment accumulation rates (m/kyr) which  
901 are far outside previously documented ranges for similar settings or are of extreme variability. C)  
902 Summary of interpretation choice based on agreement with well-established regional  
903 palaeogeographies, required uplift rates, sedimentation rates, and the ability for the palaeomagnetic  
904 survey in this study to detect the required variations. \* - Sedimentation rates for these magnetozones  
905 are less constrained than MAG1 – MAG4 due to no 'bounding' reversal at the base and top of  
906 stratigraphy and so are estimated as maximums, to the nearest adjacent reversal or extrapolation of  
907 the maximum preserved thickness. Geomagnetic Instability Time Scale (GITS) palaeomagnetic record  
908 from Singer et al. (2014). † duration for Santa Rosa taken from Yang et al. (2004). § duration for  
909 Punaruu from Channell (2017). ¶ minor Bruhnes excursion durations deemed as ~1kyr from Singer  
910 (2014), likely not truly detectable in this survey.

911 **Figure 7:** A) Environmental importance of relative percentages on ternary palynology plots of  
912 percentages of TP (Terrestrial Palynomorphs), NTP (Non-Terrestrial or 'marine' Palynomorphs) and  
913 AOM (Amorphous Organic Matter). Modified after Zobaa et al. (2015) and Tyson (1996). B1) Full scaled  
914 ternary plot for G4 palynology samples highlighting strong freshwater influence in all samples. B2) Blow  
915 out of upper 20% triangle highlighting minor deviations to weak marine (or saline) influences (<5%).

916 **Figure 8:** Summary stratigraphic plot of raw count data for sedimentary organic matter (excluding  
917 pollen, spores and dinoflagellates). X-axes are absolute numbers of particles, with numbers provided  
918 where the x-axis is exceeded.

919 **Figure 9:** Stratigraphic summary for dinoflagellate cysts presented as concentrations (cysts/g). Small  
920 values/low occurrences are labelled along with a 'Dino Sum' (total number of dinoflagellate cysts in  
921 each sample) curve.

922 **Figure 10: (2 pages)** A) Detailed concentration (thousands of grains per gram) diagram of all pollen  
923 taxa identified, showing the constituent taxa of groupings. Pollen sum (total counts) are also provided.  
924 B) Upper: Pollen groupings plot in percentages along with total pollen sum and Lower: Biomization  
925 summary highlighting the G4 data with an environmental key and conceptual after Marinova et al. (2018)  
926 highlighting the general temperature and precipitation conditions the biomes exist under. Boxes  
927 surrounding points on the biome affinity plot highlight the 5 strongest affinities for a given sample, where  
928 more than 5 are highlighted this reflects where biomes have equal affinities. The modified Marinova et  
929 al. (2018) conceptual model is reproduced with permission from John Wiley & Sons (License No.  
930 5072700384261).

931 **Figure 11:** A) Summary of palaeomagnetically tied intervals of the G4 palynological record. B) Age  
932 model for G4 stratigraphy using linear time-depth relationship/sedimentation rate within magnetozones.  
933 Palaeomagnetic tie-points from the G4 stratigraphy are highlighted with triangles where black  
934 represents normal polarity, and reversed represented by white. A subset of biome affinities are also  
935 shown; DESE - Desert, XHSB - Xerophytic Shrub, GRAM - Graminoids with Forbs, DBWB - Deciduous  
936 broadleaf woodland, WTEF - Warm-temperate evergreen needleleaf and sclerophyll broadleaf forest,  
937 TEDE, Temperate deciduous malcophyll broadleaf forest and CMIX - Cool mixed evergreen needleleaf  
938 and deciduous broadleaf forest. Onshore bed thicknesses are not representative of actual bed  
939 thicknesses. Equivalent offshore stratigraphy is from IODP Hole M0078 after McNeil et al. 2019f where  
940 (N.B Colour schemes are altered from McNeil et al., 2019a-f for comparison here). Tenaghi Philippon  
941 Arboreal Pollen Percentage is retrieved from the updated age model of Wagner et al. (2018), Lake  
942 Ohrid Arboreal Pollen (minus Pinus) record from Sadori et al. (2016). MPT – Mid-Pleistocene Transition.

943 **Figure 12:** Schematic chronostratigraphic summary diagram for the central part of the for West  
944 Xylokastro to central Corinth rift region for the Early-Mid Pleistocene. WXF – West Xylokastro Fault,  
945 MF1-7 – Minor Fault, LF – Likoporia Fault, AnF – East Antikyra Fault, WAnF – West Antikyra Fault,  
946 EXF – East Xylokastro Fault, KF – Kiato Fault, DF – Derveni Fault. G4 – Syn-Rift Systems borehole,  
947 M0079-M0078, IODP Exp 381. Boreholes. The yellow dashed line approximates the location of the  
948 section, which condenses considerable lateral variability.

949 **Figure 13:** Conceptual cartoons highlighting vegetation and climatic variability and the impact of this  
950 on the timing and calibre of sediment delivered to the deep-water realm. WXF - West Xylokastro Fault,  
951 LF - Lykoporiá Fault, DF - Derveni Fault, CUBs - Convex Up Bodies (Cullen et al., 2020).

952 **Figure 14:** Conceptual cartoon models for sediment supply variability with Pleistocene climatic and  
953 vegetation changes in Mediterranean catchments.

954

955 **11 References**

- 956 Allen, P.A. 2008. Time scales of tectonic landscapes and their sediment routing systems In: K. Gallagher, S. .  
957 Jones and J. Wainwright, eds. *Landscape Evolution: Denudation, Climate and Tectonics Over Different Time and*  
958 *Space Scales. Geological Society of London Special Publication No. 296.* Geological Society London, pp.7–28.
- 959 Armijo, R., Meyer, B., King, G.C.P., Rigo, A. and Papanastassiou, D. 1996. Quaternary evolution of the Corinth Rift  
960 and its implications for the Late Cenozoic evolution of the Aegean. *Geophys. J. Int.* 126, pp.11–53.
- 961 Armitage, J.J., Duller, R.A., Whittaker, A.C. and Allen, P.A. 2011. Transformation of tectonic and climatic signals  
962 from source to sedimentary archive. *Nature Geoscience.* 4, pp.231–235.
- 963 Armitage, J.J., Dunkley Jones, T., Duller, R.A., Whittaker, A.C. and Allen, P.A. 2013. Temporal buffering of climate-  
964 driven sediment flux cycles by transient catchment response. *Earth and Planetary Science Letters.* 369–370,  
965 pp.200–210.
- 966 Armitage, J.J., Whittaker, A.C., Zakari, M. and Campforts, B. 2018. Numerical modelling of landscape and sediment  
967 flux response to precipitation rate change. *Earth Surface Dynamics.* 6, pp. 77-99.
- 968 Backert, N., Ford, M., Malartre, F., Architecture and sedimentology of the Kerinitis Gilbert-type fan delta, Corinth  
969 Rift, Greece. *Sedimentology.* 57. pp.543-586.
- 970 Barrett, B.J., Hodgson, D.M., Collier, R.E.L., Dorrell, R. 2018. Novel 3D sequence stratigraphic numerical model  
971 for syn-rift basins: Analysing architectural responses to eustasy, sedimentation and tectonics. *Marine and*  
972 *Petroleum Geology.* 92, pp. 270-284.
- 973 Barrett, B.J., Collier, R.E.L., Hodgson, D.M., Gawthorpe, R.L., Dorrell, R. and Cullen, T.M. 2019. Quantifying  
974 faulting and base level controls on syn-rift sedimentation using stratigraphic architectures of coeval, adjacent Early-  
975 Middle Pleistocene fan deltas in Lake Corinth, Greece. *Basin Research.* pp.1–26.
- 976 Bates, S.L., Siddall, M. and Waelbroeck, C. 2014. Hydrographic variations in deep ocean temperature over the  
977 mid-Pleistocene transition. *Quaternary Science Reviews.* 88, pp.147–158.
- 978 Bathrellos, G.D., Skilodimou, H.D., Maroukian, H., Gaki-Papanastassiou, K., Kouli, K., Tsourou, T. and Tsaparas,  
979 N. 2017. Pleistocene glacial and lacustrine activity in the southern part of Mount Olympus (central Greece). *Area.*  
980 49, pp.137–147.
- 981 Beaudouin, C., Suc, JP, Escarguel, G., Arnaud, M. and Charmasson, S. 2007 The significance of pollen signal in  
982 present-day marine terrigenous sediments: The example of the Gulf of Lions (western Mediterranean Sea),  
983 *Geobios,* 40 (2), pp. 159-172
- 984 Beckers, A., Hubert-Ferrari, A., Beck, C., Bodeux, S., Tripsanas, E., Sakellariou, D. and De Batist, M. 2015. Active  
985 faulting at the western tip of the Gulf of Corinth, Greece, from high-resolution seismic data. *Marine Geology.* 360,  
986 pp.55–69.
- 987 Beckers, A., Beck, C., Hubert-Ferrari, A., Tripsanas, E., Crouzet, C., Sakellariou, D., Papatheodorou, G. and De  
988 Batist, M. 2016. Influence of bottom currents on the sedimentary processes at the western tip of the Gulf of Corinth,  
989 Greece. *Marine Geology.* 378, pp.312–332.
- 990 Bell, R.E., McNeill, L.C., Bull, J.M., Henstock, T.J., Collier, R.E.L. and Leeder, M.R. 2009. Fault architecture, basin  
991 structure and evolution of the Gulf of Corinth rift, central Greece. *Basin Research.* 21, pp.824–855.



- 992 Benninghoff, W.S., 1962. Calculation of pollen and spores density in sediments by addition of exotic pollen in  
993 known quantities. *Pollen et Spores* ,6, 332–333
- 994 Berg, P., Moseley, C. and Haerter, J.O. 2013. Strong increase in convective precipitation in response to higher  
995 temperatures. *Nature Geoscience*. 6(3), pp.181–185.
- 996 Bernhardt, A., Hebbeln, D., Regenber, M., Lückge, A. and Strecker, M.R. 2016. Shelfal sediment transport by an  
997 undercurrent forces turbidity current activity during high sea level along the Chile continental margin. *Geology*. 44,  
998 pp.295–298.
- 999 Bernhardt, A., Schwanghar, W., Hebbeln, D., Stuut, J.-B. W., and Strecker, M.R. 2017. Immediate propagation of  
1000 deglacial environmental change to deep-marine turbidite systems along the Chile convergent margin. *Earth  
1001 Planetary Science Letters*. 473, pp. 190-204.
- 1002 Beug, H.-J. 2015. Leitfaden der Pollenbestimmung für Mitteleuropa und angrenzende Gebiete 2nd ed. München:  
1003 Verlag Dr. Friedrich Pfeil.
- 1004 Blum, M.D. and Hattier-Womack, J. 2009. Climate Change, Sea-level change, and fluvial sediment supply to  
1005 deepwater depositional systems In: B. Kneller, O. Martinsen and B. McCaffrey, eds. *External Controls on Deep-  
1006 Water Depositional Systems SEPM Special Publication No.92*. Tulsa, OK: SEPM (Society for Sedimentary  
1007 Geology), pp.15–39.
- 1008 Bogaart, P.W., Van Balen, R.T., Vadenberge, J., Kasse, C. 2002 Process-based modelling of the climatic forcing  
1009 of fluvial sediment flux: some examples and a discussion of optimal model complexity in Jones, S.L., Frostick, L.E.,  
1010 (eds.) *Sediment Flux to Basins: Causes, Controls and Consequences* Geological Society Special Publication 191,  
1011 pp187-198.
- 1012 Bourget, J., Zaragosi, S., Mulder, T., Schneider, J.L., Garlan, T., Van Toer, A., Mas, V. and Ellouz-Zimmermann,  
1013 N. 2010a. Hyperpycnal-fed turbidite lobe architecture and recent sedimentary processes: A case study from the Al  
1014 Batha turbidite system, Oman margin. *Sedimentary Geology*. 229(3), pp.144–159.
- 1015 Bosch, J., Hewlett, J. 1982. A review of catchment experiments to determine the effect of vegetation changes on  
1016 water yield and evapotranspiration. *Journal of Hydrology*. 55(1-4). pp. 3-23.
- 1017 Bourget, J., Zaragosi, S., Ellouz-Zimmermann, S., Ducassou, E., Prins, M.A., Garlan, T., Lanfumey, V., Schneider,  
1018 J.-L., Rouillard, P. and Giraudeau, J. 2010b. Highstand vs. lowstand turbidite system growth in the Makran active  
1019 margin: Imprints of high-frequency external controls on sediment delivery mechanisms to deep water systems.  
1020 *Marine Geology*. 274, pp.187–208.
- 1021 Buckley, S.J., Ringdal, K., Naumann, N., Dolva, B., Kurz, T.H., Howell, J.A., Dewez, T.J 2019. LIME: Software for  
1022 3-D visualization, interpretation, and communication of virtual geoscience models. *Geosphere*. 15 (1), pp. 222-235.
- 1023 Burgess, P.M. and Hovius, N. 1998. Rates of delta progradation during highstands: consequences for timing of  
1024 deposition in deep-marine systems. *Journal of the Geological Society*. 155, pp.217–222.
- 1025 Cande, S. and Kent, D.. 1995. Revised calibration of the geomagnetic polarity timescale for the late Cretaceous  
1026 and Cenozoic. *Journal of Geophysical Research*. 100, pp.6093–6095.
- 1027 Cao, Y., Wang, Y., Gluyas, J.G., Liu, Huimin, Liu, Haining and Song, M. 2018. Depositional model for lacustrine  
1028 nearshore subaqueous fans in a rift basin : The Eocene Shahejie Formation , Dongying Sag , Bohai Bay Basin ,  
1029 China. *Sedimentology*. 65, pp.2117–2148.

- 1030 Capraro, L., Asioli, A., Backman, J., Bertoldi, R., Channell, J.E.T., Massari, F. and Rio, D. 2005. Climatic patterns  
 1031 revealed by pollen and oxygen isotope records across the Matuyama-Brunhes boundary in the central  
 1032 Mediterranean (southern Italy) In: M. Head and P. Gibbard, eds. *Early-Middle Pleistocene Transitions: The Land-  
 1033 Ocean Evidence. Geological Society London Special Publication No. 247* Geological Society London, pp.159–182.
- 1034 Carvajal, C.R. and Steel, R.J. 2006. Thick turbidite successions from supply-dominated shelves during sea-level  
 1035 highstand. *Geology*. 34, pp.665–668.
- 1036 Castellort, S., Honegger, L., Adatte, T., Clark, J.D., Puigdefàbregas, C., Spangenberg, J.E., Dykstra, M.L., Fildani,  
 1037 A. Detecting eustatic and tectonic signals with carbon isotopes in deep-marine strata, Eocene Ainsa Basin, Spanish  
 1038 Pyrenees. 2017. *Geology*. 45 (8). pp. 707-710.
- 1039 Causse, C., Moretti, I., Eschard, R. and Micarelli, L. 2004. Kinematics of the Corinth Gulf inferred from calcite dating  
 1040 and syntectonic sedimentary characteristics. *Comptes Rendus Geoscience*. 336(4–5), pp.281–290.
- 1041 Channell, J.E.T 2017. Magnetic excursions in the late Matuyama Chron (Olduvai to Matuyama-Brunhes boundary)  
 1042 from North Atlantic IODP sites. *Journal of Geophysical Research: Solid Earth*, 122, pp.773-789.
- 1043 Cheng, L., Zhang, L., Chiew, F.H.S., Canadell, J.G., Zhao, F., Wang, Y.P., Hu, X. and Lin, K. 2017. Quantifying  
 1044 the impacts of vegetation changes on catchment storage-discharge dynamics using paired-catchment data. *Water  
 1045 Resources Research*. 53(7), pp.5963–5979.
- 1046 Chester, P.I. and Raine, J.I. 2001. Pollen and spore keys for Quaternary deposits in the northern Pindos Mountains,  
 1047 Greece. *Grana*. 40, pp.299–387.
- 1048 Cohen K.M. & Gibbard, P. 2016 Global chronostratigraphical correlation table for the last 2.7 million years. V.2016a  
 1049 Subcommittee on Quaternary Stratigraphy (International Commission on Stratigraphy), Cambridge, England.
- 1050 COHMAP MEMBERS 1988. Climatic changes of the last 18,000 years:observ and model situations. *Science*. 241,  
 1051 pp.1043–1052.
- 1052 Collier, R.E.L. 1990. Eustatic and tectonic controls upon Quaternary coastal sedimentation in the Corinth Basin,  
 1053 Greece. *Journal of the Geological Society*. 147, pp.301–314.
- 1054 Collier, R.E.L. and Dart, C.J. 1991. Neogene to Quaternary rifting, sedimentation and uplift in the Corinth  
 1055 Basin, Greece. *Journal of the Geological Society*. 148, pp.1049–1065.
- 1056 Collier, R.E.L. and Gawthorpe, R.L. 1995. Neotectonics, drainage and sedimentation in central Greece: insights  
 1057 into coastal reservoir geometries in syn-rift sequences In: J. Lambiase, ed. *Hydrocarbon Habitat in Rift Basins,  
 1058 Geological Society Special Publication No. 80*. Geological Society of London, pp.165–181.
- 1059 Collier, R.E.L., Leeder, M.R., Trout, M., Ferentinos, G., Lyberis, E. and Papatheodorou, G. 2000. High sediment  
 1060 yields and cool, wet winters: Test of last glacial paleoclimates in the northern Mediterranean. *Geology*. 28, pp.999–  
 1061 1002.
- 1062 Cordier, S., Adamson, K., Delmas, M., Calvet, M. and Harmand, D. 2017. Of ice and water: Quaternary fluvial  
 1063 response to glacial forcing. *Quaternary Science Reviews*. 166, pp.57–73.
- 1064 Cosgrove, G.I.E., Hodgson, D.M., Poyatos-Moré, M., Mountney, N.P. and McCaffrey, W.D. 2018. Filter Or  
 1065 Conveyor? Establishing Relationships Between Clinofold Rollover Trajectory, Sedimentary Process Regime, and  
 1066 Grain Character Within Intraself Clinofolds, Offshore New Jersey, U.S.A. *Journal of Sedimentary Research*.  
 1067 88(8), pp.917–941.

- 1068 Covault, J.A. and Graham, S.A. 2010. Submarine fans at all sea-level stands: Tectono-morphologic and climatic  
1069 controls on terrigenous sediment delivery to the deep sea. *Geology*. 38, pp.939–942.
- 1070 Cullen, T.M, Collier, R.E.LI, Gawthorpe R.L, Hodgson, D.M and Barrett, B.J. 2020. Axial and transverse deep-water  
1071 sediment supply to syn-rift fault terraces: insights from the West Xylokastro Fault Block, Gulf of Corinth, Greece,  
1072 *Basin Research*, 32, pp. 1105-1139
- 1073 de Gelder, G., Fernández-blanco, D., Melnick, D., Duclaux, G., Bell, R.E., Jara-muñoz, J., Armijo, R. and Lacassin,  
1074 R. 2019. Lithospheric flexure and rheology determined by climate cycle markers in the Corinth Rift. *Scientific*  
1075 *Reports*. 9 pp.1–12.
- 1076 Dixon, J.F, Steel, R.J, Olariu, C, 2012. Shelf-Edge Delta Regime as a Predictor of Deep-Water Deposition. *Journal*  
1077 *of Sedimentary Research*, 82, pp. 681-687
- 1078 Djamali, M and Cilleros, K. 2020. Statistically significant minimum pollen count in Quaternary pollen analysis; the  
1079 case of pollen-rich lake sediments. *Review of Palaeobotany and Palynology*. 275. 104156.  
1080 <https://doi.org/10.1016/j.revpalbo.2019.104156>.
- 1081 Doutsos, T. and Poulimenos, G. 1992. Geometry and kinematics of active faults and their seismotectonic  
1082 significance in the western Corinth-Patras rift (Greece). *Journal of Structural Geology*. 14, pp.689–699.
- 1083 Fatourou, E., Kafetzidou, A., Panagiotopoulos,K., Marret, F., Papadopoulous,S., Kouli, K. and the IODP Expedition  
1084 381 Science Team. 2021. Quaternary Environmental Changes in the Corinth Rift Area: the IODP 381 Palynological  
1085 Record. *EGU General Assembly 2021, EGU21-11360*
- 1086 Fernández-Blanco D., de Gelder G., Lacassin R., and Armijo, R. 2019. A new crustal fault formed the modern  
1087 Corinth Rift, *Earth-Science Reviews*, 19
- 1088 Fernández-Blanco D., de Gelder G., Lacassin R., and Armijo, R. 2020. Geometry of flexural uplift by continental  
1089 rifting in Corinth, Greece. *Tectonics*, 39, <https://doi.org/10.1029/2019TC005685>
- 1090 Flotté, N., Plagnes, V., Sorel, D. and Benedicto, A. 2001. Attempt to date Pleistocene normal faults of the Corinth-  
1091 Patras Rift (Greece) by U/Th method, and tectonic implications. *Geophysical Research Letters*. 28(19), pp.3769–  
1092 3772.
- 1093 Ford, M., Williams, E.A., Malartre, F. and Popescu, S.-M. 2007. Stratigraphic Architecture, Sedimentology and  
1094 Structure of the Vouraikos Gilbert-Type Fan Delta, Gulf of Corinth, Greece *In*: I. Jarvis, G. Nichols, E. Williams and  
1095 C. Paola, eds. *Sedimentary Processes, Environments and Basins, Special Publication of the International*  
1096 *Association of Sedimentologists.*, pp.49–90.
- 1097 Ford, M., Rohais, S., Williams, E.A., Bourlange, S., Jousselin, D., Backert, N. and Malartre, F. 2013. Tectono-  
1098 sedimentary evolution of the western Corinth rift (Central Greece). *Basin Research*. 25, pp.3–25.
- 1099 Ford, M., Hemelsdaël, R., Mancini, M. and Palyvos, N. 2016. Rift migration and lateral propagation: evolution of  
1100 normal faults and sediment-routing systems of the western Corinth rift (Greece) *In*: C. Childs, R. . Holdsworth, C.  
1101 A.-L. Jackson, T. Manzocchi, J. . Walsh and G. Yielding, eds. *The Geometry and Growth Of Normal Faults -*  
1102 *Geological Society Special Publications 439* Geological Society London, pp.131–168.
- 1103 Francke, A, Wagner, B., Just, J., Leicher, N., Gromig, R., Baumgarten, H., Vogel, H., Lacey, J.H., Sadori, L., Wonik,  
1104 T., Leng, M., Zanchetta, G., Sulpizio, R., Giacco, B. 2016. Sedimentological processes and environmental

- 1105 variability at Lake Ohrid (Macedonia, Albania) between 637 ka and the present. *Biogeosciences*, 13. pp. 1179-  
1106 1196
- 1107 Gasse, F., Lédée, V., Massault, M. and Fontes, J.C. 1989. Water-level fluctuations of Lake Tanganyika in phase  
1108 with oceanic changes during the last glaciation and deglaciation. *Nature*. 342, pp.57–59.
- 1109 Gawthorpe, R.L., Fraser, A.J. and Collier, R.E.L. 1994. Sequence stratigraphy in active extensional basins:  
1110 implications for the interpretation of ancient basin-fills. *Marine and Petroleum Geology*. 11, pp.642–658.
- 1111 Gawthorpe, R.L., Andrews, J.E., Collier, R.E.L., Ford, M., Henstra, G.A., Kranis, H., Leeder, M.R., Muravchik, M.,  
1112 Skourtsos, E. 2017. Building up or out? Disparate sequence architectures along an active rift margin – Corinth Rift,  
1113 Greece. *Geology*. 45 (12). pp. 1111-1114.
- 1114 Gawthorpe, R.L., Leeder, M.R., Kranis, H., Skourtsos, E., Andrews, J.E., Henstra, G.A., Mack, G.H., Muravchik,  
1115 M., Turner, J.A. and Stamatakis, M. 2018. Tectono-sedimentary evolution of the Plio-Pleistocene Corinth rift,  
1116 Greece. *Basin Research*. 30, pp.448–479.
- 1117 Geurts, A.H., Cowie, P.A., Duclaux, G., Gawthorpe, R.L., Huismans, R.S., Pedersen, V.K., Wedmore, L.N.J. 2018.  
1118 Drainage integration and sediment dispersal in active continental rifts: A numerical modelling study of the central  
1119 Italian Apennines. *Basin Research*. 30. pp. 965-989.
- 1120 Gobo, K., Ghinassi, M. and Nemec, W. 2014. Reciprocal Changes in Foreset to Bottomset Facies in a Gilbert-Type  
1121 Delta: Response to Short-Term Changes in Base Level. *Journal of Sedimentary Research*. 84, pp.1079–1095.
- 1122 Gobo, K., Ghinassi, M. and Nemec, W. 2015. Gilbert-type deltas recording short-term base-level changes: Delta-  
1123 brink morphodynamics and related foreset facies. *Sedimentology*. 62, pp.1923–1949.
- 1124 Gupta, S., Underhill, J., Sharp, I. and Gawthorpe, R.. 1999. Role of fault interactions in controlling synrift sediment  
1125 dispersal patterns: Miocene, Abu Alaqa Group, Suez Rift, Sinai, Egypt. *Basin Research*. 11(2), pp.167–189.
- 1126 Gutierrez-Pastor, J., Hans Nelson, C., Goldfinger, C., Johnson, J., Escutia, C., Eriksson, A. and Morey, A.. 2009.  
1127 Earthquake Control of Holocene Turbidite Frequency Confirmed by Hemipelagic Sedimentation Chronology on the  
1128 Cascadia and Northern California Active Continental Margins In: B. Kneller, O. Martinsen and B. McCaffrey, eds.  
1129 *External Controls on Deep-Water Depositional Systems SEPM Special Publication No. 92*. Tulsa, OK: SEPM  
1130 (Society for Sedimentary Geology), pp.179–197.
- 1131 Hadler-Jacobsen, F., Johannessen, E.P., Ashton, N., Henriksen, S., Johnson, S.D. and Kristensen, J.B. 2005.  
1132 Submarine fan morphology and lithology distribution: A predictable function of sediment delivery, gross shelf-to-  
1133 basin relief, slope gradient and basin topography In: Doré, A.G and Vining, B.A eds. *Petroleum Geology: North-  
1134 West Europe and Global Perspectives - Proceedings of the 6th Petroleum Geology Conference*, pp.1121–1145.
- 1135 Hajek, E.A. and Straub, K.M. 2017. Autogenic Sedimentation in Clastic Stratigraphy. *Annual Review of Earth and  
1136 Planetary Sciences*. 45, pp.681–709.
- 1137 Harris, A.D., Baumgardner, S.E., Sun, T. and Granjeon, D. 2018. A Poor Relationship Between Sea Level and  
1138 Deep-Water Sand Delivery. *Sedimentary Geology*. 370, pp.42–51.
- 1139 Harrison, S.P., Prentice, I.C. and Bartlein, P.J. 1992. Influence of insolation and glaciation on atmospheric  
1140 circulation in the North Atlantic sector: Implications of general circulation model experiments for the Late  
1141 Quaternary climatology of Europe. *Quaternary Science Reviews*. 11, pp.283–299.

- 1142 Hay, C., Mitrovica, J.X., Gomez, N., Creveling, J.R., Austermann, J. and Kopp, R.R. 2014. The sea-level  
1143 fingerprints of ice-sheet collapse during interglacial periods. *Quaternary Science Reviews*. 87, pp.60–69.
- 1144 Heezen, B.C., Ewing, M. and Johnson, G.L. 1966. The Gulf of Corinth floor. *Deep-Sea Research and*  
1145 *Oceanographic Abstracts*. 13, pp.381–411.
- 1146 Henstra, G.A., Grundvåg, S.-A., Johannessen, E.P., Kristensen, T.B., Midtkandal, I., Nystuen, J.P., Rotevatn, A.,  
1147 Surlyk, F., Sæther, T. and Windelstad, J. 2016. Depositional processes and stratigraphic architecture within a  
1148 coarse-grained rift-margin turbidite system: The Wollaston Forland Group, east Greenland. *Marine and Petroleum*  
1149 *Geology*. 76, pp.187–209.
- 1150 Horsch, G.M. and Fourniotis, N.T. 2018. On strong nearshore wind-induced currents in flow-through gulfs:  
1151 Variations on a theme by Csanady. *Water*. 10, pp.1–14.
- 1152 Hughes, P.D., Woodward, J.C. and Gibbard, P.L. 2006. Late Pleistocene glaciers and climate in the Mediterranean.  
1153 *Global and Planetary Change*. 50, pp.83–98.
- 1154 Hughes, P.D., Woodward, J.C. and Gibbard, P.L. 2007. Middle Pleistocene cold stage climates in the  
1155 Mediterranean: New evidence from the glacial record. *Earth and Planetary Science Letters*. 253, pp.50–56.
- 1156 Hughes, P.D. and Woodward, J.C. 2017. Quaternary glaciation in the Mediterranean mountains: A new synthesis  
1157 *In: P. D. Hughes and J. . Woodward, eds. Quaternary Glaciation in the Mediterranean Mountains, Geological*  
1158 *Society of London Special Publications No. 433*. Geological Society of London, pp.1–23.
- 1159 Imbrie, J., Berger, A., Boyle, E.A., Clemens, S.C., Duffy, A., Howard, W.R., Kukla, G., Kutzbach, J., Martinson,  
1160 D.G., McIntyre, A., Mix, A.C., Molfino, B., Morley, J.J. , Peterson, L.C., Pisas, N.G., Prell, W.L., Raymo, M.E.,  
1161 Shackleton, N.J. and Toggweiler, J.R., 1993. On the structure and origin of major glaciation cycles 2. The 100,000-  
1162 year cycle. *Paleoceanography*. 8( 6), pp.699– 735
- 1163 Istanbuluoglu, E. and Bras, R.L. 2005. Vegetation-modulated landscape evolution: Effects of vegetation on  
1164 landscape processes, drainage density, and topography. *Journal of Geophysical Research: Earth Surface*. 110,  
1165 pp.1–19.
- 1166 Jerolmack, D.J. and Paola, C. 2010. Shredding of environmental signals by sediment transport. *Geophysical*  
1167 *Research Letters*. 37(19), pp.1–5.
- 1168 Joannin, S., Quillévéré, F., Suc, J.-P., Lécuyer, C. and Martineau, F. 2007a. Early Pleistocene climate changes in  
1169 the central Mediterranean region as inferred from integrated pollen and planktonic foraminiferal stable isotope  
1170 analyses. *Quaternary Research*. 67, pp.264–274.
- 1171 Joannin, S., Cornée, J.-J., Moissette, P., Suc, J.-P., Koskeridou, E., Lécuyer, C., Buisine, C., Kouli, K. and Ferry,  
1172 S. 2007b. Changes in vegetation and marine environments in the eastern Mediterranean (Rhodes, Greece) during  
1173 the Early and Middle Pleistocene. *Journal of the Geological Society*. 164, pp.1119–1131.
- 1174 Joannin, S., Ciaranfi, N. and Stefanelli, S. 2008. Vegetation changes during the late Early Pleistocene at  
1175 Montalbano Jonico (Province of Matera, southern Italy) based on pollen analysis. *Palaeogeography,*  
1176 *Palaeoclimatology, Palaeoecology*. 270, pp.92–101.
- 1177 Jobe, Z.R., Sylvester, Z., Howes, N., Pirmez, C., Parker, A., Cantelli, A., Smith, R., Wolinsky, M.A., O'Byrne, C.,  
1178 Slowey, N. and Prather, B. 2017. High-resolution, millennial-scale patterns of bed compensation on a sand-rich  
1179 intraslope submarine fan, western Niger Delta slope. *Bulletin of the Geological Society of America*. 129, pp.23–37.

- 1180 Kiro, Y., Goldstein, S.L., Garcia-Veigas, J., Levy, E., Kushnir, Y., Stein, M. and Lazar, B. 2017. Relationships  
 1181 between lake-level changes and water and salt budgets in the Dead Sea during extreme aridities in the Eastern  
 1182 Mediterranean. *Earth and Planetary Science Letters*. 464, pp.211–226.
- 1183 Kirschvink, J. L. 1980. The least-squares line and plane and the analysis of palaeomagnetic data. *Geophys. J. R.*  
 1184 *Astron. Soc.* 62 pp.699–718.
- 1185 Kneller, B.C., Martinsen, O.J. and McCaffrey, B. 2009. External controls on deep-water sedimentary systems:  
 1186 challenges and perspectives *In: External Controls on Deep-Water Depositional Systems* SEPM Special Publication  
 1187 No.92. (Kneller, B., Martinsen, O. and McCaffrey, B., eds.). Tulsa, OK: SEPM (Society for Sedimentary Geology),  
 1188 pp.5–12.
- 1189 Kouli, K., Brinkhuis, H. and Dale, B. 2001. Spiniferites cruciformis: A fresh water dinoflagellate cyst? *Review of*  
 1190 *Palaeobotany and Palynology*. 113, pp.273–286.
- 1191 Koymans, M.R., Langereis, C.G., Pastor-Galán, D. and van Hinsbergen, D.J.J. 2016. Paleomagnetism.org: An  
 1192 online multi-platform open source environment for paleomagnetic data analysis. *Computers and Geosciences*. 93  
 1193 pp.127–137.
- 1194 Lacey, J. H., Leng, M.J., Francke, A., Sloane, H.J., Milodowski, A., Vogel, H., Baumgarten, H., Zanchetta, G.,  
 1195 Wagner, B. 2016. Northern Mediterranean climate since the Middle Pleistocene: a 637 ka stable isotope record  
 1196 from Lake Ohrid (Albania/Macedonia). *Biogeosciences* 13, pp. 1801–1820.
- 1197 Leeder, M.R., Harris, T., Kirkby, M.J., and Hovius, N. 1998. Sediment supply and climate change: implications for  
 1198 basin stratigraphy. *Basin Research*. 10, pp.7–18.
- 1199 Leeder, M.R., McNeill, L.C., Collier, R.E.L., Portman, C., Rowe, P.J., Andrews, J.E. and Gawthorpe, R.L. 2003.  
 1200 Corinth Rift margin uplift: new evidence from Late Quaternary marine shorelines. *Geophysical Research Letters*.  
 1201 30(12), p.1611.
- 1202 Leeder, M. R., Mark, D. F., Gawthorpe, R. L., Kranis, H., Loveless, S., Pedentchouk, N., Stamatakis, M. .2012. A  
 1203 'Great Deepening': Chronology of rift climax, Corinth rift, Greece. *Geology*, 40, 999– 1002.
- 1204 Leontaritis, A., Kouli, K. and Pavlopoulos, K. 2020. The glacial history of Greece: a comprehensive review.  
 1205 *Mediterranean Geoscience Reviews*
- 1206 Malartre, F., Ford, M. and Williams, E.A. 2004. Preliminary biostratigraphy and 3D geometry of the Vouraikos  
 1207 Gilbert-type fan delta, Gulf of Corinth, Greece. *Comptes Rendus Geoscience*. 336, pp.269–280.
- 1208 Marinova, E., Harrison, S.P., Bragg, F., Connor, S., Laet, V. de Leroy, S.A.G., Mudie, P., Atanassova, J.,  
 1209 Bozilova, E., Carner, H., Cordova, C., Djamali, M., Filipova-Marinova, M., Gerasimenko, N., Jahns, N., Kouli, K.,  
 1210 Kotthoff, U., Kvavadze, E., Lazarova, M., Novenko, E., Ramezani, E., Röpke, A., Shumilovskikh, L., Tanțău, I.,  
 1211 Tonkov, S. 2018. Pollen-derived biomes in the Eastern Mediterranean–Black Sea–Caspian–Corridor. *Journal of*  
 1212 *Biogeography* 45, 484–499.
- 1213 Marshall, M.H., Lamb, H.F., Huws, D., Davies, S.J., Bates, R., Bloemendal, J., Boyle, J., Leng, M.J., Umer, M. and  
 1214 Bryant, C. 2011. Late Pleistocene and Holocene drought events at Lake Tana, the source of the Blue Nile. *Global*  
 1215 *and Planetary Change*. 78, pp.147–161.
- 1216 Marston, R.A. 2010. Geomorphology and vegetation on hillslopes: Interactions, dependencies, and feedback loops.  
 1217 *Geomorphology*. 116(3–4), pp.206–217.

- 1218 Maslin, M.A. and Ridgwell, A.J. 2005. Mid-Pleistocene revolution and the 'eccentricity myth' *In*: M. Head and P.  
 1219 Gibbard, eds. *Early-Middle Pleistocene Transitions: The Land-Ocean Evidence. Geological Society London*  
 1220 *Special Publication No. 247.*, pp.19–34.
- 1221 McArthur, A., Kneller, B., Wakefield, M., Souza, P. and Kuchle, J. 2016a. Palynofacies classification of the  
 1222 depositional elements of confined turbidite systems: Examples from the Gres d'Annot, SE France. *Marine and*  
 1223 *Petroleum Geology*. 77, pp.1254–1273.
- 1224 McArthur, A. D., Kneller, B.C., Souza, P.A. and Kuchle, J. 2016b. Characterization of deep-marine channel-levee  
 1225 complex architecture with palynofacies: An outcrop example from the Rosario Formation, Baja California, Mexico.  
 1226 *Marine and Petroleum Geology*. 73, pp.157–173.
- 1227 McArthur, Adam D., Jolley, D.W., Hartley, A.J., Archer, S.G. and Lawrence, H.M. 2016c. Palaeoecology of syn-rift  
 1228 topography: A Late Jurassic footwall island on the Josephine Ridge, Central Graben, North Sea. *Palaeogeography,*  
 1229 *Palaeoclimatology, Palaeoecology*. 459, pp.63–75.
- 1230 McNeil, L.C., Cotterill, C.J., Henstock, T.J., Bull, J.M., Stefatos, T.J., Collier, R.E.L., Papatheoderou, G., Ferentinos,  
 1231 G. and Hicks, S.E. 2005. Active faulting within the offshore western Gulf of Corinth, Greece: Implications for models  
 1232 of continental rift deformation. *Geology*. 33, pp.241–244.
- 1233 McNeill, Lisa C, Shillington, D.J., Carter, G.D.O., Everest, J.D., Gawthorpe, R.L., Miller, C., Phillips, M.P., Collier,  
 1234 R.E.L., Cvetkoska, A., Gelder, G. De, Diz, P., Doan, M. and Ford, M. 2019a. High-resolution record reveals climate-  
 1235 driven environmental and sedimentary changes in an active rift. *Scientific Reports*. 9, pp.1–11.
- 1236 McNeill, L.C., Shillington, D.J., Carter, G.D.O., Everest, J.D., Le Ber, E., Collier, R.E., Cvetkoska, A., De Gelder,  
 1237 G., Diz, P., Doan, M.L., Ford, M., Gawthorpe, R.L., Geraga, M., Gillespie, J., Hemelsdaël, R., Herrero-Bervera, E.,  
 1238 Ismaiel, M., Janikian, L., Kouli, K., Li, S., Machlus, M.L., Maffione, M., Mahoney, C., Michas, G., Miller, C., Nixon,  
 1239 C.W., Oflaz, S.A., Omale, A.P., Panagiotopoulos, K., Pechlivanidou, S., Phillips, M.P., Sauer, S., Seguin, J.,  
 1240 Sergiou, S. and Zakharova, N.V. 2019b. Expedition 381 summary *In: Proceedings of the International Ocean*  
 1241 *Discovery Program Volume 381*. IODP.
- 1242 McNeill, L C, Shillington, D.J., Carter, G.D.O., Everest, J.D., Le Ber, E., Collier, R.E.L., Cvetkoska, A., De Gelder,  
 1243 G., Diz, P., Doan, M.L., Ford, M., Gawthorpe, R., Geraga, M., Gillespie, J., Hemelsdaël, R., Herrero-Bervera, E.,  
 1244 Ismaiel, M., Janikian, L., Kouli, K., Li, S., Machlus, M.L., Maffione, M., Mahoney, C., Michas, G., Miller, C., Nixon,  
 1245 C.W., Oflaz, S.A., Omale, A.P., Panagiotopoulos, K., Pechlivanidou, S., Phillips, M.P., Sauer, S., Seguin, J.,  
 1246 Sergiou, S. and Zakharova, N. V 2019c. Expedition 381 methods *In: Proceedings of the International Ocean*  
 1247 *Discovery Program Volume 381*. IODP.
- 1248 McNeill, L.C., Shillington, D.J., Carter, G.D.O., Everest, J.D., Le Ber, E., Collier, R.E., Cvetkoska, A., De Gelder,  
 1249 G., Diz, P., Doan, M.L., Ford, M., Gawthorpe, R.L., Geraga, M., Gillespie, J., Hemelsdaël, R., Herrero-Bervera, E.,  
 1250 Ismaiel, M., Janikian, L., Kouli, K., Li, S., Machlus, M.L., Maffione, M., Mahoney, C., Michas, G., Miller, C., Nixon,  
 1251 C.W., Oflaz, S.A., Omale, A.P., Panagiotopoulos, K., Pechlivanidou, S., Phillips, M.P., Sauer, S., Seguin, J.,  
 1252 Sergiou, S. and Zakharova, N.V. 2019d. Site M0080 *In: Proceedings of the International Ocean Discovery Program*  
 1253 *Volume 381*. IODP.
- 1254 McNeill, L.C., Shillington, D.J., Everest, J.D., Ber, E. Le, Cvetkoska, A., Gelder, G. De, Diz, P., Ford, M., Gawthorpe,  
 1255 R.L., Geraga, M., Gillespie, J., Ismaiel, M., Janikian, L., Kouli, K., Li, S., Machlus, M.L., Maffione, M., Mahoney, C.,  
 1256 Michas, G., Miller, C., Nixon, C.W., Oflaz, S.A., Omale, A.P., Panagiotopoulos, K., Pechlivanidou, S., Phillips, M.P.,

- 1257 Sauer, S., Seguin, J., Sergiou, S., Zakharova, N. V, Gulf, A., Sea, M. and Sea, A. 2019e. Site M0079 In: *Proceedings*  
1258 *of the International Ocean Discovery Program Volume 381*. IODP.
- 1259 McNeill, L.C., Shillington, D.J., Carter, G.D.O., Everest, J.D., Le Ber, E., Collier, R.E., Cvetkoska, A., De Gelder,  
1260 G., Diz, P., Doan, M.L., Ford, M., Gawthorpe, R.L., Geraga, M., Gillespie, J., Hemelsdaël, R., Herrero-Bervera, E.,  
1261 Ismaiel, M., Janikian, L., Kouli, K., Li, S., Machlus, M.L., Maffione, M., Mahoney, C., Michas, G., Miller, C., Nixon,  
1262 C.W., Oflaz, S.A., Omale, A.P., Panagiotopoulos, K., Pechlivanidou, S., Phillips, M.P., Sauer, S., Seguin, J.,  
1263 Sergiou, S. and Zakharova, N.V. 2019f. Site M0078 In: *Proceedings of the International Ocean Discovery Program*  
1264 *Volume 381*. IDOP.
- 1265 Mertens, K.N., Price, A.M. and Pospelova, V. 2012a. Determining the absolute abundance of dinoflagellate cysts  
1266 in recent marine sediments II: Further tests of the Lycopodium marker-grain method. *Review of Palaeobotany and*  
1267 *Palynology*. 184, pp.74–81.
- 1268 Mertens, K.N., Rengefors, K., Moestrup, Ø., and Ellegaard, M. 2012b. A review of recent freshwater dinoflagellate  
1269 cysts: taxonomy, phylogeny, ecology and palaeoecology. *Phycologia*. 51, pp.612–619.
- 1270 Morzadec-Kerfourn, M.T. 2005. Interaction between sea-level changes and the development of littoral herbaceous  
1271 vegetation and autotrophic dinoflagellates. *Quaternary International*. 133–134, pp.137–140.
- 1272 Mudie, P.J., Aksu, A.E. and Yasar, D. 2001. Late Quaternary dinoflagellate cysts from the Black, Marmara and  
1273 Aegean seas: Variations in assemblages, morphology and paleosalinity. *Marine Micropaleontology*. 43, pp.155–  
1274 178.
- 1275 Mudie, P.J., Marret, F., Rochon, A. and Aksu, A.E. 2010. Non-pollen palynomorphs in the Black Sea corridor.  
1276 *Vegetation History and Archaeobotany*. 19, pp.531–544.
- 1277 Mudie, P.J., Marret, F., Mertens, K.N., Shumilovskikh, L. and Leroy, S.A.G. 2017. Atlas of modern dinoflagellate  
1278 cyst distributions in the Black Sea Corridor: from Aegean to Aral Seas, including Marmara, Black, Azov and Caspian  
1279 Seas. *Marine Micropaleontology*. 134, pp.1–152.
- 1280 Muntzos, T. 1992. Palyno– und Paläoklima-Stratigraphie der pliozänen und altpleistozänen Sedimente der  
1281 nördlichen und nordwestli- chen Peloponnes. *Newsletters on Stratigraphy*. 27, pp.71–91.
- 1282 Muravchik, M., Gawthorpe, R.L., Sharp, I.R., Rarity, F. and Hodgetts, D. 2018. Sedimentary environment evolution  
1283 in a marine hangingwall dip slope setting. El Qaa Fault Block, Suez Rift, Egypt. *Basin Research*. 30. pp. 452-478.
- 1284 Nelson, C., Escutia, C., Goldfinger, C., Karabanov, E., Gutierrez-Pastor, J. and De Batist, M. 2009. External  
1285 Controls on Modern Clastic Turbidite Systems: Three Case Studies In: B. Kneller, O. Martinsen and B. McCaffrey,  
1286 eds. *External Controls on Deep-Water Depositional Systems SEPM Special Publications*. No. 92. Tulsa, OK: SEPM  
1287 (Society for Sedimentary Geology), pp.57–76.
- 1288 Nguyen, N., Duffy, B., Shulmeister, J. and Quigley, M. 2013. Rapid Pliocene uplift of Timor. *Geology*. 41, pp.179–  
1289 182.
- 1290 Nixon, C.W., McNeill, L.C., Bull, J.M., Bell, R.E., Gawthorpe, R.L., Henstock, T.J., Christodoulou, D., Ford, M.,  
1291 Taylor, B., Sakellariou, D., Ferentinos, G., Papatheodorou, G., Leeder, M.R., Collier, R.E.L.I., Goodliffe, A.M.,  
1292 Sachpazi, M. and Kranis, H. 2016. Rapid spatiotemporal variations in rift structure during development of the  
1293 Corinth Rift, central Greece. *Tectonics*. 35, pp.1225–1248.



- 1294 Nyberg, B., Helland-Hansen, W., Gawthorpe, R.L., Sandbakken, P., Haug Eide, C., Sømme, T., Hadler-Jacobsen,  
1295 F., Leiknes, S. 2018. Revisiting morphological relationships of modern source-to-sink segments as a first-order  
1296 approach to scale ancient sedimentary systems. *Sedimentary Geology*. 373 pp. 111-133
- 1297 Okuda, M., Yasuda, Y. and Setoguchi, T. 2008. Middle to Late Pleistocene vegetation history and climatic changes  
1298 at Lake Kopais, Southeast Greece. *Boreas*. 30 (1). pp. 73-82.
- 1299 Panagiotopoulos, K., Holtvoeth, J., Kouli, K., Marinova, E., Francke, A., Cvetkoska, A., Jovanovska, E., Lacey,  
1300 J.H., Lyons, E.T., Buckel, C., Bertini, A., Donders, T., Just, J., Leicher, N., Leng, M.J., Melles, M., Pancos, R.D.,  
1301 Sadori, L., Tauber, P., Vogel, H., Wagner, B. and Wilke, T. 2020. Insights into the evolution of the young Lake Ohrid  
1302 ecosystem and vegetation succession from a southern European refugium during the Early Pleistocene.  
1303 *Quaternary Science Reviews*. 227.
- 1304 Papadopoulou, P., Iliopoulos, G., Zidianakis, I. and Tsoni, M. 2018. Vegetation and palaeoclimatic reconstruction  
1305 of the Sousaki Basin (eastern Gulf of Corinth, Greece) during the Early Pleistocene. *Quaternary International*.  
1306 476, pp.110–119
- 1307 Papadopoulos, G.A. 2003. Tsunami hazard in the Eastern Mediterranean: Strong earthquakes and tsunamis in  
1308 Cyprus and the Levantine Sea. *Natural Hazards*. 40(3), pp.503–526.
- 1309 Paropkari, A.L., Prakash Babu, C. and Mascarenhas, A. 1992. A critical evaluation of depositional parameters  
1310 controlling the variability of organic carbon in Arabian Sea sediments. *Marine Geology*. 107(3).
- 1311 Pechlivanidou, S., Cowie, P.A., Hannisdal, B., Whittaker, A.C., Gawthorpe, R.L., Pennos, C. and Riiser, O.S. 2018.  
1312 Source-to-sink analysis in an active extensional setting: Holocene erosion and deposition in the Sperchios rift,  
1313 central Greece. *Basin Research*. 30, pp.522–543.
- 1314 Pechlivanidou, S., Cowie, P.A., Duclaux, G., Nixon, C.W., Gawthorpe, R.L. and Salles, T. 2019. Tipping the  
1315 balance: Shifts in sediment production in an active rift setting. *Geology*. 47, pp.259–262.
- 1316 Piper, D.J.W. 2006. Sedimentology and tectonic setting of the Pindos Flysch of the Peloponnese, Greece *in*:  
1317 Robertson, A.H.F and Mountrakis, D (eds.) *Tectonic Development of the Eastern Mediterranean Region*,  
1318 *Geological Society of London Special Publication No. 260*. Geological Society of London, pp. 493-505.
- 1319 Pope, R.J., Hughes, P.D. and Skourtsos, E. 2017. Glacial history of Mt Chelmos, Peloponnese, Greece *In*:  
1320 Hughes, P.D & Woodward, J.C eds. *Quaternary Glaciation in the Mediterranean Mountains*, *Geological Society of*  
1321 *London Special Publication No 433*. Geological Society of London, pp.211–236.
- 1322 Posamentier, H.W. and Vail, P.R. 1988. Eustatic controls on clastic deposition II: sequence and systems tract  
1323 models *In*: C. K. Wilgus, B. S. Hastings, H. Posamentier, J. Van Wagoner, C. A. Ross and C. G. S. C. Kendall,  
1324 eds. *Sea-level changes: an integrated approach*. *SEPM Special Publication No.42*. SEPM, Tulsa, OK pp.125–154.
- 1325 Prentice, C., Guiot, J., Huntley, B., Jolly, D., Cheddadi, R. 1996. Reconstructing biomes from palaeoecological  
1326 data: a general method and its application to European pollen data at 0 and 6 ka. *Climate Dynamics*. 12. pp 185-  
1327 194.
- 1328 Rohais, S. and Moretti, I. 2017. Structural and Stratigraphic Architecture of the Corinth Rift (Greece): An Integrated  
1329 Onshore to Offshore Basin-Scale Synthesis *In*: F. Roure, A. A. Amin, S. Khomsi and M. A. Al Garni, eds.  
1330 *Lithosphere Dynamics and Sedimentary Basins of the Arabian Plate and Surrounding Areas*. Springer International  
1331 Publishing, *Frontiers in Earth Sciences*, pp.89–120.

- 1332 Rohais, S., Eschard, R., Ford, M., Guillocheau, F. and Moretti, I. 2007a. Stratigraphic architecture of the Plio-  
1333 Pleistocene infill of the Corinth Rift: Implications for its structural evolution. *Tectonophysics*. 440, pp.5–28.
- 1334 Rohais, S., Joannin, S., Colin, J.P., Suc, J.P., Guillocheau, F. and Eschard, R. 2007b. Age and environmental  
1335 evolution of the syn-rift fill of the southern coast of the gulf of Corinth (Akrata-Derveni region, Greece). *Bulletin de*  
1336 *la Societe Geologique de France*. 178(3), pp.231–243.
- 1337 Rohais, S., Eschard, R. and Guillocheau, F. 2008. Depositional model and stratigraphic architecture of rift climax  
1338 Gilbert-type fan deltas (Gulf of Corinth, Greece). *Sedimentary Geology*. 210, pp.132–145.
- 1339 Romans, B.W., Castellort, S., Covault, J.A., Fildani, A. and Walsh, J.P. 2016. Environmental signal propagation in  
1340 sedimentary systems across timescales. *Earth-Science Reviews*. 153, pp.7–29.
- 1341 Rovere, A., Stocchi, P. and Vacchi, M. 2016. Eustatic and Relative Sea Level Changes. *Current Climate Change*  
1342 *Reports*. 2(4), pp.221–231.
- 1343 Rubi, R., Rohais, S., Bourquin, S., Moretti, I. and Desaubliaux, G. 2018. Processes and typology in Gilbert-type  
1344 delta bottomset deposits based on outcrop examples in the Corinth Rift. *Marine and Petroleum Geology*. 92,  
1345 pp.193–212.
- 1346 Sømme, T.O., Helland-Hansen, W., Martinsen, O.J., Thurmond, J.B. 2009. Relationships between morphological  
1347 and sedimentological parameters in source-to-sink systems: a basis for predicting semi-quantitative characteristics  
1348 in subsurface systems. *Basin Research*. 21 (4). pp. 361-387
- 1349 Sømme, T.O., Skogseid, J., Embry, P. and Løseth, H. 2019. Manifestation of Tectonic and Climatic Perturbations  
1350 I Deep-Time Stratigraphy – An Example From the Paleocene Succession offshore Western Norway. *Frontiers in*  
1351 *Earth Science*. 7:303.
- 1352 Sadori, L., Koutsodendris, A., Panagiotopoulos, K., Masi, A., Bertini, A., Combourieu-Nebout, N., Francke, A.,  
1353 Kouli, K., Joannin, S., Mercuri, A.M., Peyron, O., Torri, P., Wagner, B., Zanchetta, G., Sinopoli, G. and Donders,  
1354 T.H. 2016. Pollen-based paleoenvironmental and paleoclimatic change at Lake Ohrid (south-eastern Europe)  
1355 during the past 500 ka. *Biogeosciences*. 13 (5). pp.1423–1437.
- 1356 Schmid, M., Ehlers, T.A., Werner, C., Hickler, T. and Fuentes-Espoz, J.-P. 2018. Effect of changing vegetation and  
1357 precipitation on denudation-Part 2: Predicted landscape response to transient climate and vegetation cover over  
1358 millennial to million-year timescales. *Earth Surface Dynamics*. 6, pp.859–881.
- 1359 Sergiou, S., Beckers, A., Geraga, M., Papatheodorou, G., Iliopoulos, I. and Papaefthymiou, H. 2016. Recent  
1360 Sedimentary Processes in the Western Gulf of Corinth, Greece: Seismic and Aseismic Turbidites. *Bulletin of the*  
1361 *Geological Society of Greece*. 50, pp.383–391.
- 1362 Simpson, G. and Castellort, S. 2012. Model shows that rivers transmit high-frequency climate cycles to the  
1363 sedimentary record. *Geology*. 40(12), pp.1131–1134.
- 1364 Singer, B. 2014. A quaternary geomagnetic instability time scale. *Quaternary Geochronology*. 21. pp. 29-52.
- 1365 Skourtsos, E. and Kranis, H. 2009. Structure and evolution of the western Corinth Rift , through new field data from  
1366 the Northern Peloponnesus In: U. Ring and B. Wernicke, eds. *Geological Society, London, Special Publication 321.*  
1367 *Extending a Continent: Architecture, Rheology and Heat Budget*. pp.119–138.

- 1368 Skourtsos, E., Kranis, H., Zambetakis-Lekkas, A., Gawthorpe, R. and Leeder, M. 2016. Alpine Basement  
1369 Outcrops at Northern Peloponnesus: Implications for the Early Stages in the Evolution of the Corinth Rift. *Bulletin*  
1370 *of the Geological Society of Greece*. 50, pp.153–163.
- 1371 Smith, G.W., Nance, R.D. and Genes, A.N. 1997. Quaternary glacial history of Mount Olympus, Greece. *Bulletin*  
1372 *of the Geological Society of America*. 109, pp.809–824.
- 1373 Stockmarr, J. 1971. Tablets with spores used in absolute pollen analysis. *Pollen et Spores*. XIII(January 1971),  
1374 pp.615–621.
- 1375 Strachan, L.J., Rarity, F., Gawthorpe, R.L., Wilson, P., Sharp, I. and Hodgetts, D. 2013. Submarine slope processes  
1376 in rift-margin basins, Miocene Suez Rift, Egypt. *Bulletin of the Geological Society of America*. 125, pp.109–127.
- 1377 Straub, K., Duller, R.A., Foreman, B.Z., Hajek, E.A. 2020. Buffered, Incomplete, and Shredded: The Challenges of  
1378 Reading an Imperfect Stratigraphic Record. *Journal of Geophysical Research: Earth Surface*. 125 (3),  
1379 e2019JF005079.
- 1380 Suc, J.P. and Popescu, S.M. 2005. Pollen records and climatic cycles in the North Mediterranean region since 2.7  
1381 Ma In: M. . Head and P. L. Gibbard, eds. *Early-Middle Pleistocene Transitions: The Land-Ocean Evidence*.  
1382 *Geological Society London Special Publication No. 247*. Geological Society London, pp.147–158.
- 1383 Symeonidis, N., Theodorou, G., Schutt, H. and Veleitzelos, E. 1987. Paleontological and stratigraphic  
1384 observations in the area of Achaia and Etoloakarnania (W.Greece). *Annales Geologiques de Pays Helleniques*. 38,  
1385 pp.317–353.
- 1386 Szczepanek, K., Myszkowska, D., Worobiec, E., Piotrowicz, K., Ziemianin, M. and Bielec-Bąkowska, Z. 2017. The  
1387 long-range transport of Pinaceae pollen: an example in Kraków (southern Poland). *Aerobiologia*. 33, pp.109–  
1388 125. Taylor, B., Weiss, J.R., Goodliffe, A.M., Sachpazi, M., Laigle, M. and Hirn, A. 2011. The structures, stratigraphy  
1389 and evolution of the Gulf of Corinth rift, Greece. *Geophysical Journal International*. 185, pp.1189–1219.
- 1390 Taylor, B., Weiss, J.R., Goodliffe, A.M., Sachpazi, M., Laigle, M. and Hirn, A. 2011. The structures, stratigraphy  
1391 and evolution of the Gulf of Corinth rift, Greece. *Geophysical Journal International*. 185(3) pp.1189–1219.
- 1392 Tofelde, S., Bernhardt, A., Guerit, L. and Romans, B.W. 2021. Times Associated With Source-to-Sink Propagation  
1393 of Environmental Signals During Landscape Transience. *Frontiers in Earth Science: Sedimentology, Stratigraphy*  
1394 *and Diagenesis* 9:628315. doi: 10.3389/feart.2021.628315
- 1395 Torfstein, A., Goldstein, S.L., Stein, M. and Enzel, Y. 2013. Impacts of abrupt climate changes in the Levant from  
1396 Last Glacial Dead Sea levels. *Quaternary Science Reviews*. 69, pp.1–7.
- 1397 Toucanne, S., Zaragosi, S., Bourillet, J.F., Dennielou, B., Jorry, S.J., Jouet, G. and Cremer, M. 2012. External  
1398 controls on turbidite sedimentation on the glacially-influenced Armorican margin (Bay of Biscay, western European  
1399 margin). *Marine Geology*. 303–306, pp.137–153.
- 1400 Trenberth, K.E., Dai, A., Rasmussen, R.M. and Parsons, D.B. 2003. The changing character of precipitation.  
1401 *Bulletin of the American Meteorological Society*. 84(9), pp.1205-1217+1161.
- 1402 Tucker, G.E., McCoy, S.W., Whittaker, A.C., Roberts, G.P., Lancaster, S.T. and Phillips, R. 2011. Geomorphic  
1403 significance of postglacial bedrock scarps on normal-fault footwalls. *Journal of Geophysical Research: Earth*  
1404 *Surface*. 116(1), pp.1–14.
- 1405 Tyson, R.. 1995. Sedimentary Organic Matter: Organic facies and palynofacies. *Chapman & Hall*, London.

- 1406 Tzedakis, P.C., Hooghiemstra, H. and Pälike, H. 2006. The last 1.35 million years at Tenaghi Philippon: revised  
1407 chronostratigraphy and long-term vegetation trends. *Quaternary Science Reviews*. 25, pp.3416–3430.
- 1408 Vidal, G. 1988. American Association of Stratigraphic Palynologists A Palynological Preparation Method  
1409 Stratigraphic Palynologists. *Palynology*. 12, pp.215–220.
- 1410 Wagner, B., Vogel, H., Francke, A., Friedrich, T., Donders, T., Lacey, J.H., Leng, M.J., Regattieri, E., Sadori, L.,  
1411 Wilke, T., Zanchetta, G., Albrecht, C., Bertini, A., Combourieu-Nebout, N., Cvetkoska, A., Giaccio, B., Grazhdani,  
1412 A., Hauffe, T., Holtvoeth, J., Joannin, S., Jovanovska, E., Just, J., Kouli, K., Kousis, I., Koutsodendris, A., Krastel,  
1413 S., Lagos, M., Leicher, N., Levkov, Z., Lindhorst, K., Masi, A., Melles, M., Mercuri, A.M., Nomade, S., Nowaczyk,  
1414 N., Panagiotopoulos, K., Peyron, O., Reed, J.M., Sagnotti, L., Sinopoli, G., Stelbrink, B., Sulpizio, R., Timmermann,  
1415 A., Tofilovska, S., Torri, P., Wagner-Cremer, F., Wonik, T. and Zhang, X. 2019. Mediterranean winter rainfall in  
1416 phase with African monsoons during the past 1.36 million years. *Nature*. 573, pp.256–260.
- 1417 Watkins, S.E., Whittaker, A.C., Bell, R.E., McNeill, L.C., Gawthorpe, R.L., Brooke, S.A.S. and Nixon, C.W. 2018.  
1418 Are landscapes buffered to high-frequency climate change? A comparison of sediment fluxes and depositional  
1419 volumes in the Corinth Rift, central Greece, over the past 130 k.y. *Bulletin of the Geological Society of America*.  
1420 131, pp.372–388.
- 1421 Watkins, S.E., Whittaker, A.C., Bell, R.E., Brooke, S.A.S., Ganti, V., Gawthorpe, R.L., McNeill, L.C. and Nixon,  
1422 C.W. 2020. Straight from the source’s mouth: Controls on field-constrained sediment export across the entire active  
1423 Corinth Rift, central Greece. *Basin Research*, doi: 10.1111/bre.12444
- 1424 Westaway, R. 2002. The Quaternary evolution of the Gulf of Corinth, central Greece: coupling between surface  
1425 processes and flow in the lower continental crust. *Tectonophysics*. 348, pp.269–318.
- 1426 Whittaker, A.C., Attal, M. and Allen, P.A. 2010. Characterising the origin, nature and fate of sediment exported from  
1427 catchments perturbed by active tectonics. *Basin Research*. 22(6), pp.809–828.
- 1428 Whittaker, A.C., Duller, R.A., Springett, J., Smithells, R.A., Whitchurch, A.L. and Allen, P.A. 2011. Decoding  
1429 downstream trends in stratigraphic grain size as a function of tectonic subsidence and sediment supply. *Bulletin of*  
1430 *the Geological Society of America*. 123(7–8), pp.1363–1382.
- 1431 Woodward, J.C., Lewin, J. and MacKlin, M.G. 1992. Alluvial sediment sources in a glaciated catchment: The  
1432 voidomatis basin, Northwest Greece. *Earth Surface Processes and Landforms*. 17(3), pp.205–216.
- 1433 Yang, T., Hyodo M., Yang, Z., Fu, J., 2004. Evidence for the Kamikatsura and Santa Rosa excursions recorded in  
1434 eolian deposits from the Southern Chinese Loess Plateau. *Journal of Geophysical Research: Solid Earth*. 109(12).  
1435 pp. 1-10.
- 1436 Zhang, J., Burgess, P.M., Granjeon, D. and Steel, R. 2019a. Can sediment supply variations create sequences?  
1437 Insights from stratigraphic forward modelling. *Basin Research*. 31, pp.274–289.
- 1438 Zhang, J., Kim, W., Olariu, C. and Steel, R. 2019b. Accommodation- versus supply-dominated systems for  
1439 sediment partitioning to deep water. *Geology*. 47, pp.1–4.
- 1440 Zhong, X., Escalona, A., Sverdrup, E. and Bukta, K.E. 2018. Impact of fault evolution in Gilbert-type fan deltas in  
1441 the Evrostini area, south-central Gulf of Corinth, Greece. *Marine and Petroleum Geology*. 95, pp.82–99.

1442 Zobaa, M.K., Salah, Y., Taha, A.A. and Oboh-ikuenobe, F.E. 2015. Improved Graphical Representation of  
1443 Sedimentary Organic Matter as Paleoenvironmental Parameters *In: GSA 2015 Conference Proceedings.*  
1444 *Baltimore, Maryland, USA, 47, p.365.*

1445 **12 Supplementary Information**

1446 ***Supplementary Data 1:*** Summary of samples and sample depths for G4

1447 ***Supplementary Data 2:*** *Zidjerveld Palaeomag plots*

1448 ***Supplementary Data 3:*** Outcrop model (hosted on V3GEO)

1449 ***Supplementary Data 4:*** *Raw Palynology counts*

1450 ***Supplementary Data 5:*** Biomization summary

Figure 1

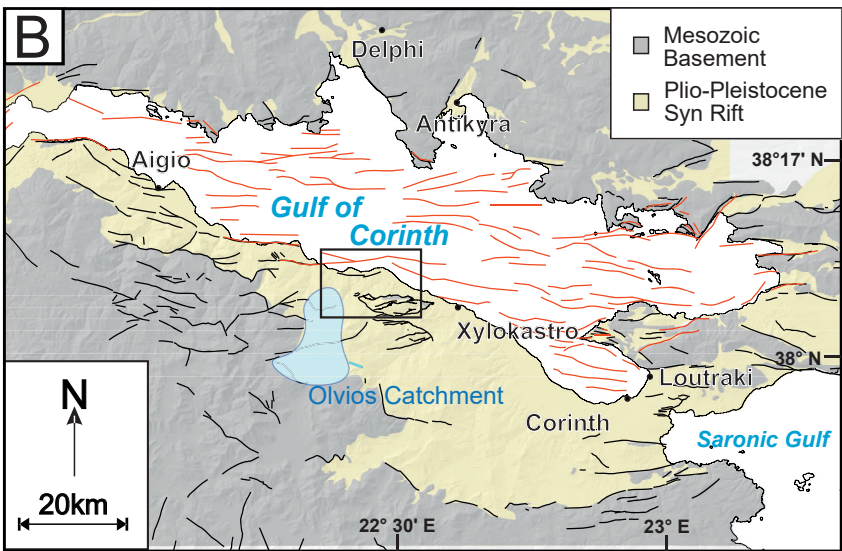
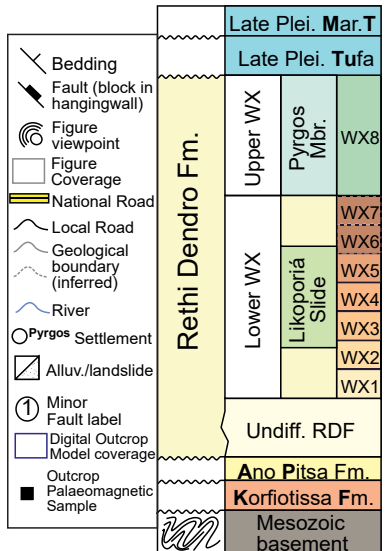
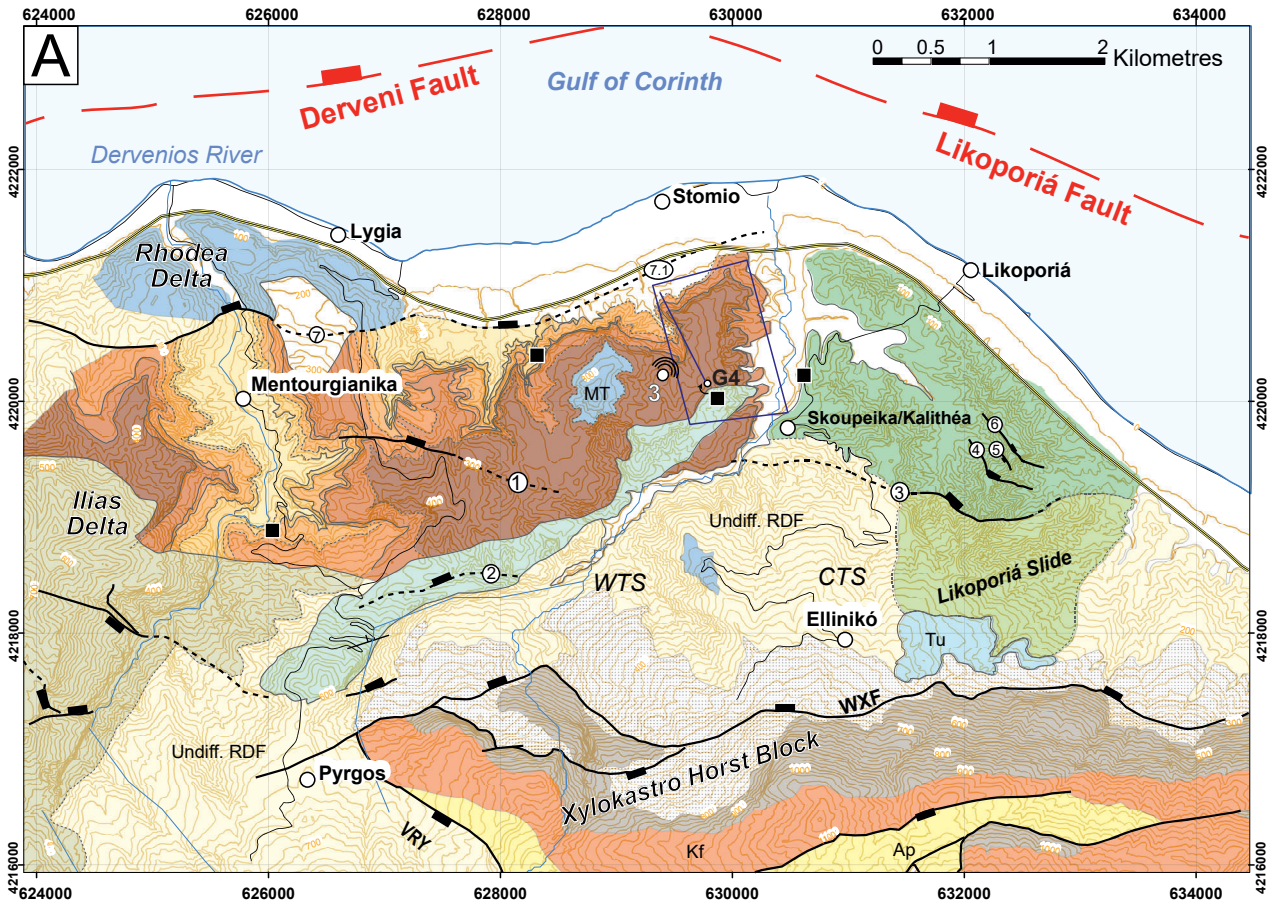




Figure 2

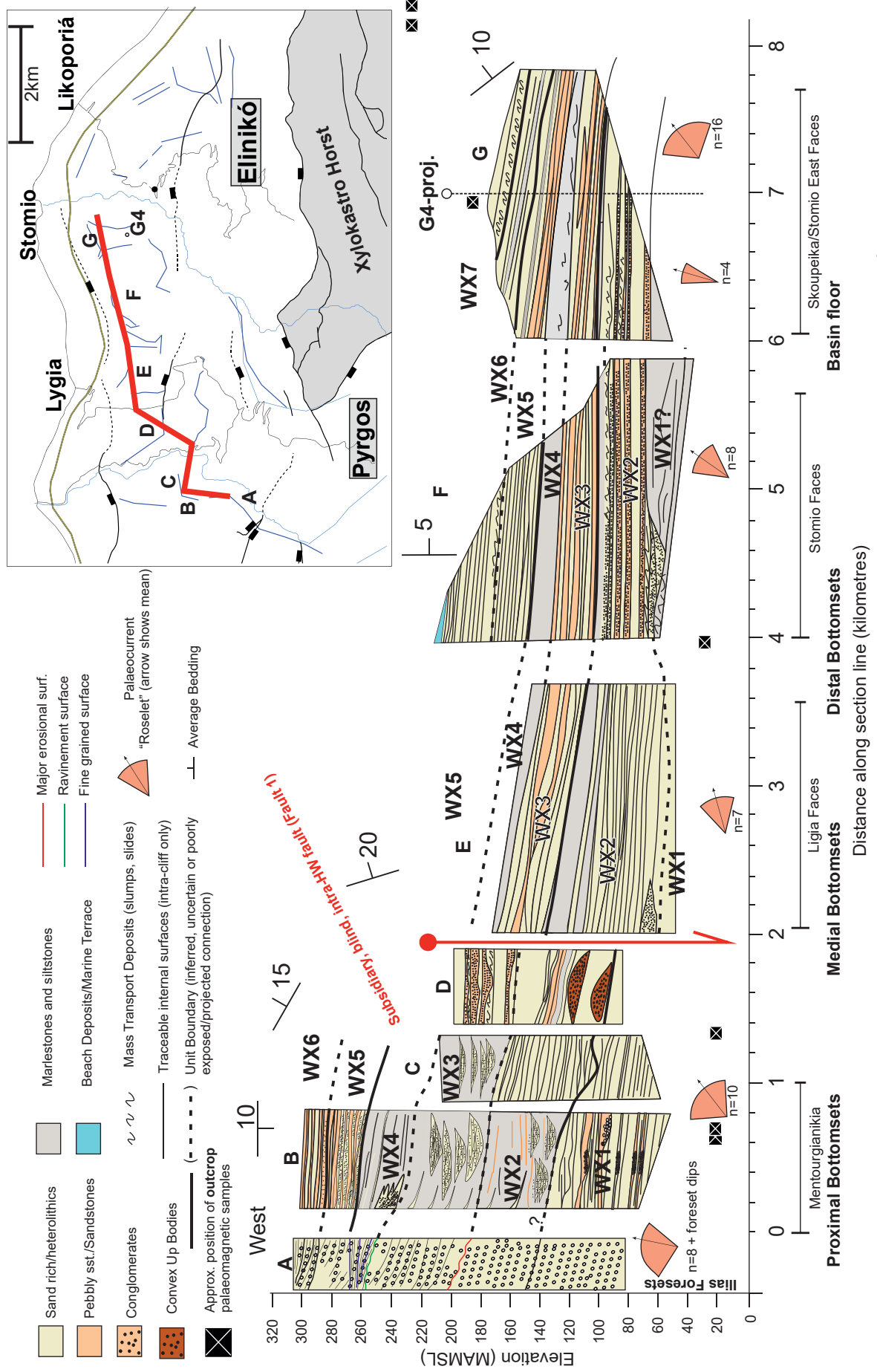


Fig3

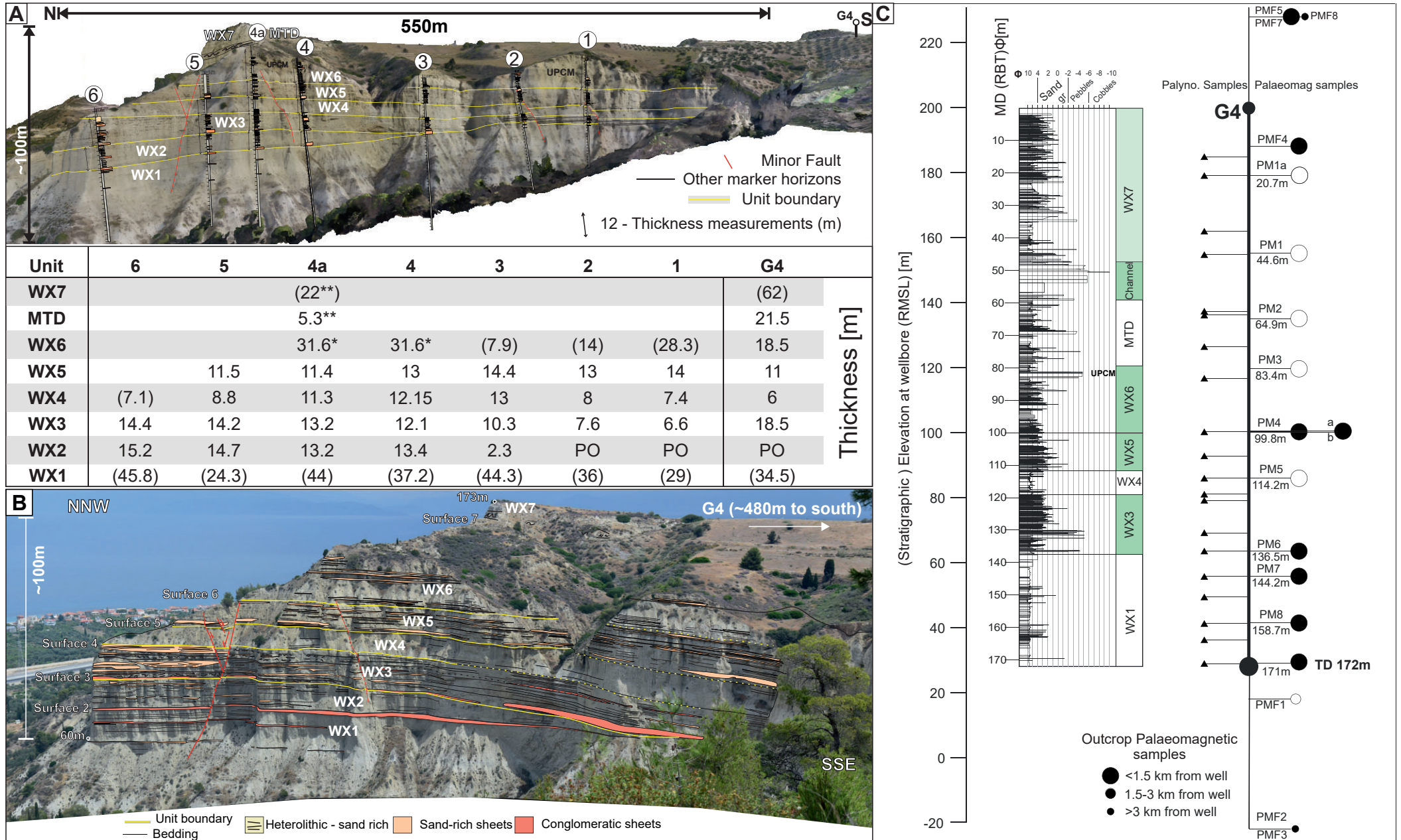




Figure 4

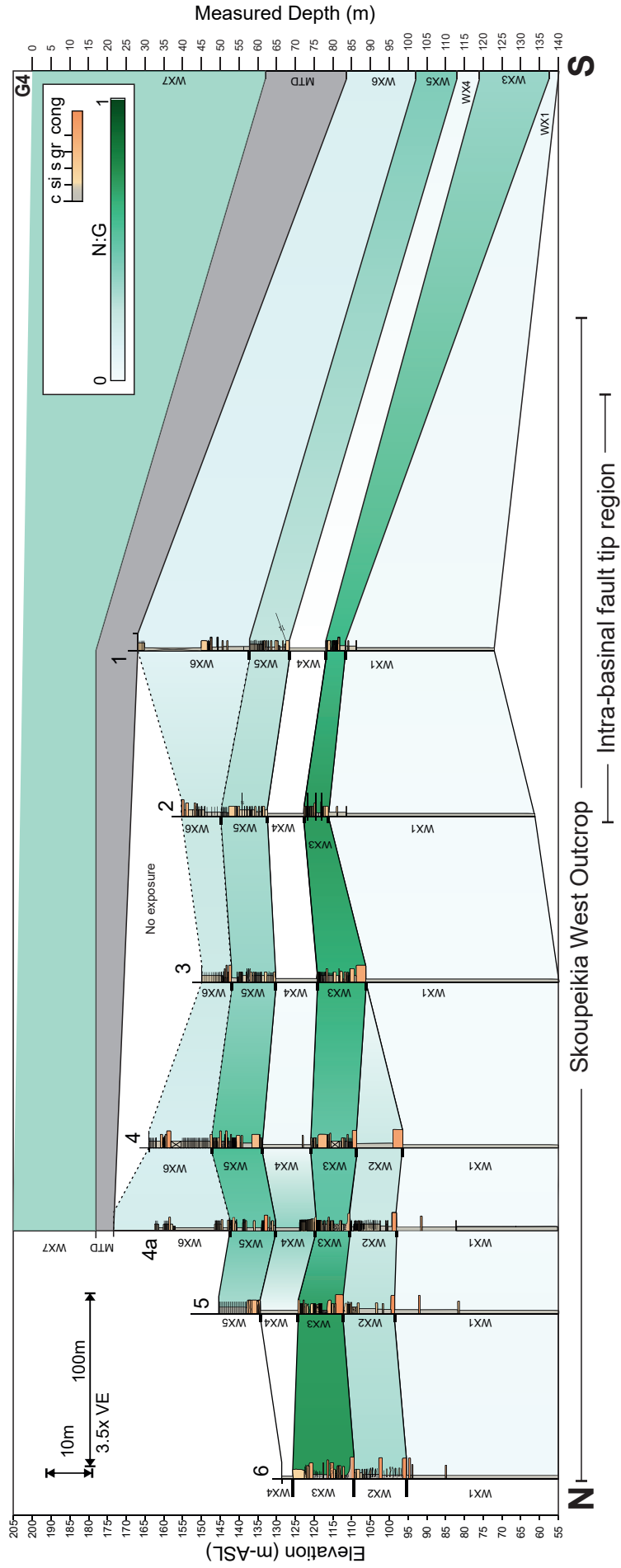


Figure 5

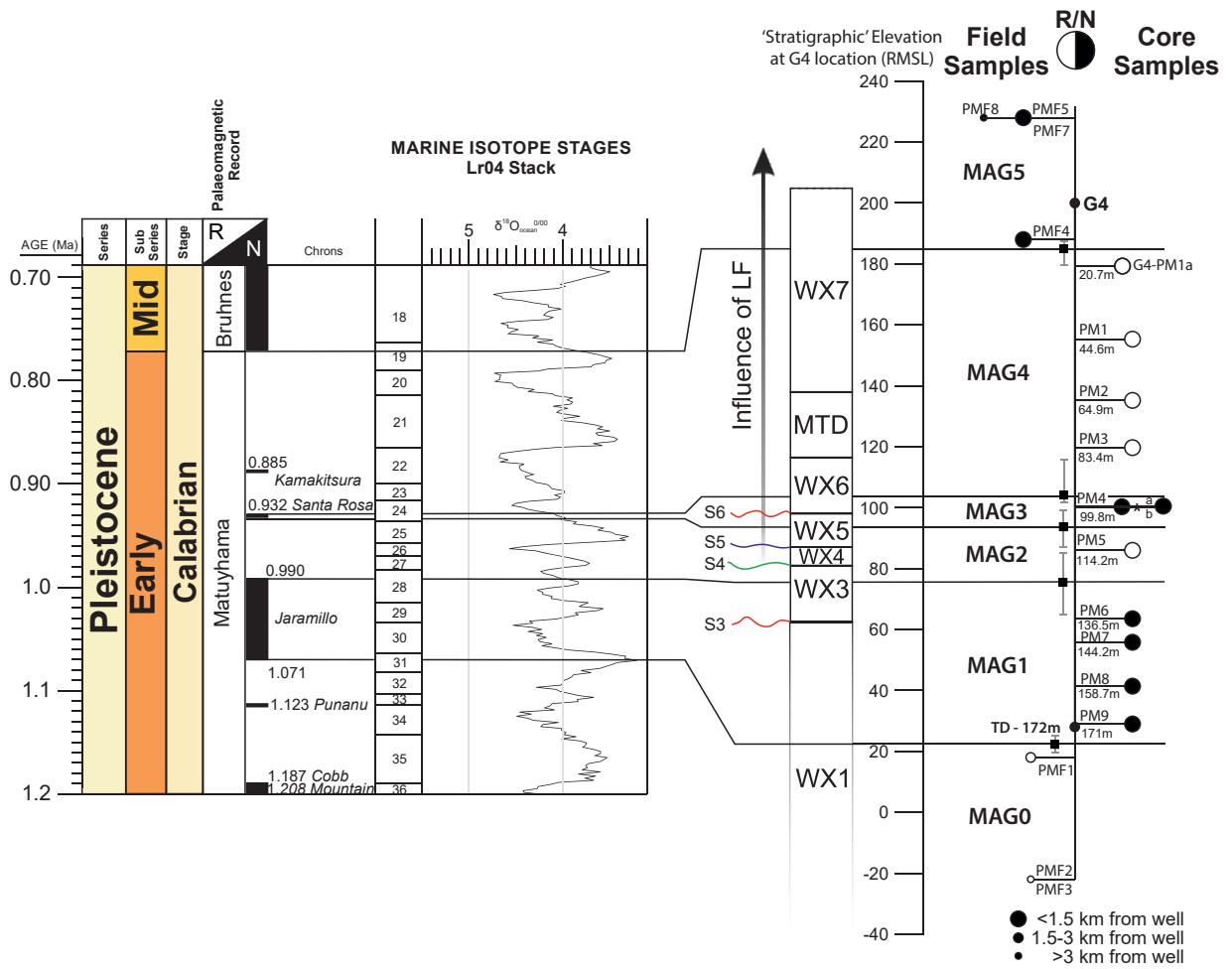
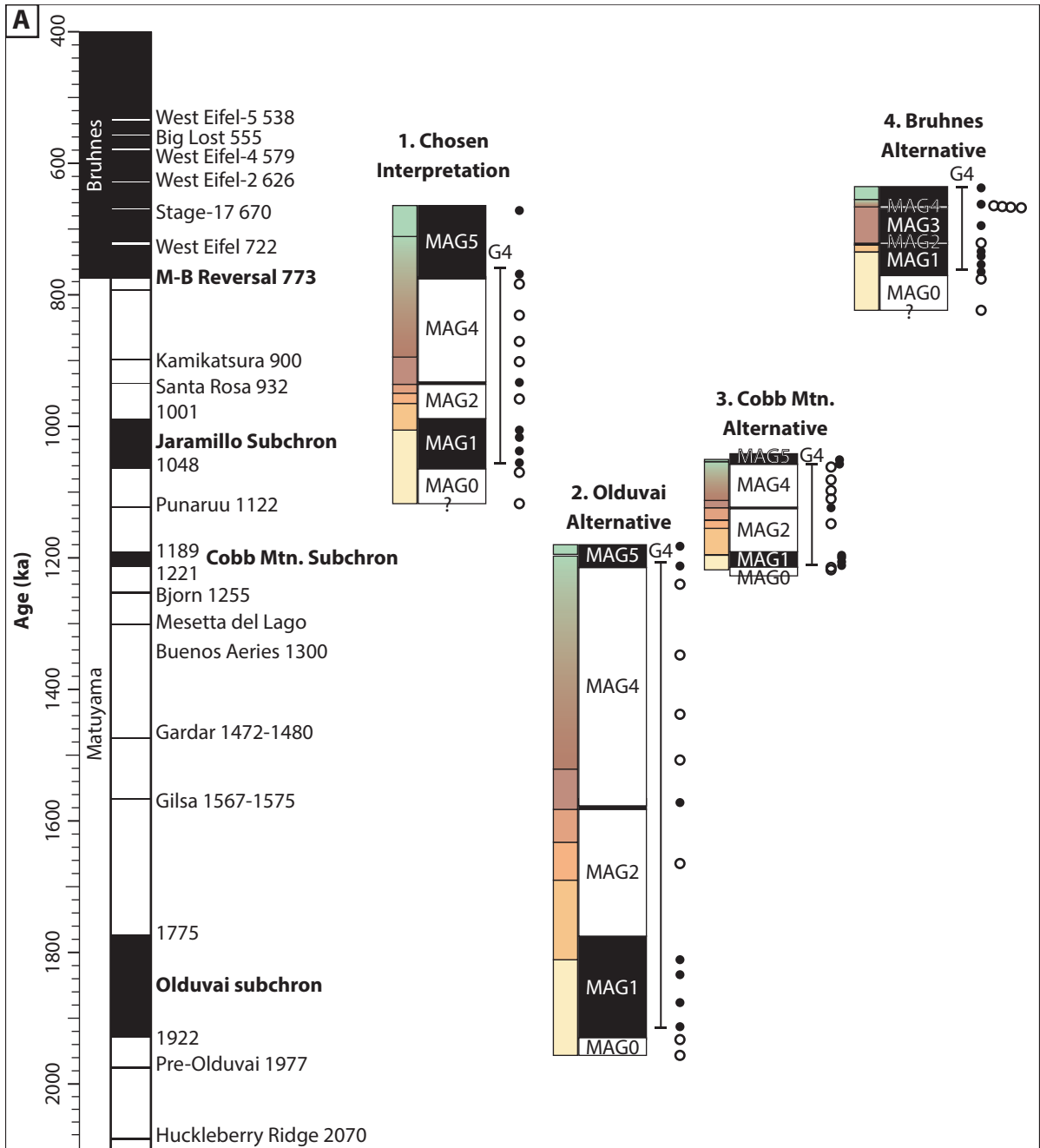


Figure 6



		Thickness (m)	Sediment Accumulation Rate at G4 (m/kyr)				
			1	2	3	4 <sup>n</sup>	
WX8+	Pyrg	MAG5	44	* 0.6	1.4	1.3	1.0
WX7		MAG4	81	0.5	0.2	0.2	<b>81.1</b>
WX6		MAG3	10	1.4 <sup>t</sup>	1.2	<b>4.9<sup>s</sup></b>	0.2
WX5		MAG2	18	0.2	<b>0.09</b>	0.3	<b>17.9</b>
WX4		MAG1	53	1.1	0.3	1.6	1.0
WX3		MAG0	44	* 0.6	0.8	1.3	1.6

	1	2	3	4
Regional palaeogeography?	✓	✗	✓	?
Required uplift/exhumation rate?	✓	✗	?	?
Sedimentation rates/variability?	✓	✗	✗	✗
Palaeomagnetic certainty?	✓	✓	✓	✗

✓ Reasonable   ✗ Unreasonable   ? Uncertain

Figure 7

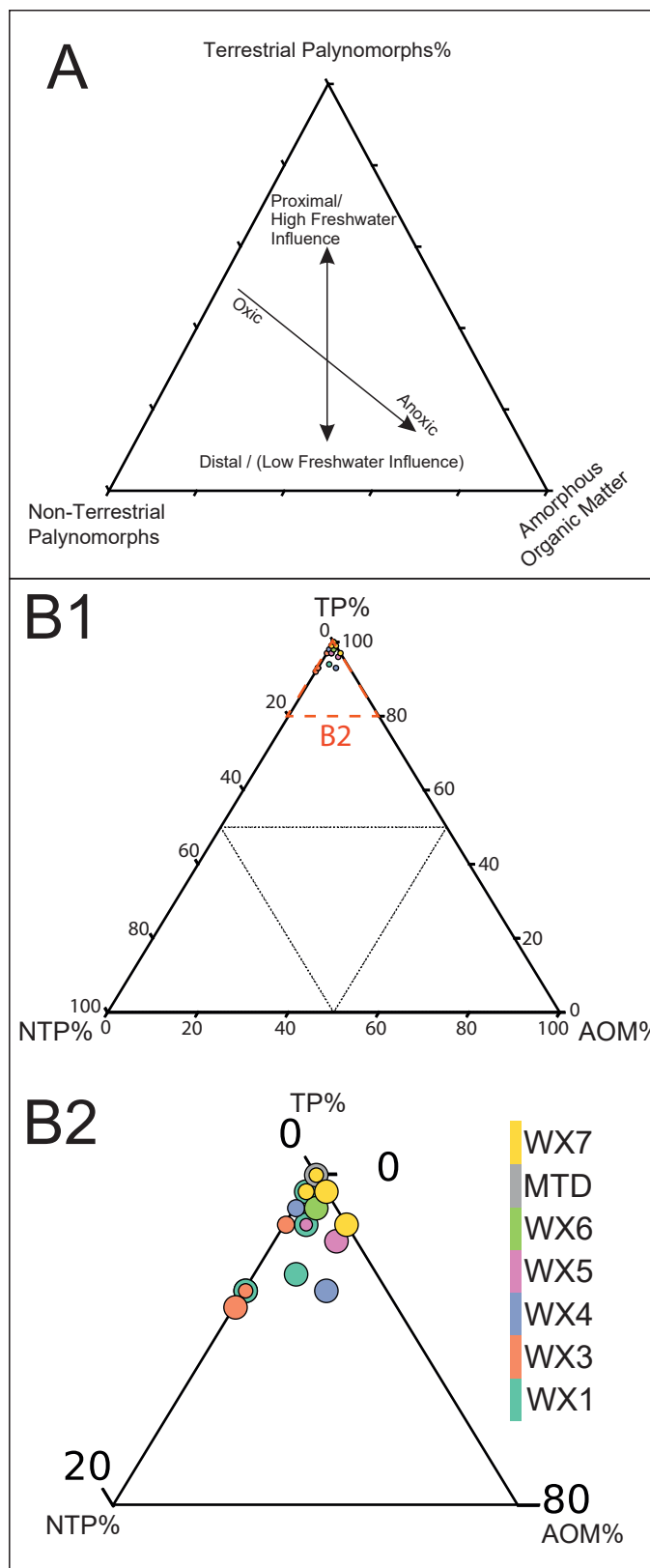
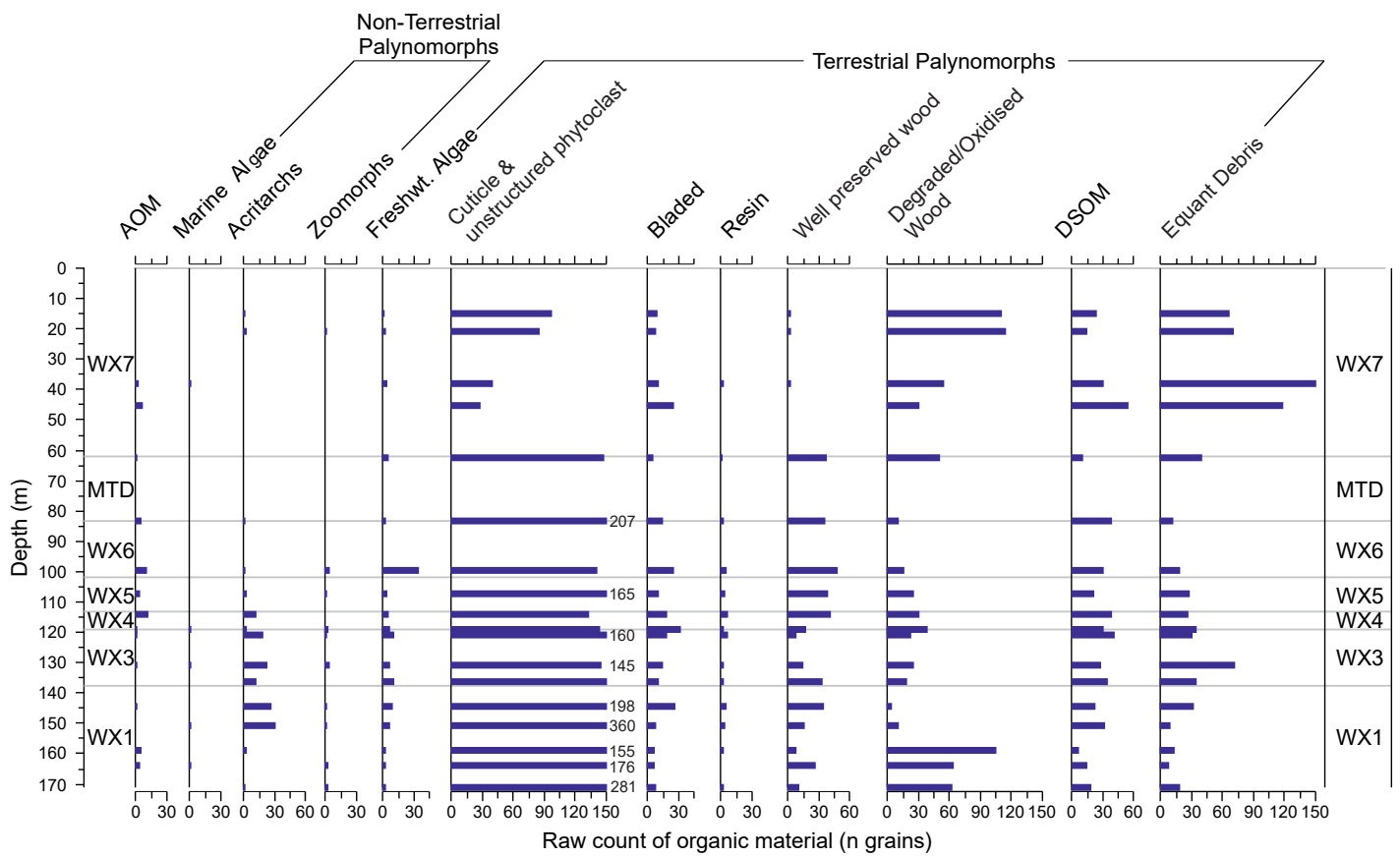


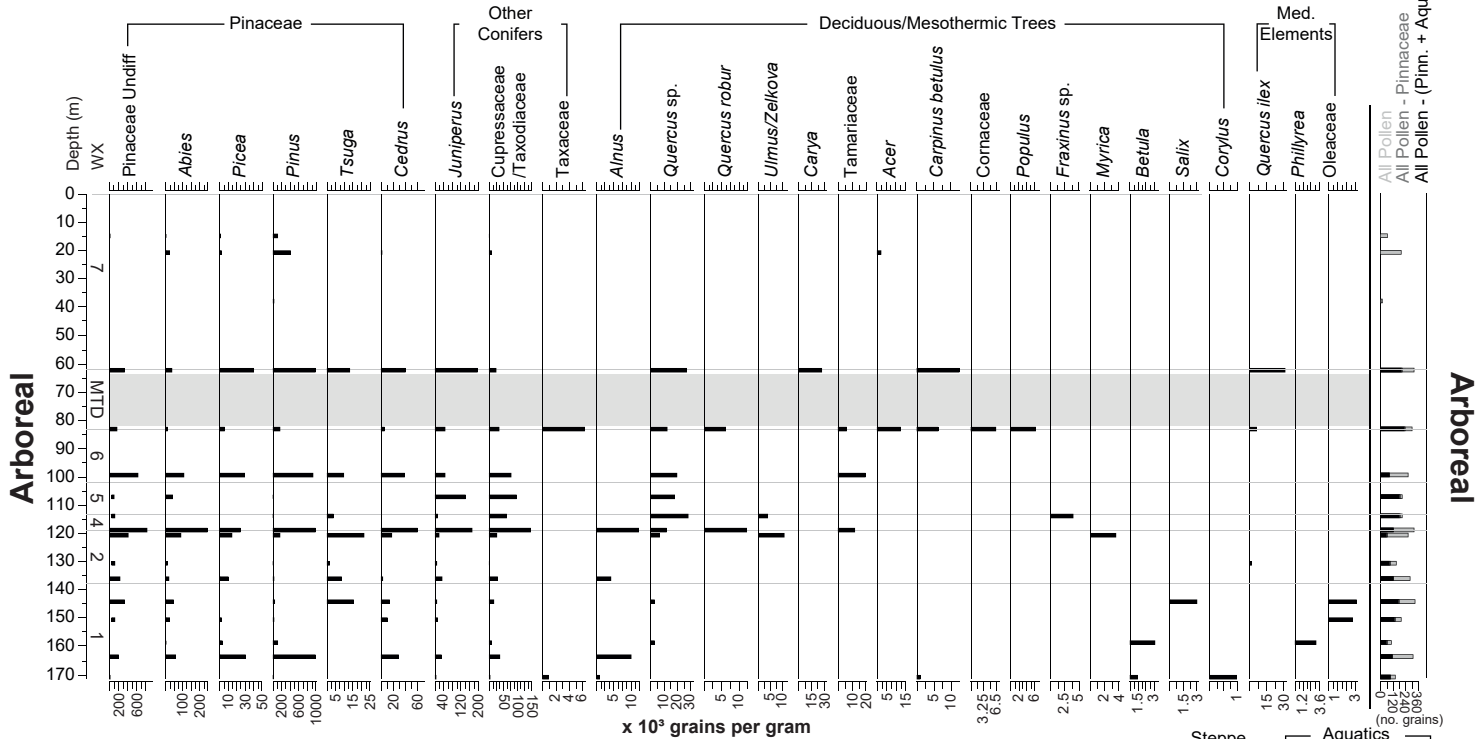
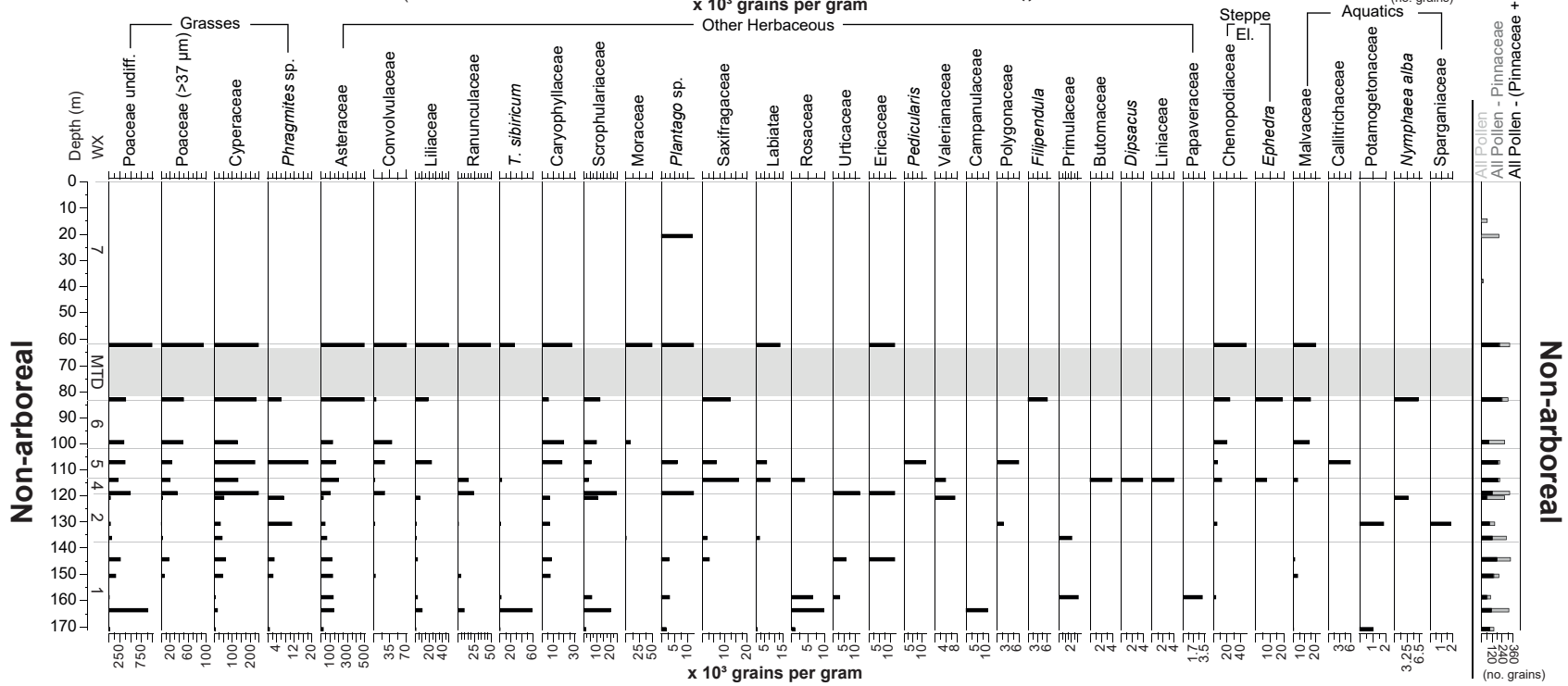
Figure 8





A

Fig10a



Non-arboreal

Arboreal

Figure 10b

**B**

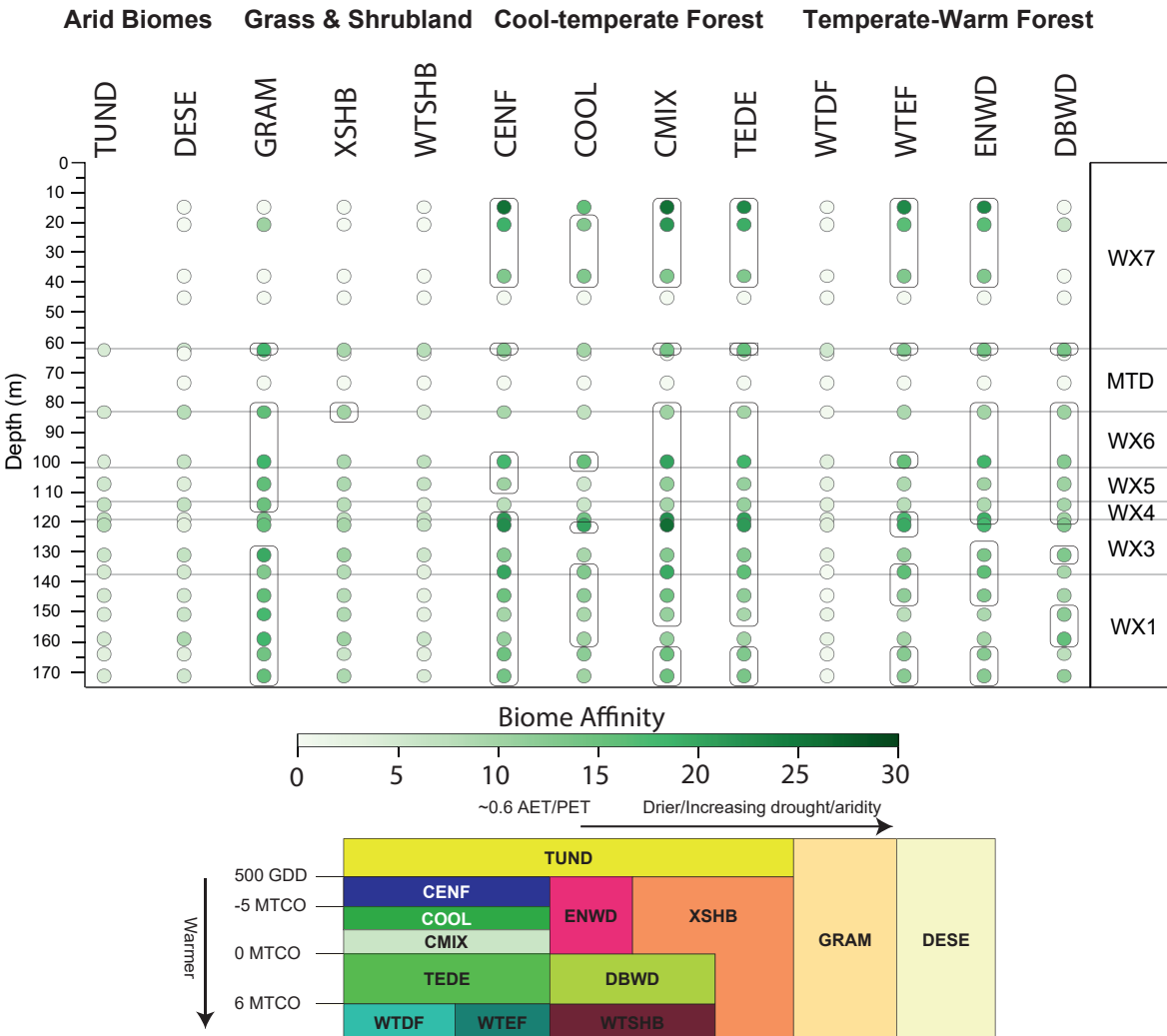
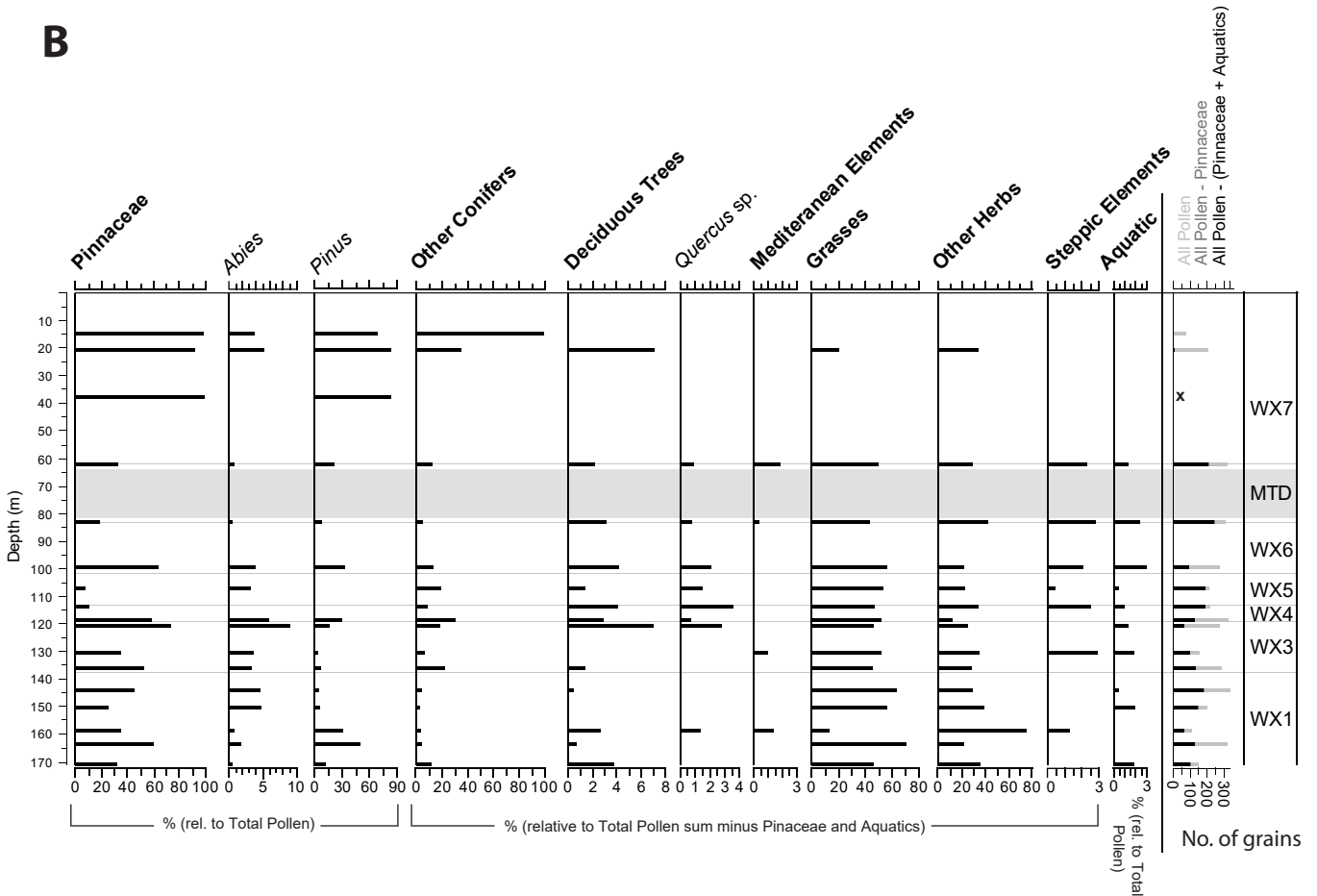




Figure 11

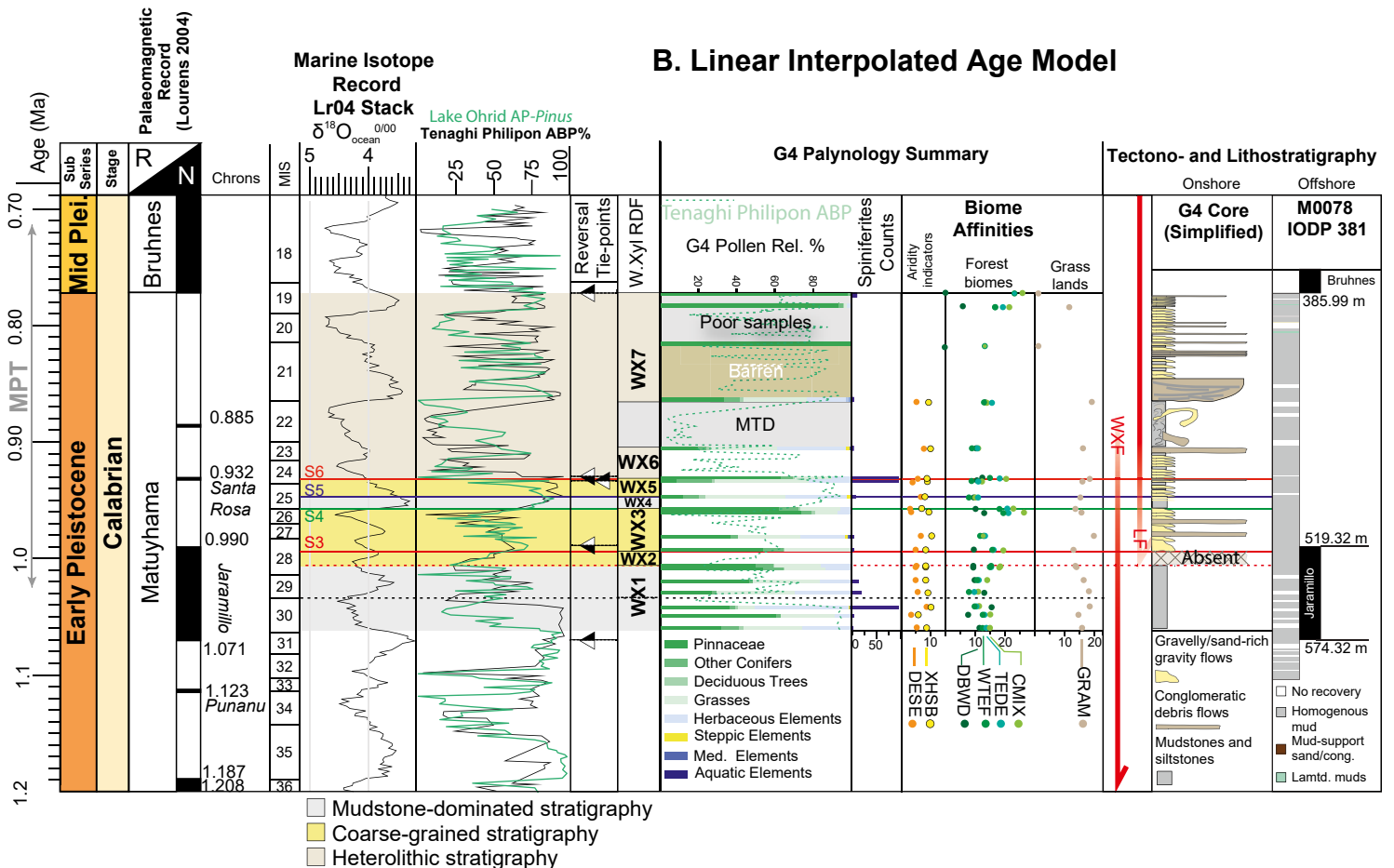
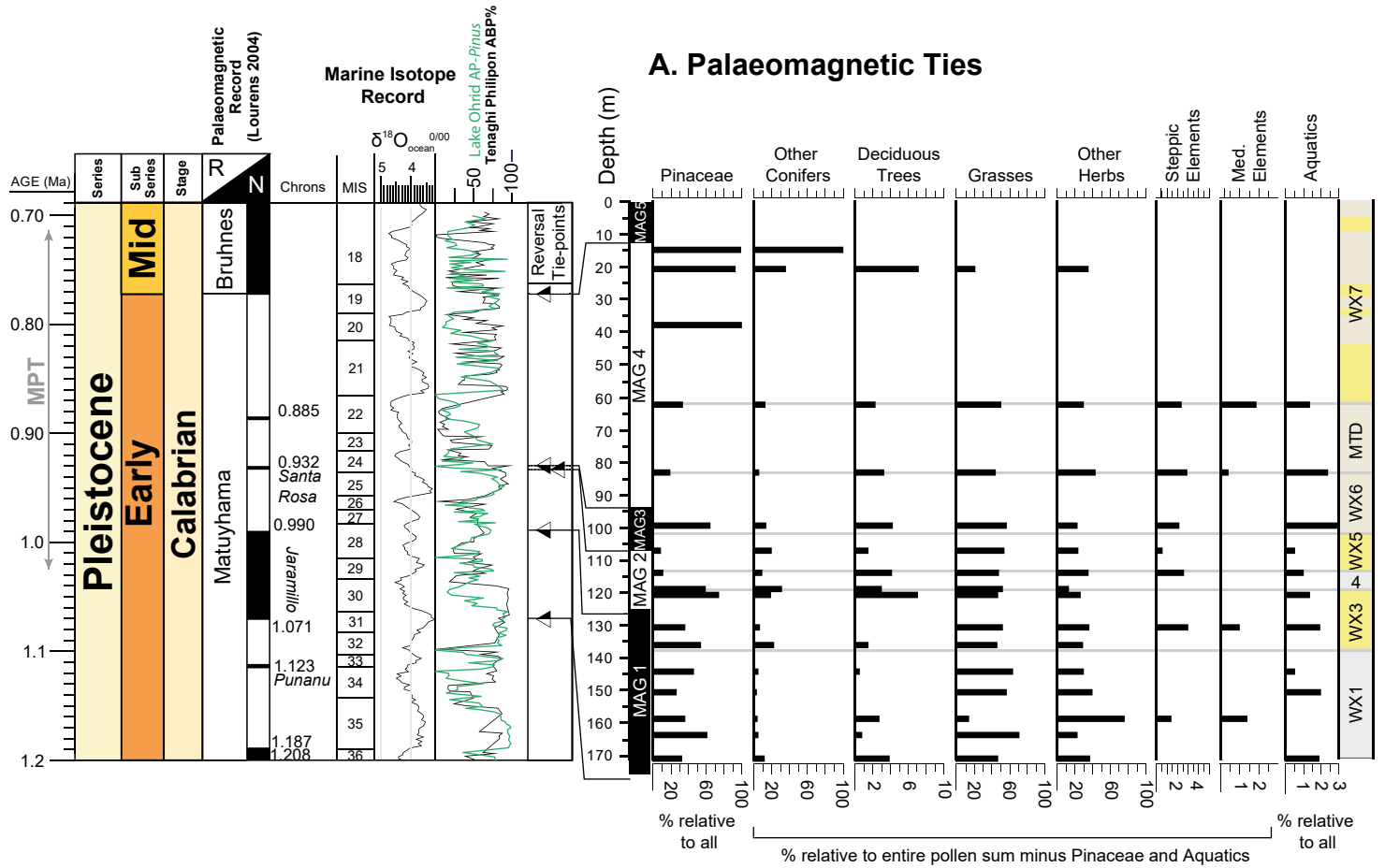


Figure 12

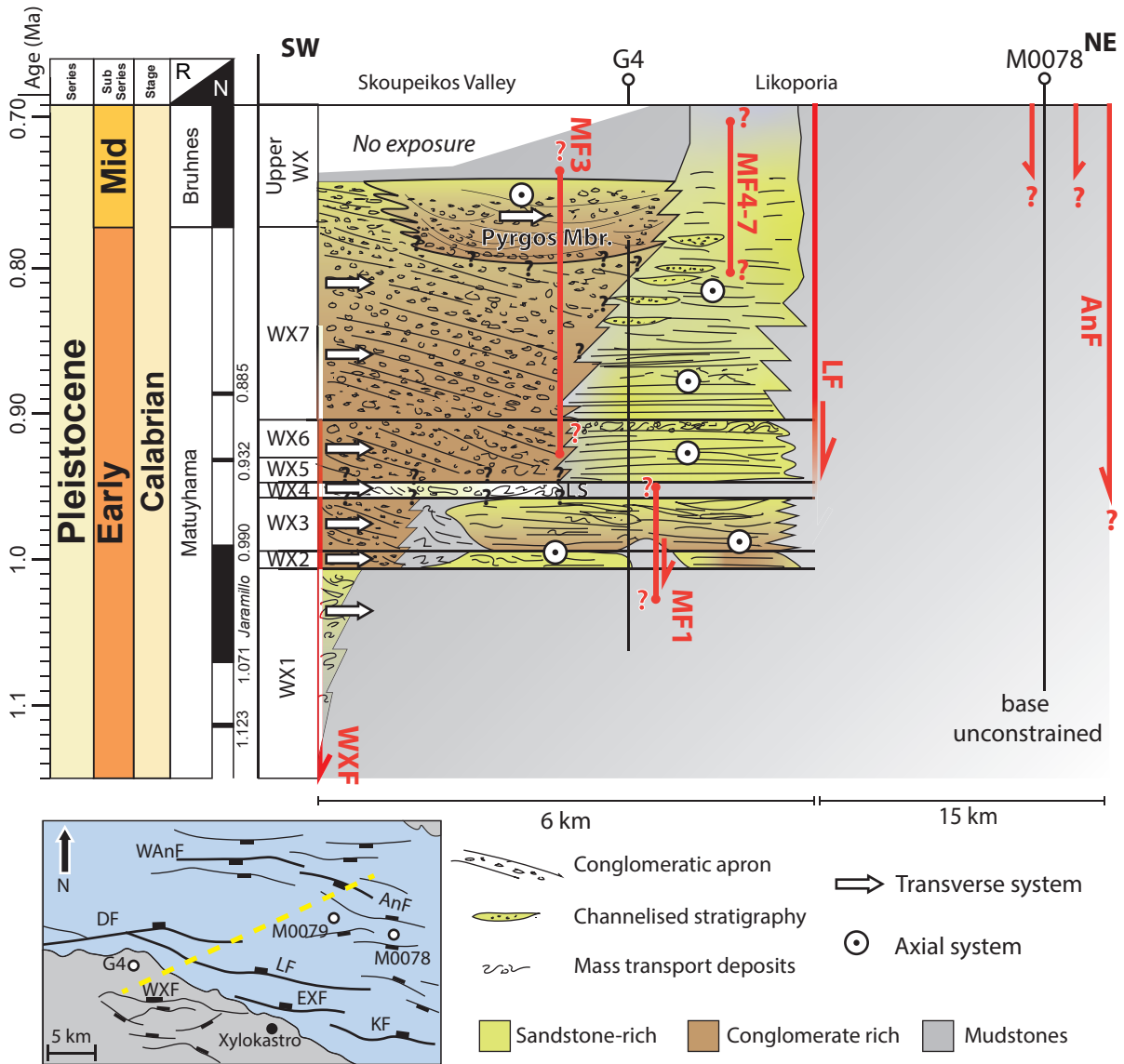
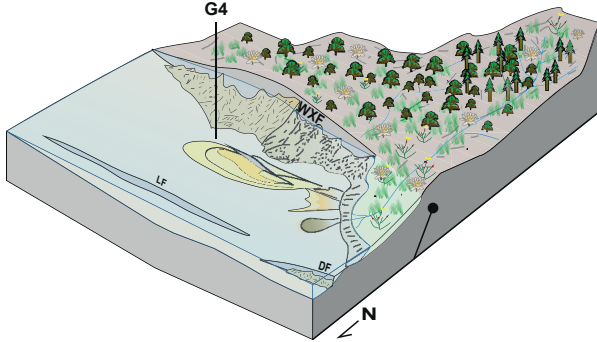


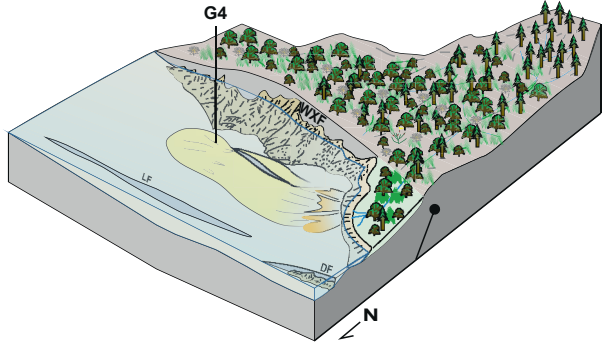
Figure 13

**A. Arboreal Pollen Reduction during cold, wet, lowstand (e.g. S2 - WX2)**



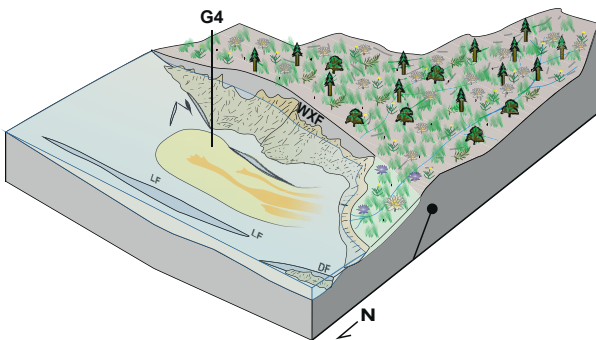
Increase in catchment sediment yield through arboreal pollen reduction permits conglomerate-grade material to be supplied into the deep-water depocentre

**B. Cool, wet glacial interstadial with onset of lake-level fall during glacial (e.g. S3 - WX3)**



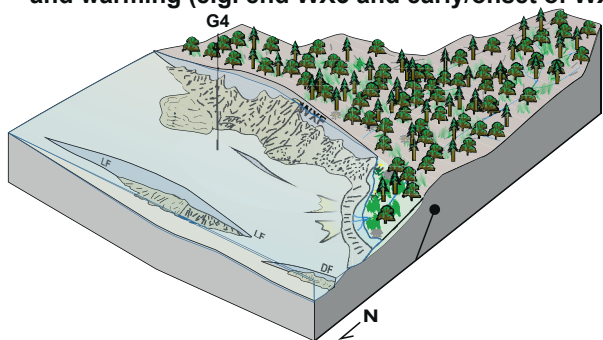
Arboreal pollen increase lowers catchment sediment yield but this is matched by wetter S. Mediterranean climate and possible minor sea-level fall permitting reworking of exposed littoral material

**C. Short lived, cool, wet, glacial (e.g. Mid-WX3)**



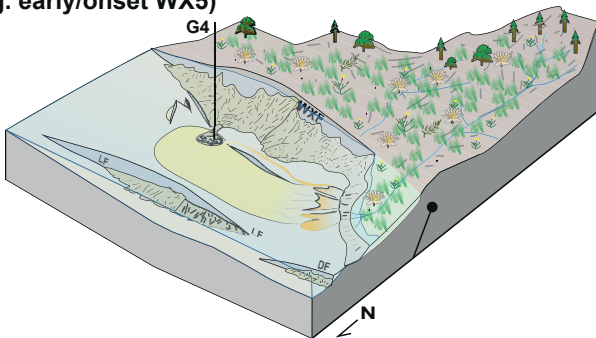
Glacial with lake-level maintained as before due to increased runoff and catchment yield permits pulses of coarser (conglomerate grade) material in broad channels to distal deepwater. Conifer populations include high-altitude cold-tolerant genera such as *Abies* and *Picea*.

**D. Quick (~10kyr), large magnitude global sea-level rise and warming (e.g. end WX3 and early/onset of WX4)**










Large magnitude global transgression/warming event. Possible minor lake level rise, accompanied by rapid reforestation reducing sediment flux to deep/water realm.

**E. Warm, semi-arid/"Mediterranean" highstand/interglacial (e.g. early/onset WX5)**



Peak of global highstand becomes too warm to support large forests in southern Greece and grassland vegetation dominates permitting high sediment yields during storm events. High run-off seen in significant freshwater algal and *Spiniferites* occurrences

-  Pines and conifers
-  Mesothermic arboreal (*Quercus*, *Acer* etc)
-  Grassland
-  Steppe elements (*Chenopodiaceae*, *Ephedra*)
-  Mediterranean elements
-  Aquatic elements (*Nymphaea* etc)
-  Herbaceous Elements (*Asteraceae* etc)


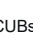



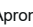
-  CUBs
-  Background/Marlstones
-  Sheet-like heterolithics (sand def.)
-  Sand rich (complex) heterolithics
-  Apron system
-  Conglomerates

Figure 14

